Characterization of Conditioned Nuclear Waste for its Safe Disposal in Europe

Deliverable D3.4
CHANCE project
Work Package 3

Work programme topic addressed: "Research and innovation on the overall management of radioactive waste other than geological disposal"

Supply Chain Security topic

Task 3.3 Exploitation of the results

EC Grant Agreement number: H2020-755371

Start date of project: June 1, 2017 Duration: 58 months

Lead beneficiary of this deliverable:

Due date of deliverable: 31/05/2021

Project funded by the European Commission within the Horizon 2020 Program (2014-2020)		
Type		
R	Document, report excluding the periodic and final reports	
DEM	Demonstrator, pilot, prototype, plan designs	X
DEC	Websites, patents filling, press & media actions, videos, etc.	
OTHER	Software, technical diagram, etc.	
Dissemination level		
PU	PUBLIC, fully open, e.g. web	X
CO	CONFIDENTIAL, restricted under conditions set out in Model Grant Agreement	

V #	Date	Type of revision	Author
0	02/05/2022	Published version	WP3

Deliverable Contributors

Authors

Partner	Name
CEA	Cédric Carasco
CEA	Bertrand Perot
SCK CEN	Bart Rogiers
SCK CEN	Eric Laloy
KEP	Christophe Mathonat
KEP IC	Andrea Francescon
KEP IC	Xavier Mettan
WUT	Wojciech Kubinski

Contributors

Partner	Name

Internal Reviewers

Partner	Name
Andra	Denise Ricard

Contents

Table of figures

Table of Tables

Glossary

Caption / Acronym	Description/Meaning
ANDRA	Agence nationale pour la gestion des déchets radioactifs
CHANCE	Characterisation of conditioned nuclear waste for its Safe Disposal in Europe
ESARDA	European Safeguards Research and Development Association
FRAM	Fixed energy, Response function Analysis with Multiple efficiencies
IEM	Infinite Energy Method
ISOCS	In Situ Object Counting System
KEPIC	KEP Innovation Centre
LVC	Large Volume Calorimeter
MCNP	Monte Carlo N-Particle code
PNMC	Passive Neutron Measurement Counting
RN	Radionuclide
SCK CEN	Belgian nuclear research centre

1 Executive Summary

1.1 Executive Factsheet

Who should read this deliverable? Who are the stakeholders concerned by this deliverable?	Why should s/he read this deliverable? What will s/he learn from this deliverable?	Which part of the content is most relevant for him / her?
End User Group	This document is presenting the results of uncertainties evaluation linked to the experimental investigation done in CEA and SCK•CEN in Task 3.2.	Section 4.5 and 5.5

FIGURE 1 - EXECUTIVE FACTSHEET

1.2 Executive Summary

The CHANCE project aims to address the specific issue of the characterization of conditioned radioactive waste. The characterization of fully or partly conditioned radioactive waste is a specific issue because unlike for raw waste, its characterization is more complex and therefore requires more advanced non-destructive techniques and methodologies.

The objective of CHANCE is to further develop, test and validate techniques already identified that will improve the characterization of conditioned radioactive waste, namely those that cannot easily be dealt with using conventional methods. Specifically, the work on conditioned radioactive waste characterization technology focuses on:

- Calorimetry as an innovative non-destructive technique to reduce uncertainties on the inventory of radionuclides.
- Muon Tomography to address the specific issue of non-destructive control of the content of large volume nuclear waste.
- Cavity Ring-Down Spectroscopy (CRDS) as an innovative technique to characterize outgassing of radioactive waste.

The present report focuses on activities from Work Package 3 related to the development of the calorimetry. In the frame of the Task 3.3. the exploitation of the results of the measurements carried out with mock-up waste drums at CEA Cadarache and SCK CEN with gamma spectrometry, passive neutron counting and using the calorimeter developed by KEP Technologies, was done. SCK CEN also performed measurements with a 200 L real unconditioned waste drum. This document presents the analysis of the results obtained with the different techniques and the combination of the different technics to better characterize the mock up and real drums and reduce the associated measurement uncertainties. Also, some MCNP modelling of the calorimeter and gamma spectrometry were performed in the framework of the performed experiments.

2 General introduction

Deliverable 3.3 [1] of CHANCE WP3 was aiming at describing the measurement campaigns performed at CEA and SCK CEN, highlighting the raw measurement results, and providing a first interpretation in terms of activities for most measurements. In this document we focus more on the uncertainties related to the different measurement techniques.

On the one hand, a large simulation study is performed to assess the theoretical uncertainties related to the calorimeter measurement, through investigating the deposition of energy within the measurement chamber. This study is presented in Section 3.

On the other hand, an update on the measurement interpretation is provided, obtained by probabilistic modelling of the individual measurements, as well as combinations of measurement techniques, to assess the added value of calorimetry and the more conventional NDA techniques used in the investigated cases. These studies are presented in Sections 4 and 5, for the experiments and modelling performed at CEA and SCK CEN respectively.

Furthermore, as we had the opportunity to do additional joule effect calibration measurements at SCK CEN, after completion of the planned measurement campaign, and can exploit the measurements with reference sources as well for that calibration, a more thorough investigation (compared to what was presented in [1]) on the calibration of the calorimeter sensitivity coefficients, and their uncertainty was performed as well. This is presented in Section 5.2.

3 Calorimeter modelling

3.1 Numerical model of the calorimeter

Matching the design of the calorimeter, a simplified but still viable numerical model was implemented using the MCNP6 code. The numerical model is presented in Figure 2. It consists of different layers, just alike the real KEP-LVC calorimeter. There is a cylindrically shaped sample drum (60 cm in diameter and 88 cm high) at the centre of the measurement chamber which is filled with air. The next layer is the octagon-shaped structure with the heat flux detectors mounted on each wall. Then, there is the package of alternating homogenization (red layers in Figure 2) and insulation layers (blue layers in Figure 2), up to six layers each. Underneath the measurement chamber, we can find the reference chamber (or ghost chamber) with a phantom aluminium block.

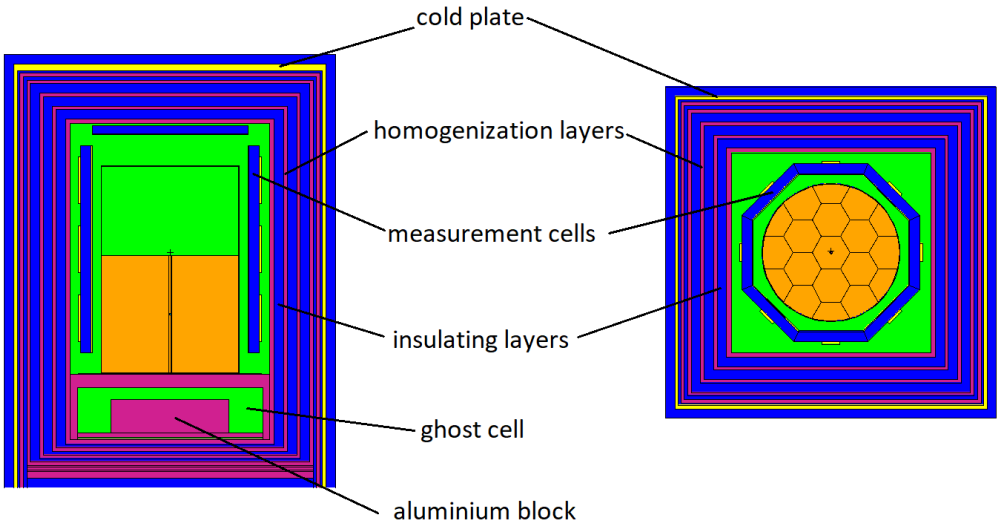

FIGURE 2. THE MCNP MODEL.

3.2 Nuclear vectors definition

Two approaches were used in the simulation. For the first approach, we simulated the emission of gamma particles and neutrons with energies in the range 10^{-2}-10^{6} eV to check energy deposition in the drum and the penetration properties of these particles depending on their energy. The second approach consisted of simulating typical nuclear vectors that can be expected in waste drums and checking the possibility of characterizing these materials using a combination of calorimetry and gamma spectrometry. To implement the second approach, four typical nuclear vectors were provided by ANDRA, as shown in Table 1.

TABLE 1. ANDRA'S NUCLEAR VECTORS.

Isotope	vector no 1	vector no 2	vector no 3	vector no 4
Pu238f	11,1%	15,2%	-	11,1%
Pu239f	2,1%	17,8%	0,02%	3,1%
Pu240f	2,3%	17,1%	0,01%	4,3%
Am241f	43,1%	49,7%	3,3%	30,0%
Sr90f/Y90f	6,6%	-	44,9%	18,7%
Cs137f/Ba137m	8,5%	-	51,3%	30,3%
Cm244f	24,0%	-	-	1,9%
Tc99f	1,0%	-	-	-
Others	1,4%	0,2%	0,4%	0,6%
Total	100,0%	100,0%	100,0%	100,0%

3.3 Combination of calorimetry and gamma spectrometry

As part of the project, several simulations were performed to determine the possibility of combining calorimetric measurements with other non-destructive methods. This chapter describes simulations for the potential combination of calorimetry with gamma spectrometry.

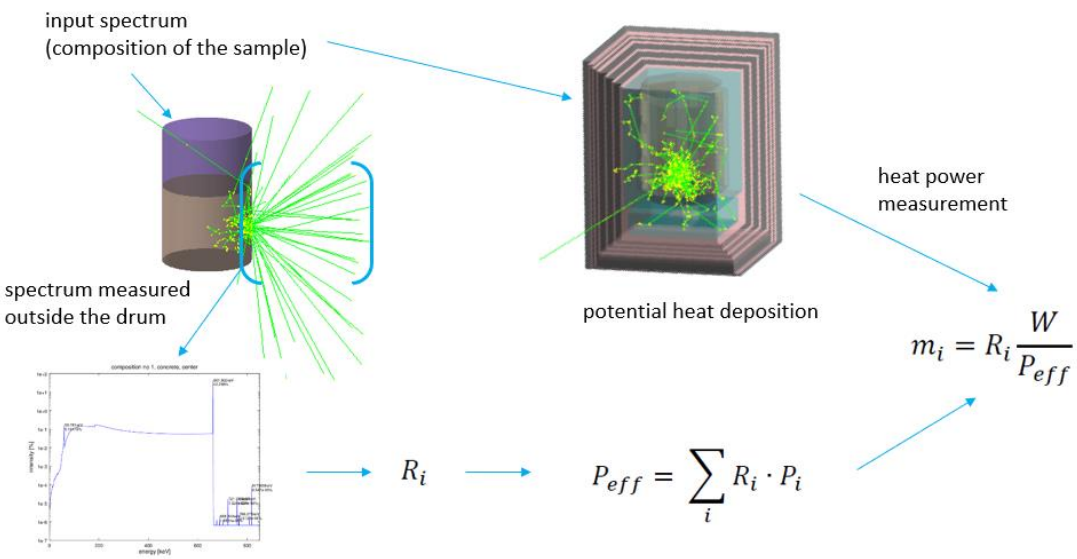

FIGURE 3. COMBINATION OF GAMMA SPECTROMETRY AND CALORIMETRY - METHODOLOGY.

In this series of analyses, simulations of the calorimetric measurement and simulations of the spectrometric measurement were carried out to combine the results obtained using both methods. Using the Monte Carlo Geant4 code, a simulation of >10^8 particles emitted from different parts of the drum was performed. On the one hand, it was checked which spectrum of particles that leave the drum can be measured outside (gamma spectrometry), and

on the other hand, which is the energy deposition and heat power inside the drum (calorimetric measurement), as shown in Figure 3.

3.3.1 Gamma spectrometry

After simulating the spectrum outside the drum, the share of a given isotope *k* based on a selected peak *p* can be determined in the simplest method by comparing the relative intensities:

$$R_k = \frac{I_{k,p}}{\alpha_{k,p}} \cdot \left(\sum \frac{I_{i,p}}{\alpha_{i,p}}\right)^{-1}, \qquad \alpha_{k,p} = A_k BR_k^p \tag{3.1}$$

$$m_k = I_{k,p}/\alpha_{k,p} \tag{3.2}$$

Where:

t – simulated time *[s]*
R_k– relative share of k-compound
$I_{k,p}$ – intensity given peak of k-compound
A_k – specific activity of k-compound *[Bq/g]*
$BR_{k,p}$ – branching ratio of k-compound and analysed peak *p [%]*
m_k – mass of isotope *k* calculated using selected peak intensity *[g]*

3.3.2 Calorimetry

Knowing the potential percentage composition of the mixture determined using gamma spectrometry, it is possible to determine the effective heat power (P_{eff}) of the material inside the drum [2]:

$$P_{eff} = \sum_i R_i \cdot P_i \tag{3.3}$$

Where:

R_i- relative share of *i*-compound [%]
P_i- effective power of *i*-compound [W/g]

After simulating the power that will be deposited in the matrix (W), one can determine what is the total mass of radioactive material inside the drum:

$$m = \frac{W}{P_{eff}} \tag{3.4}$$

Then the mass of the *i-th* element will be determined as:

$$m_i = R_i \cdot m = R_i \cdot \frac{W}{P_{eff}} \tag{3.5}$$

3.3.3 Example composition

Simulations were made, among others, for one of the typical compositions that can be found in nuclear waste drum (Andra's vectors). For this mixture, it was checked what spectrum can be measured outside the drum and what heat power is emitted in the matrix.

TABLE 2. EXAMPLE COMPOSITION: ANDRA'S VECTOR NO 2.

isotope	abundance
Pu238	15.2%
Pu240	17.1%
Pu239	17.8%
Am241	49.7%
Total	100.0%

As part of the simulation, 1g of the material was placed at the edge of the drum, halfway up the active part $\left(\frac{H}{2}; R\right)$. From this position, $4 \cdot 10^8$ gamma particles were emitted with a spectrum corresponding to the mixture in Table 2. The spectrum obtained outside the drum is shown in Figure 4.

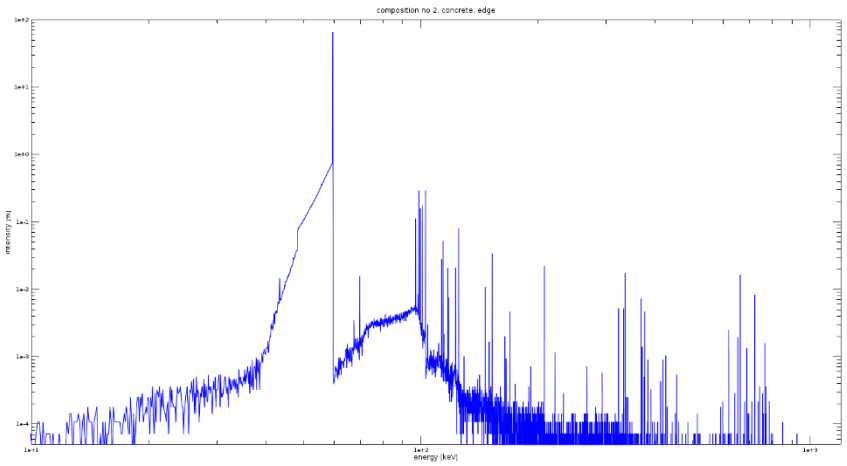

FIGURE 4. GAMMA SPECTRUM OUTSIDE THE DRUM.

Then the peaks in the spectrum were recorded. The criteria for registration were that the peak was 1.5 times the mean value in the 0.5keV window. Table 3 shows the list of the registered peaks.

TABLE 3. REGISTERED PEAKS.

isotope	E [keV]	intensity [%]
Am241	59.52	6.48E+01
Am241	67.43	2.43E-03
Am241	101.04	1.73E-01
Am241	106.40	6.43E-04
Am241	113.29	2.74E-02
Am241	114.21	5.18E-02
Am241	114.91	1.79E-03
Am241	117.46	2.04E-02
Am241	122.99	2.05E-02
Am241	150.03	1.64E-03
Am241	165.80	8.58E-04
Am241	169.54	4.54E-03
Am241	267.53	6.79E-04
Am241	332.35	5.15E-03
Am241	376.63	4.61E-03
Am241	383.79	8.93E-04
Am241	619.00	2.47E-03
Am241	688.70	1.32E-03
Pu239	129.27	8.58E-04
Pu239	413.70	3.93E-04
Pu238	43.43	7.58E-03
Pu238	99.84	1.57E-01
Pu238	766.37	1.57E-03

Only those peaks with the best statistics and similar energies were selected for further analysis. Gamma particles with significantly different energies would be absorbed by the matrix and wall of the drum in different ways, disturbing the comparison of peak intensities and thus determination of the percentage share of a given isotope. In Table 4 the selection of peaks is presented. At this stage, the simplest method of characterization was used, so single peak analysis. Three peaks (one for each isotope) were used for further analysis. The peaks were chosen to be as close to each other as possible (to minimize the effect of different attenuation at different energies) but at the same time with relatively high number of counts to provide sufficient statistics.

TABLE 4. PEAKS CHOSEN FOR ANALYSIS AND CALCULATIONS RESULT.

isotope	E [keV]	N	u(N)	intensity [%]	BR [%]	activity [Bq/g]	equivalent mass [g]:	Ri	u(Ri)	real
Am241	114.21	1.45E+03	3.81E+01	5.18E-02	2.80E-05	1.27E+11	5.28E-02	61.0%	2.5%	49.7%
Pu239	129.27	2.40E+01	4.90E+00	8.58E-04	6.31E-05	2.30E+09	2.15E-02	24.8%	5.1%	17.8%
Pu238	99.84	4.41E+03	6.64E+01	1.57E-01	7.35E-05	6.34E+11	1.23E-02	14.2%	5.9%	15.2%

The analysed peak intensities correspond respectively to the following masses: 0.05g, 0.02g and 0.01g of Am241, Pu239 and Pu238, so around 0.08g in total. Based on these masses, the composition of the mixture can be determined as Am241: 61.0% (vs. expected 49.7%), Pu239: 24.8% (vs. 17.8%) and Pu238: 14.2% (vs. 15.2%). Three of the four isotopes have been identified. Only the Pu240 isotope was not recognized due to the overlapping of its spectrum with other isotopes of Pu. Knowing the percentage shares of isotopes, the effective power of the sample was determined (Table 4) using equation ((3.3).

TABLE 5. EFFECTIVE POWER CALCULATION [3].

isotope	Pi [mW/g]	Peff·Ri [mW/g]	u(Peff) [mW/g]
Am241	1.15E+02	7.02E+01	1.76E+00
Pu239	1.93E+00	4.79E-01	2.45E-02
Pu238	5.68E+02	8.04E+01	4.72E+00
	Total:	1.51E+02	5.04E+00

Then, a simulation of energy deposition in the matrix and wall of the drum was performed. The simulations showed that the thermal power of the drum would be $W = 142\ mW$. Then, using the previously determined effective power and equation ((3.4), one obtains 0.94 g of radioactive material (out of 1 g of simulated material).

TABLE 6. RESULTS OF COMBINATION OF GAMMA SPECTROMETRY AND CALORIMETRY.

isotope	measured	M_i with calorimetry [g]	$u(M_i)$ [g]	real [g]
Am241	61.0%	0.57	0.02	0.497
Pu239	24.8%	0.23	0.01	0.178
Pu238	14.2%	0.13	0.01	0.152
Pu240	-	-	-	0.171
total	100%	0.94		1.00

Table 6 shows a summary of the results obtained. The simulations showed that for the composition under consideration, by combining calorimetry with gamma spectrometry, one could potentially characterize 0.94 g per 1 g of the mixture, however, overestimating the mass of Am241 by about 0.07g, overestimating the mass of Pu239 by 0.05g, underestimating the mass of Pu238 by 0.02g and not characterizing Pu240. Although the case under consideration assumed a very simplified method of comparing the peaks, it shows the methodology and possible improvement of the results when combining calorimetry with gamma spectrometry.

3.3.4 Background radiation influence

This section describes simulations performed in order to investigate the potential influence of background radiation on the analysis of the peaks and the characterization of the compositions considered. For this purpose, a background radiation spectrum was defined in addition to the spectrum derived from radioactive material. The gamma spectrometric measurement was simulated again. The simulated time of measurement was 96 seconds. The spectrum of the background radiation was taken from the literature [4]. An example of the spectrum of the mixture for which the background radiation introduced relatively the greatest differences (up to 14%), is presented below.

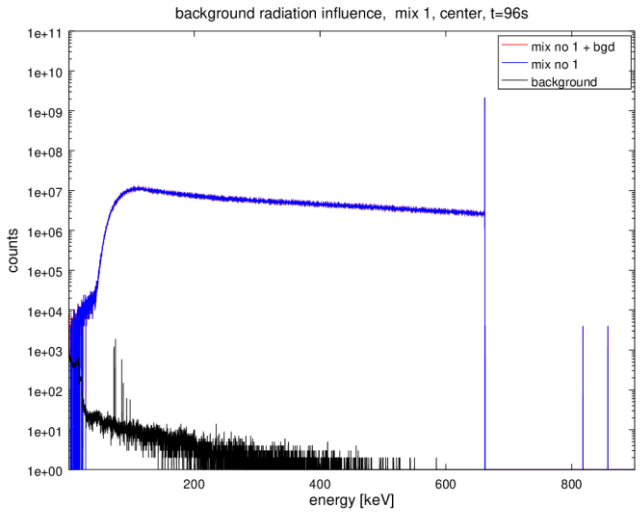

FIGURE 5. SPECTRUM FOR MIX NO 1 PLACED IN THE CENTRE OF THE DRUM COMPARED WITH THE BACKGROUND RADIATION.

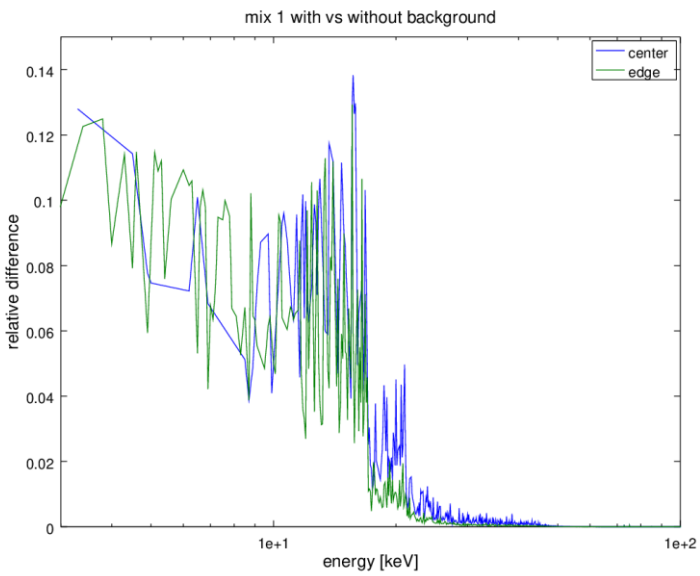

FIGURE 6. DIFFERENCE BETWEEN SPECTRUM FOR MIX NO 1 AND SPECTRUM WITH BACKGROUND RADIATION. FOR THE SOURCE PLACED IN THE CENTRE AND BY THE EDGE OF THE DRUM.

Figure 6 shows that the greatest differences appear for energies <20keV and raise up to 14%. However, such particles with low level energies have few chances to leave the drum. Typical spectral analysis usually includes peaks with energies greater than 50keV for which these differences are much smaller (much less than 1%), as most of the background spectrum that was used is below 50 keV. It can therefore be seen that for the considered compositions, the background radiation will have little effect on the spectrometric analysis, in case of the considered vectors.

3.3.5 Attenuation of the gamma radiation inside the drum

Large-volume and heterogeneous drums are problematic to characterize. Because of the large volume, the radioactive materials can be distributed in an heterogenous manner in the matrix. Radioactive materials can be close to the edge of the drum or buried/hidden inside other materials or shielded [5]. Depending on the type of matrix, its composition, the position of the source inside the drum, and the energy of emitted particles, attenuation of the radiation can vary, as well as the corresponding contribution to the spectrum. In order to evaluate the impact of the distribution of the radioactive materials, simulation of the emission of gamma particles with energies from 100keV to 1MeV was undertaken. A spectrum of 10 mono-energetic peaks was considered: 100, 200, ..., 1000 keV, all of equal intensity. Particles were emitted from the centre or the edge of the drum. Two matrices were considered: bitumen and concrete, with or without elements (bubbles, steel, aluminium) inside the matrix. The Figure 7 shows the scenarios considered.

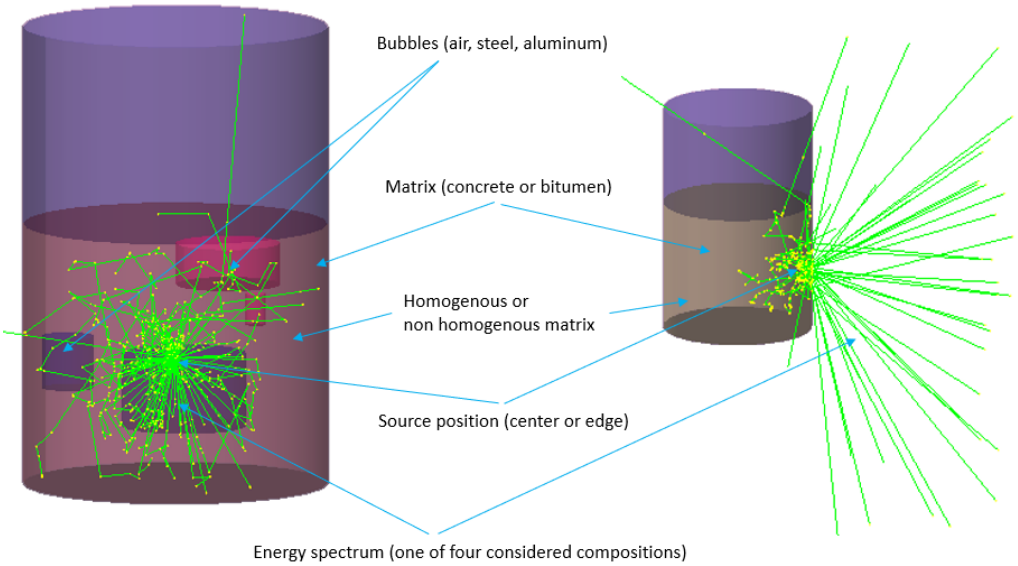

FIGURE 7. CONSIDERED SCENARIOS.

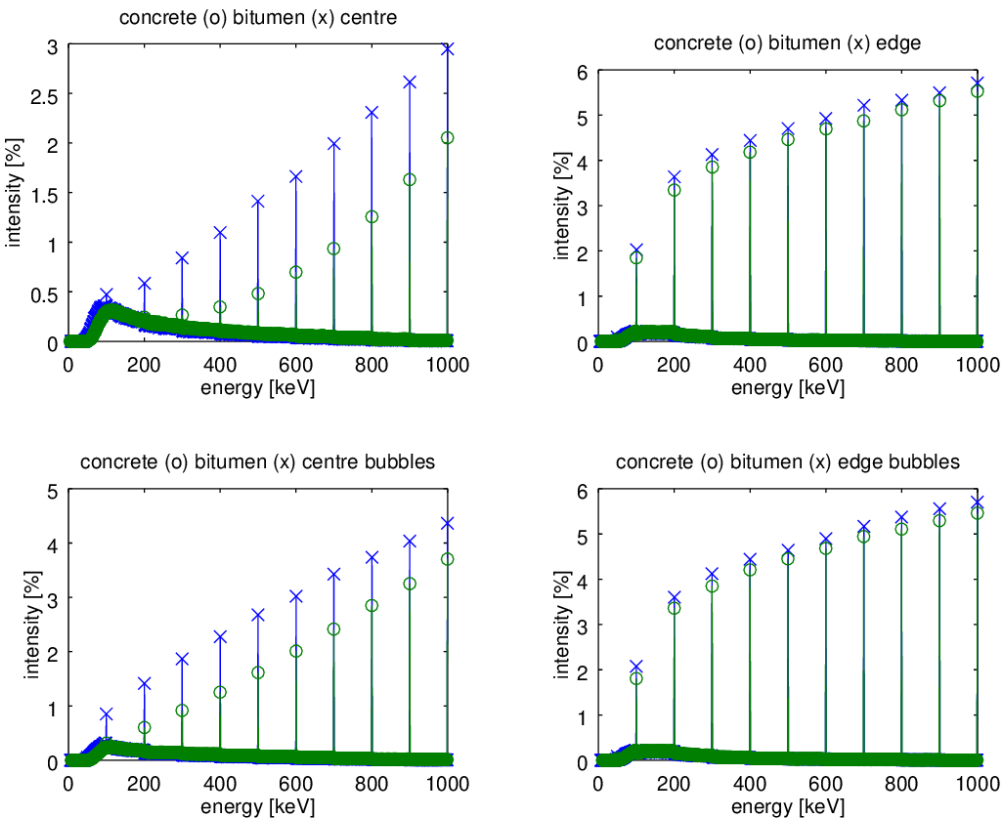

FIGURE 8. ATTENUATION ANALYSIS RESULTS FOR CONCRETE (BLUE LINE) AND BITUMEN (GREEN LINE) MATRIX.

The results (Figure 8) shows that, depending on the scenario, self-attenuation may have different effects on the spectrum measured outside the drum and in general this influence may be non-trivial and difficult to define a priori. The simulations showed that, depending on the scenario and energy, the peak intensity can be weakened by about 2 to 20 times and increase approximately linearly with the energy or satisfy the relation: $\exp(-\alpha/E)$.

The available software of gamma spectrometers uses methods that partially take into account the effects of self-shielding, they adjust the spectrum analysis by assuming simple geometry and attenuation of the material and use multiple peak analysis. However, they require prior information on the approximate matrix composition and distribution and/or require knowledge on the homogeneity and composition of the materials [6]

3.3.6 Infinite energy method (IEM) for radioactive materials characterization

One of the methods of considering the self-attenuation effect is the infinite energy method (IEM), in which for a selected isotope the determined mass is plotted against the 1/E, where E is the energy of the radiation peak on the basis of which the mass is determined. The final mass is determined by extrapolating the function fitted to the measured points and determining its value at the zero point. As Am-241 appears in all the considered vectors (four ANDRA's vectors), and it is characterized by several peaks (Table 7) of high intensity and a wide range of energy, this isotope could be used to determine a function that could, to some extent, reflect the attenuation properties of the drum (assuming that all remaining radioactive material is similarly distributed to Am-241) [7].

TABLE 7. AM241 PEAKS FOR INFINITE ENERGY METHOD.

E_k [keV]	$1/E_k$ [keV^{-1}]	m_k^{Am241} [g]
69.8	0.0143	0.029(3)
101.1	0.0099	0.081(2)
103.0	0.0097	0.083(2)
117.5	0.0085	0.106(8)
123.0	0.0081	0.110(9)
208.0	0.0048	0.163(12)
335.4	0.0030	0.230(20)
662.4	0.0015	0.255(21)

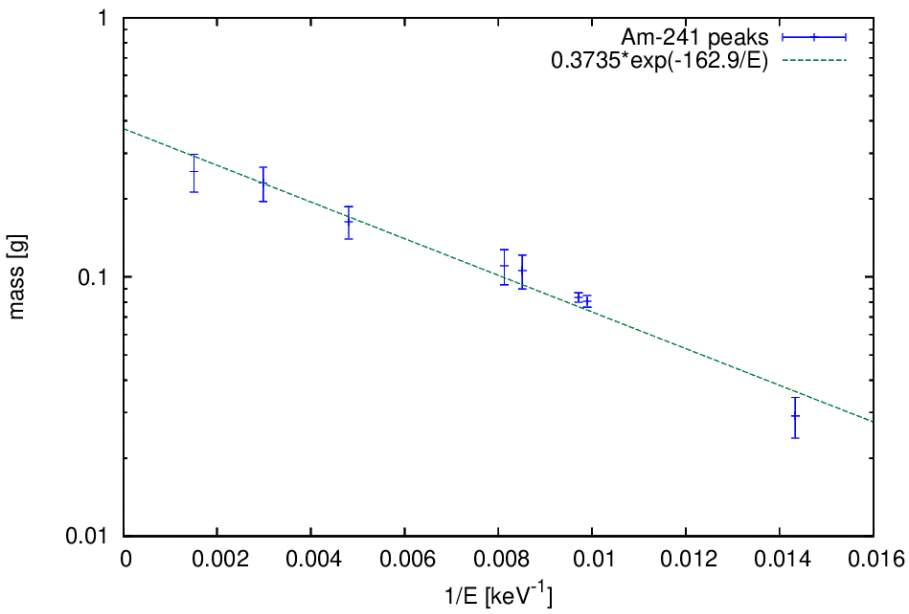

FIGURE 9. INFINITE ENERGY METHOD FOR AM-241.

Figure 9 shows the use of Infinite Energy Method IEM for 0.497g of Am-241 located at the edge of the drum. Single peak analysis leads to a maximum of 0.26g of Am-241 (51% of the simulated content). Whereas the mass of Am-241 determined using IEM is equal to 0.37g (74%). IEM was used to more accurately determine the mass of the Am-241. It can also be used to define the following equation:

$$F(E) = m_{IEM} \cdot e^{-\alpha E} / m_{IEM} = e^{-\alpha E} \tag{3.6}$$

Where m_{IEM} and α are curve fitting factors and m_{IEM} corresponds to the mass calculated using IEM.

To some extent *F(E)* would reflect the gamma attenuation properties of the matrix and wall of the drum. Thus, any mass m_k^i of isotope *i* determined using peak *k* of energy E_k would be adjusted using the function ((3.6):

$$\tilde{m}_k^i = \frac{m_k^i}{F(E_k)} = m_k^i \cdot^{\alpha E_k} \tag{3.7}$$

Figure 10 presents the *F(E)* as a function of the gamma particle energy.

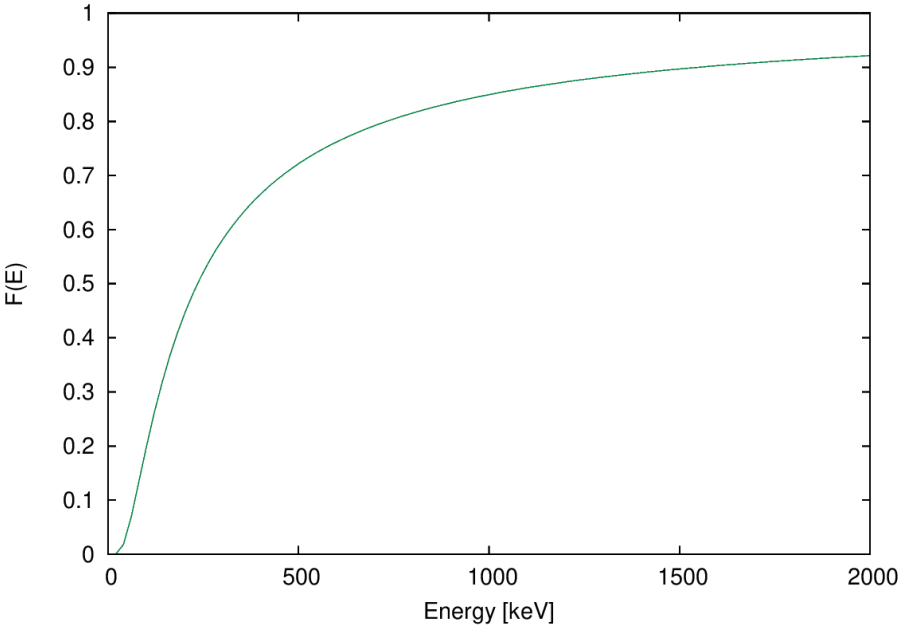

FIGURE 10. ATTENUATION CURVE APPROXIMATED USING AM-241 PEAKS.

TABLE 8. IEM MASS ADJUSTMENT, ANDRA'S VECTOR NO 2.

isotope	E [keV]	equivalent mass [g]:	equivalent mass_adj [g]	Ri	Ri_adj	u(Ri)	mass with calorimetry [g]	u(mass) [g]	simulated mass [g]
Am241	114.2	0.05	0.22	61.0%	61.4%	2.5%	0.58	0.01	0.50
Pu239	129.3	0.02	0.08	24.8%	21.1%	5.1%	0.20	0.01	0.18
Pu238	99.8	0.01	0.06	14.2%	17.5%	5.9%	0.16	0.01	0.15

Table 8 shows the adjustment of mass using IEM. Masses calculated using simple peak analysis for Am241, Pu239 and Pu238 were equal to 0.05g, 0.02g and 0.01g whereas masses adjusted using IEM were equal to 0.22g, 0.08g and 0.06g, being closer to the expected values (0.50g, 0.18g and 0.15g). On the basis of this values percentage shares were determined and equal to 61.4%, 21.1% and 17.5% and after multiplying it by 0.94g of total radioactive material (from calorimetry) the final detection was: 0.58g for Am-241, 0.20g for Pu239 and 0.16g for Pu238.

3.4 Gamma and neutron radiation leakage

In the context of the use of gamma spectroscopy in the characterization of radioactive materials, it is important that a major part of the gamma radiation can escape from the inside of the drum to be captured by the detectors. For calorimetry, which measures the heat emitted by the material, it is important most of the radiation energy is deposited in the drum and the measurement chamber (measurement Peltier elements). It can however happen that some of the particles (neutrons and high-energy gamma particles) escape from the drum and deposit some of their energy outside the drum. This part of the energy is not measured or can even lead to a double error when deposited in the reference parts of the calorimeter (reference Peltier elements) [8]. When a particle deposits energy in the

reference part, this part is not detected by the measurement Peltier elements and it also decreases the final signal (as it is measured by the reference Peltier elements).

3.4.1 Considered scenarios

To check how the distribution of radioactive material inside the drum influences the radiation leakage, three simulation scenarios were studied. For all the scenarios the drum was filled with a radioactive material to a height of 50 cm (it is defined as the active part of the drum). The remaining part of the drum was filled with air.

Scenario I.

The first source configuration, hereafter called the “most conservative” set-up was a drum filled with sand and one pin of radioactive material placed in the centre of the drum. In the middle of the pin a container with the sampled source was placed. It was assumed that all the radioactivity was hidden deeply inside the drum, thus on average, the path for the particle to escape was the highest. This configuration is called the most conservative scenario.

Scenario II.

In this scenario, hereafter called the “homogenous” set-up, it was assumed that the radioactive material is uniformly distributed within the whole volume of the active part of the drum. The active part was filled only with sand and particles were sampled inside this whole volume. The amount of escaping radiation was, of course, higher in this case, as the particles can be nearby the edge of the drum as well.

Scenario III.

A third kind of source configuration, hereafter called “least conservative” set-up was a drum, similar to case I, but with only one pin placed near the edge of the drum. In addition, the container with the virtual radioactive material was located at the bottom of the pin. In this scenario the particles, on average, had the shortest path to leave the system.

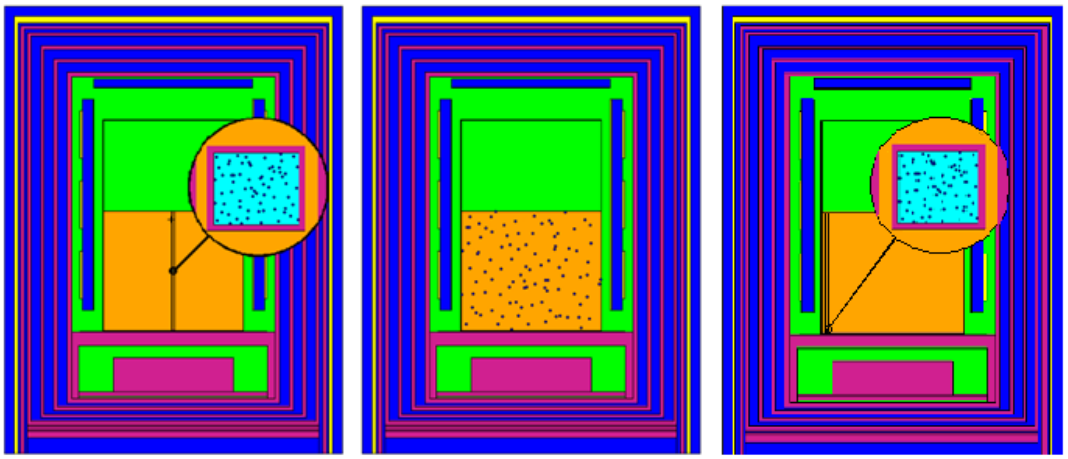

FIGURE 11. VISUALIZING THE COMPARING SCENARIOS: MOST CONSERVATIVE SOURCE (LEFT), HOMOGENOUS (MIDDLE) AND LEAST CONSERVATIVE (RIGHT).

Figure 11 shows the differences between sampling particles scenarios in all three kinds of the source configurations. The radioactive composition was modelled by a virtual gamma source and a virtual neutron source at energies from 10 keV up to 10 MeV. In addition, some calculations of waste composition for beta and alpha emission were carried out too, but as expected, no escaping radiation was found.

3.4.2 Energy - power conversion

In the MCNP input file it is only possible to define energy of a single source particle and the total number of emitted particles (which usually depends on calculation time and the complexity of the problem). It simulates what happened with every single particle and not make possible to define the associated energy.

I order to calculate the energy deposition and the associated power (in *mW*), and the specific power, the mean energy per one source particle, must be multiplied by the activity α of the source:

$$P = \bar{E} \cdot a \tag{3.8}$$

where $\bar{E}$ is the calculated energy (MeV/particle) and a is the activity (Bq/g).

The equation ((3.8) is true only for the mono-energetic source. For more complicated spectrum, we must use the relation:

$$\bar{E} = \sum_{i=1}^{k} \bar{E}_i n_i \tag{3.9}$$

where n_i- number of the particles emitted by the i-th isotope, k -number of isotopes.

In a real case, the simulated material would be described by the isotopic composition. As each isotope would have a different activity and branching ratio (BR) of a given particle, the number of the particles emitted in time *t,* would be equal to:

$$n_i = a_i \cdot BR_i \cdot t \tag{3.10}$$

Using the equation (3.10) in the equation (3.9) , one obtains the final relation for the specific power of the multi-energetic source:

$$P = \sum_{i=1}^{k} \bar{E}_i \cdot BR_i \cdot a_i \tag{3.11}$$

Using the uncertainty propagation method, the total uncertainty of the specific power would be equal to:

$$u(P) = \sqrt{\sum_{i=1}^{k} [u^2(\bar{E}_i) + u^2(BR_i) + u^2(a_i)]} \tag{3.12}$$

3.4.3 Particles flux distribution analysis - Gamma radiation

In order to understand how the particles behave inside the calorimeter, the particle flux was checked using tally 4 [9] with the mesh option and normalized to 10^6 particles source strength, as said before. The flux was calculated on a XY mesh made of 10 000 rectangular cells, each 1.4cm wide and 188cm high. The flux was also determined along the Z axis, on a mesh made of 300 rectangular cells, 72cm wide and 0.6 cm high. The obtained 3D fluxes are illustrated in Figure 12. The fluxes were analysed for the three scenarios and three different source energies (0.1MeV, 1MeV and 5 MeV) as mentioned before. For the clarity of the results presented, the charts were zoomed up to the range of $(0,10^{-4})$ particles/cm^2.

a) Scenario I, 0.1 MeV

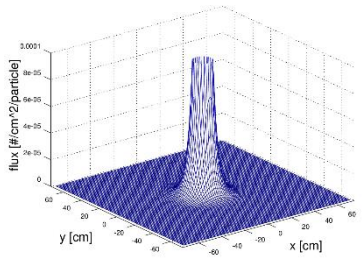

b) Scenario I, 1 MeV

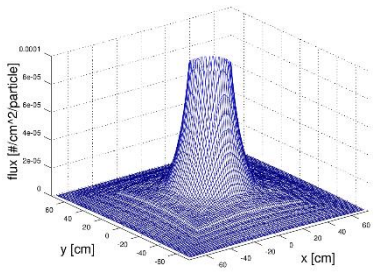

c) Scenario I, 5 MeV

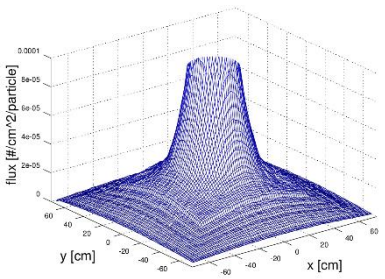

d) Scenario II, 0.1 MeV

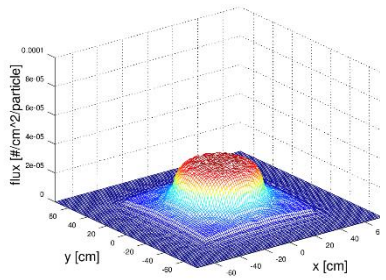

e) Scenario II, 1 MeV

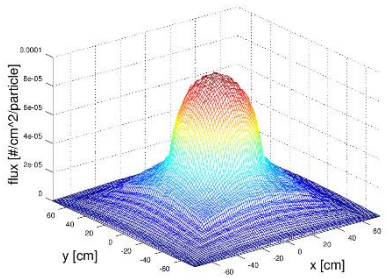

f) Scenario II, 5 MeV

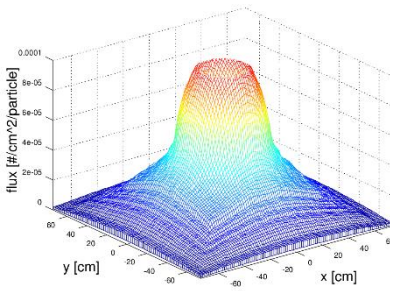

g) Scenario III, 0.1 MeV h) Scenario III, 1 MeV i) Scenario III, 5 MeV

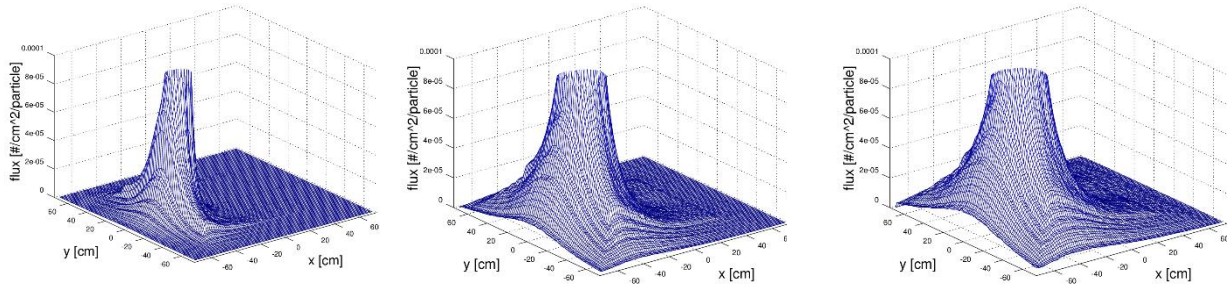

FIGURE 12. GAMMA PARTICLES FLUX (NORMALIZED TO 106 SOURCE PARTICLES) FOR DIFFERENT ENERGIES AND THE THREE SCENARIOS DISCUSSED IN THE TEXT.

The results confirm that for the 0.1 MeV source almost all the radiation is deposited inside the system. Despite all particles being absorbed and no radiation escaping the system, even for low energy gammas not all the heat is deposited inside the Peltier elements where it is detected. For the homogenous and least conservative scenario, still some step changes in the flux distribution are visible, reflecting the layers of the calorimeter, which means that some part of the radiation penetrates the detection zone and the homogenization and insulation parts. Only the heat deposited inside the drum and measurement parts are detectable, thus not all the total deposited energy can be measured. And for higher energies, certainly even more particles leave the system as expected.

The charts in Figure 12 are meant to be just illustrative. To quantify and compare the fluxes, especially the tails which describe the radiation leakage, two-dimensional charts are plotted along the X and Z axes, and Figure 13 shows a comparison of the fluxes for different energies for the case of the 2nd scenario whereas Figure 14 shows a juxtaposition of fluxes at mid-energy (i.e. 1MeV) for all three scenarios. Relative error shown in Table 9 and Table 10 is statistical uncertainty calculated automatically by MCNP.

a) b)

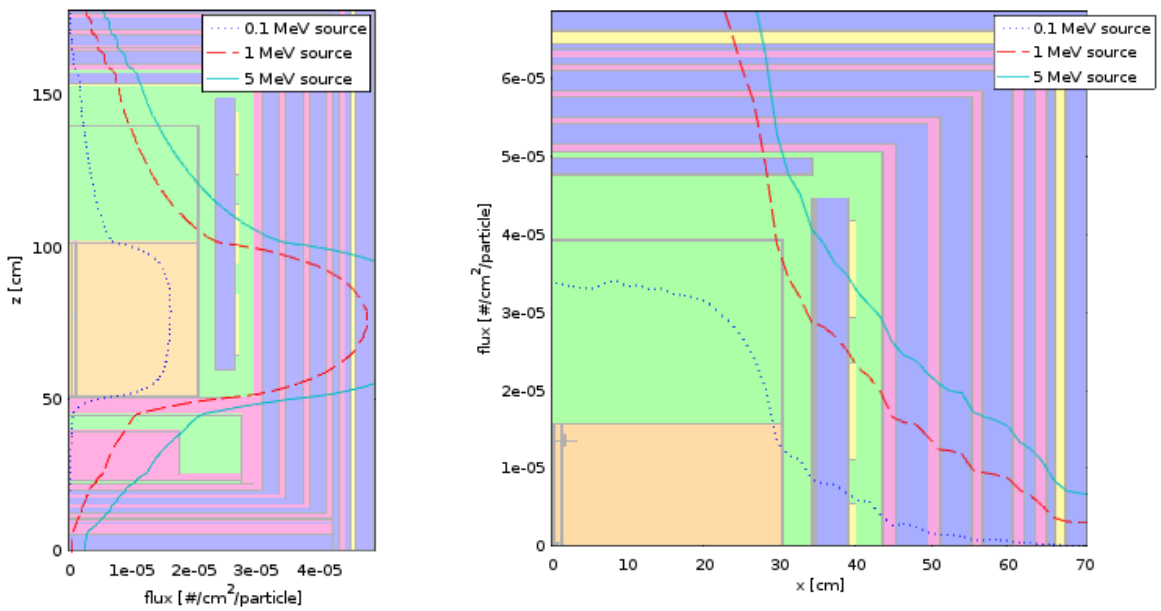

FIGURE 13. FLUX DISTRIBUTION FOR DIFFERENT ENERGIES IN Z- AND X-DIRECTION, HOMOGENOUS GAMMA SOURCE.

TABLE 9. RADIATION LEAKAGE FOR DIFFERENT ENERGIES, HOMOGENOUS GAMMA SOURCE.

	flux [particles/cm^2]							
	along Z-axis						**along X-axis**	
energy [MeV/par]:	**bottom:**	**rel. error:**	**top:**	**rel. error:**	**aluminium block:**	**rel. error:**	**flux:**	**rel. error:**
0.1	1.35E-09	22.0%	3.11E-08	6.4%	2.48E-07	2.7%	1.32E-07	25.9%
1	5.08E-07	1.9%	1.60E-06	1.0%	5.82E-06	0.5%	2.75E-06	4.3%
5	2.45E-06	0.6%	3.81E-06	0.6%	1.30E-05	0.4%	6.73E-06	2.6%

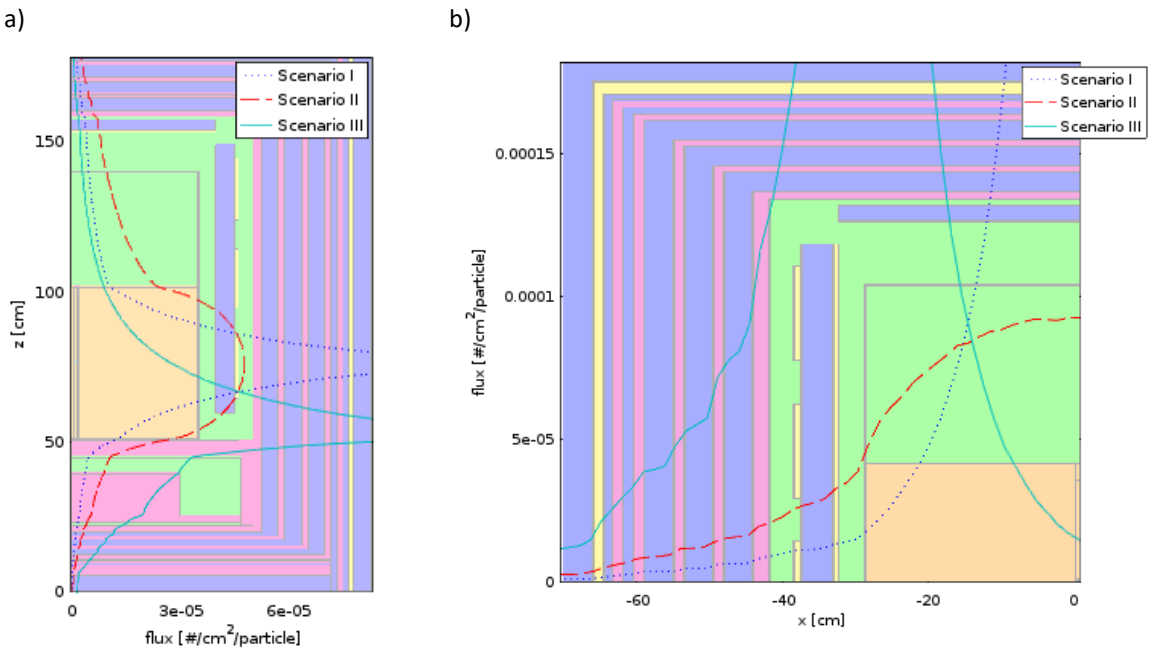

FIGURE 14. FLUX DISTRIBUTION FOR THE DIFFERENT SCENARIOS, 1MEV GAMMA SOURCE, 10^6 SOURCE STRENGTH.

One can see that the energy of the source has significant influence on the flux distribution. The flux plotted along Z axis (Figure 14a) shows that some part of it reaches the ghost chamber and beyond. For high energies, the flux penetrates more layers, as well as the reference parts of the calorimeter which causes inevitably a double bias.

TABLE 10. RADIATION LEAKAGE FOR DIFFERENT SCENARIOS, 1 MEV GAMMA SOURCE.

	flux [particles/cm^2]							
	along Z-axis						**along X-axis**	
scenario:	**bottom:**	**rel. error:**	**top:**	**rel. error:**	**aluminium block:**	**rel. error:**	**flux:**	**rel. error:**
I	1.93E-07	2.7%	4.63E-07	1.4%	2.48E-06	0.1%	9.47E-07	6.7%
II	5.08E-07	1.9%	1.60E-06	1.0%	5.82E-06	0.5%	2.75E-06	4.3%
III	1.76E-06	0.7%	2.13E-07	2.1%	2.03E-05	0.4%	1.07E-05	2.0%

The results show that source distribution pattern has a strong influence on the flux distribution. In case of the flux along X-axis (Figure 14b) and the source close to the wall of the drum, the flux leakage is around four times higher than compared to the homogeneous case and around 11 times higher compared to the most conservative scenario I.

3.4.4 Particles flux distribution analysis - Neutron radiation

Like for the gamma radiation, the neutron particles flux was simulated on the XY surface and along Z axis. Figure 15 presents illustrative 3D plots of the fluxes (normalized to 10^6 Bq source strength), for different scenarios and source energies. For the clarity of the results presented, the charts were zoomed up to the range of ($0{,}2\cdot10^{-4}$) particles/cm^2/s.

a) Scenario I, 0.1 MeV

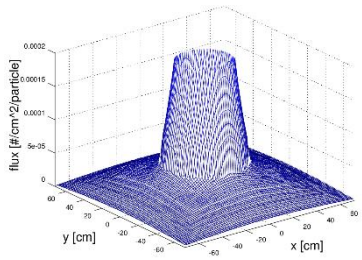

b) Scenario I, 1 MeV

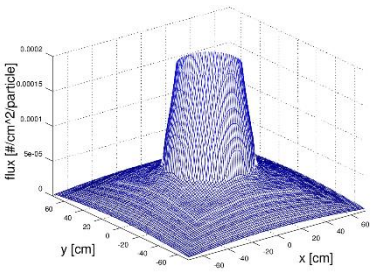

c) Scenario I, 5 MeV

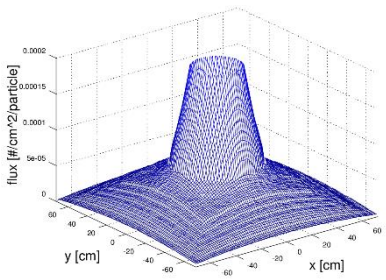

d) Scenario II, 0.1 MeV

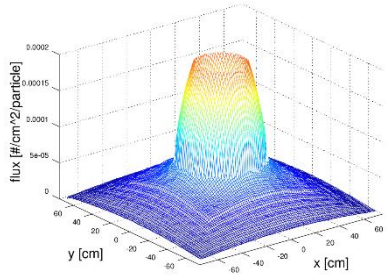

e) Scenario II, 1 MeV

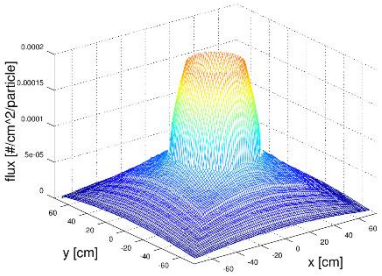

f) Scenario II, 5 MeV

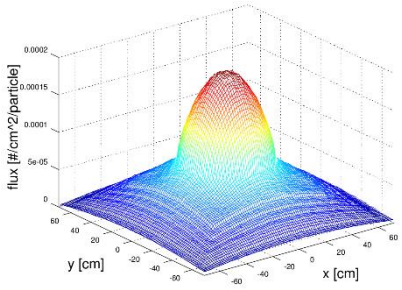

g) Scenario III, 0.1 MeV h) Scenario III, 1 MeV i) Scenario III, 5 MeV

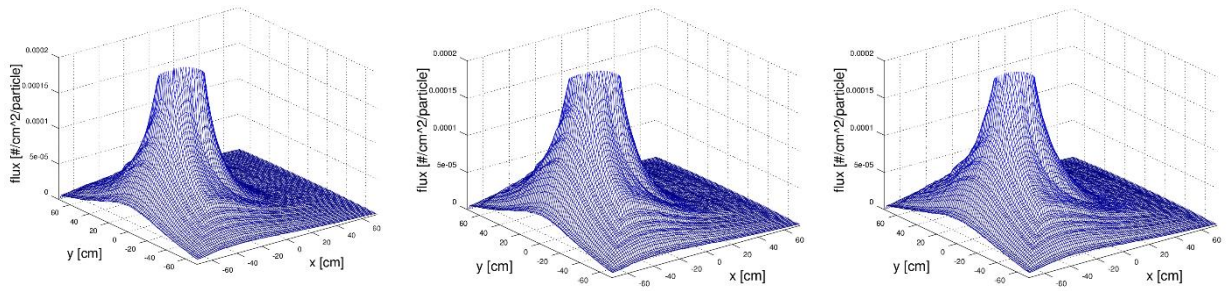

FIGURE 15. NEUTRON PARTICLES FLUX FOR DIFFERENT ENERGIES AND SCENARIOS.

One can see a different behaviour of the photon and neutron fluxes. In case of photons, source energy strongly influences the shape of the flux distribution, whereas neutrons flux is less sensitive for the source energy. For different energies the neutron flux distribution changes the shape slightly but the total flux that escapes the system is almost the same, as presented in the Figure 16 and TABLE 11. Only the position of the source can strongly influence the radiation leakage. However, the simulations show that, for the source placed in the centre of the drum and the uniformly distributed source, fluxes are very similar. Only for the source placed close to the edge of the drum, the radiation leakage and shape of the flux change significantly.

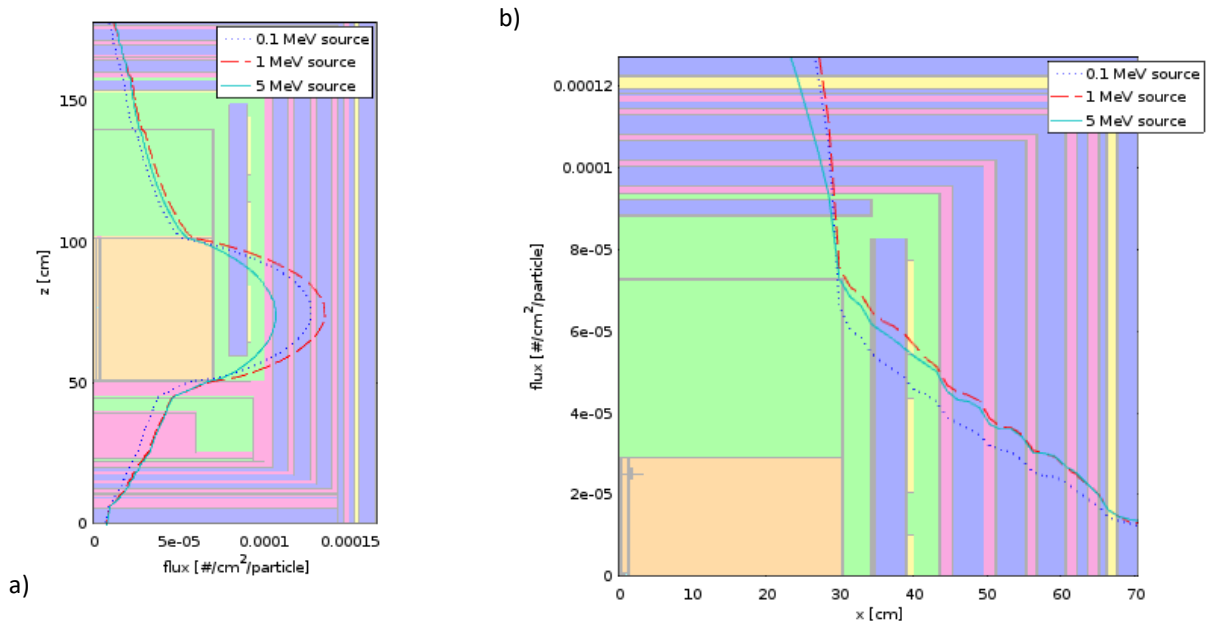

FIGURE 16. XZ-PLOT OF THE N-FLUX PROFILES FOR DIFFERENT ENERGIES, HOMOGENOUS NEUTRON SOURCE.

TABLE 11. NEUTRON RADIATION LEAKAGE FOR DIFFERENT SCENARIOS, 1 MEV NEUTRON SOURCE

	flux [particles/cm²]							
	along Z-axis						**along X-axis**	
energy [MeV/par]:	**bottom:**	**rel. error:**	**top:**	**rel. error:**	**aluminium block:**	**rel. error:**	**flux:**	**rel. error:**
0.1	7.12E-06	0.4%	4.66E-06	0.4%	2.68E-05	0.3%	1.15E-05	1.9%
1	7.74E-06	0.4%	5.50E-06	0.4%	3.33E-05	0.3%	1.28E-05	1.8%
5	7.97E-06	0.4%	5.78E-06	0.4%	3.40E-05	0.3%	1.33E-05	1.7%

a) b)

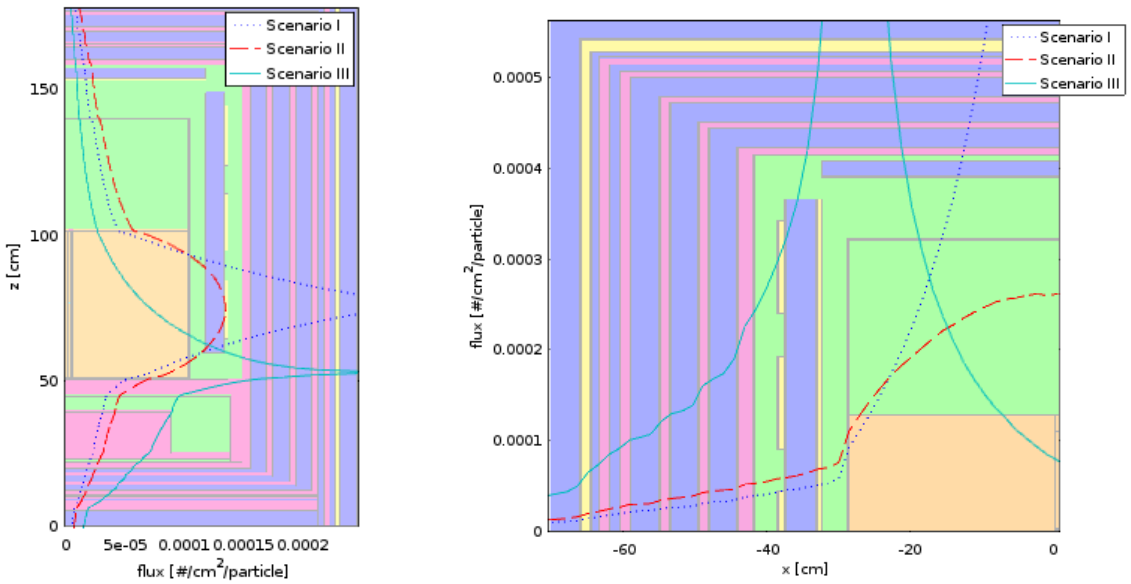

FIGURE 17. XZ-PLOT OF THE NEUTRON FLUX PROFILES FOR THE THREE DIFFERENT SCENARIOS, 1MEV NEUTRON SOURCE.

TABLE 12. NEUTRON RADIATION LEAKAGE FOR DIFFERENT ENERGIES, HOMOGENOUS NEUTRON SOURCE.

	flux [particles/cm²]							
	along Z-axis						**along X-axis**	
scenario:	**bottom:**	**rel. error:**	**top:**	**rel. error:**	**aluminium block**	**rel. error:**	**flux:**	**rel. error:**
I	5.99E-06	0.4%	4.17E-06	0.5%	2.44E-05	0.3%	1.01E-05	1.9%
II	7.74E-06	0.4%	5.50E-06	0.4%	3.33E-05	0.3%	1.28E-05	1.8%
III	1.58E-05	0.3%	2.21E-06	0.7%	7.38E-05	0.2%	3.96E-05	1.1%

As the total neutron flux and the radiation leakage are more-or-less constant, it may suggest that most of the neutrons are not absorbed rather scattered and potential absorption is partly recompensed by neutron-producing reactions, whereas the energy deposition depends on the secondary particles and calorimeter nuclei interactions.

Figure 2 shows that, within the range of the studied energies, the flux shape profiles and radiation leakage are almost independent of the energy of the source. Table 12 shows that the flux escaping the system and going through the aluminium block are fairly constant (maximum 25% changes).

3.5 Heat detection

3.5.1 Calorimeter's layers

Not all the heat is likely to be detected by the calorimeter's Peltier elements. In order to fully simulate what actually would be the heat measured by the device, the energy/heat deposition in all the layers was determined. Figure 18 presents a sketch of the calorimeter set-up with description of the layers.

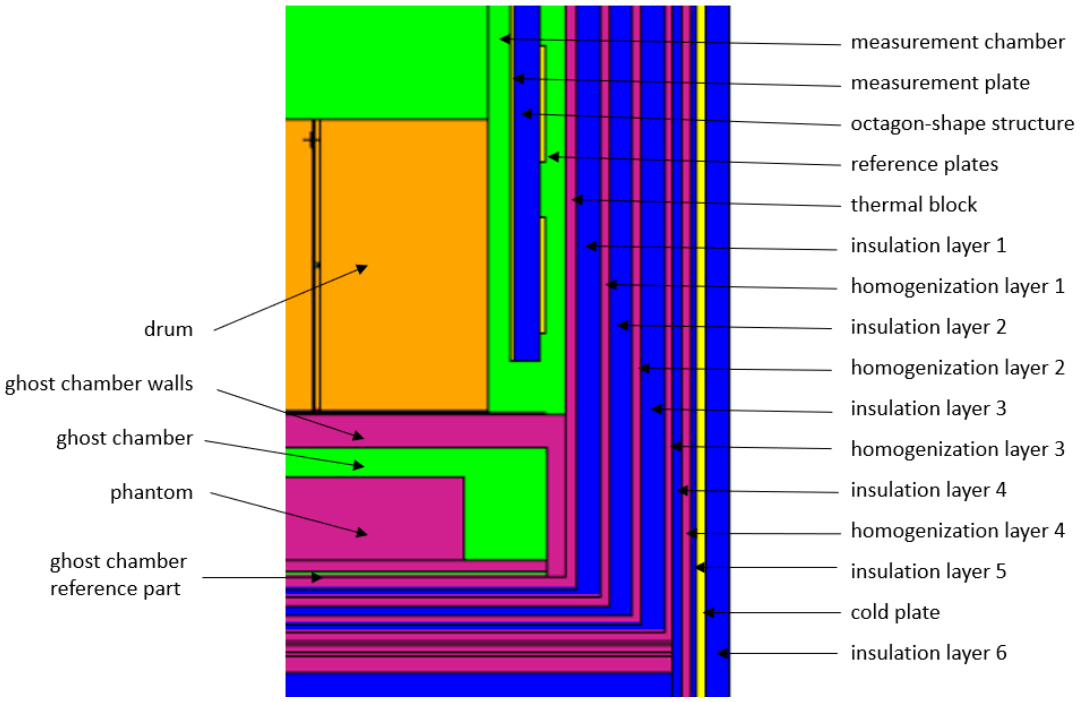

FIGURE 18. SKETCH OF THE LAYERS OF THE CALORIMETER.

The total energy deposition was simply calculated as the sum of all the energy depositions of the different layers. The following subsection contains the energy depositions, detailed by layer, for the three scenarios, at three different source energies (i.e. 100 keV, 1 MeV and 5 MeV).

As mentioned, the Peltier elements are placed on the measurement plates located around the measurement chamber, aside, below and above the sample. An additional measurement plate is located at the bottom of the ghost cell for the bottom reference measurement, while the reference Peltier elements are integrated in the other measurement plates. The total heat flux is the difference between the measurement signal corresponding to the

heat produced inside the drum and the reference signal which attempts to quantify the measurement noise. In case of high energies, radiation escaping from the measurement chamber can affect the accuracy of the measurement.

In the following part the energy deposition and its detection are discussed: The heat depositions inside the layers is split into three components: i) the heat detected by the measurement elements (coloured in green in Table 13 - Table 18), ii) the heat monitored in the ghost cell, which reduces the result (coloured in red in Table 13 - Table 18) and iii) the negligible parts of the heat deposition with no influence on the total power measurement (not coloured in Table 13 - Table 18). The final result is equal to:

$$E_{det} = E_{drum} + E_{mch} - E^{ref} - \left(E_{gch} + E_{ph} - E_{gch}^{ref}\right) \tag{3.13}$$

where E_{drum}, E_{mch}, E^{ref}, E_{gch}, E_{ph}, E_{gch}^{ref} (J or eV) are the energies deposited in the drum, measurement chamber, reference plates, ghost chamber, phantom and ghost chamber reference plate, respectively.

In case of the measurement chamber, only the heat produced inside the octagonal-shaped structure would be detected. The heat produced behind the measurement plates would not be detected. However, preliminary simulations showed that this heat has virtually no influence on the final measurement and, as an approximation, all the heat produced inside the measurement chamber is considered as detected.

TABLE 13. ENERGY DEPOSITION AT THE VARIOUS PARTS OF THE LVC CALORIMETER FOR DIFFERENT ENERGIES, 1ST SCENARIO, GAMMA SOURCE.

source energy [MeV/particle]:	0.1		1		5	
Layer:	energy deposition:	rel. error:	energy deposition:	rel. error:	energy deposition:	rel. error:
thermal block	0.1%	2.2%	2.5%	0.2%	3.9%	0.1%
insulation layer 1	0.0%	3.4%	0.0%	0.3%	0.0%	0.2%
homogenization layer 1	0.0%	3.5%	1.5%	0.3%	2.6%	0.2%
insulation layer 2	0.0%	0.0%	0.0%	0.3%	0.0%	0.2%
homogenization layer 2	0.0%	4.9%	1.2%	0.3%	2.3%	0.2%
insulation layer 3	0.0%	0.0%	0.0%	0.4%	0.0%	0.2%
homogenization layer 3	0.0%	6.8%	0.9%	0.3%	2.0%	0.2%
insulation layer 4	0.0%	0.0%	0.0%	0.4%	0.0%	0.2%
homogenization layer 4	0.0%	8.9%	0.7%	0.4%	1.8%	0.2%
insulation layer 5	0.0%	0.0%	0.0%	0.5%	0.0%	0.2%
cold plate	0.0%	0.0%	0.6%	0.5%	1.8%	0.2%
insulation layer 6	0.0%	0.0%	0.0%	0.5%	0.0%	0.2%
drum	99.6%	0.1%	87.3%	0.1%	67.3%	0.0%
measurement chamber	0.0%	0.0%	0.0%	0.2%	0.0%	0.2%
ghost chamber walls	0.1%	3.7%	1.8%	0.5%	3.1%	0.32%
ghost cell and phantom	0.0%	0.0%	0.2%	1.5%	0.5%	1.0%
ghost cell reference part	0.0%	0.0%	0.2%	1.0%	0.3%	0.52%

measurement plates	0.1%	2.0%	0.6%	0.2%	0.9%	0.1%
octagonal structure	0.0%	0.0%	0.0%	0.3%	0.0%	0.16%
reference plates	0.0%	5.6%	0.2%	0.6%	0.2%	0.4%
total:	**100.0%**	**0.1%**	**97.7%**	**0.1%**	**86.7%**	**0.1%**
detected:	**99.7%**	**0.1%**	**87.7%**	**0.1%**	**67.8%**	**0.1%**

As we can see from the Table 13, for low energy gamma radiation almost all the heat is deposited inside the drum and can be detected. Despite the source located is in the centre, for higher energies there is a notable part of the radiation which escape from the system and are not detected, thus the detection rate is significantly decreased to around 68%.

TABLE 14. ENERGY DEPOSITION AT THE VARIOUS PARTS OF THE LVC CALORIMETER FOR DIFFERENT ENERGIES, 1ST SCENARIO, NEUTRON SOURCE.

source energy [MeV/particle]:	0.1		1		5	
Layer:	energy deposition:	rel. error:	energy deposition:	rel. error:	energy deposition:	rel. error:
thermal block	0.1%	0.9%	0.4%	0.4%	3.7%	0.1%
insulation layer 1	0.0%	0.9%	0.2%	0.4%	0.3%	0.2%
homogenization layer 1	0.0%	0.9%	0.3%	0.4%	2.7%	0.2%
insulation layer 2	0.0%	1.0%	0.1%	0.4%	0.3%	0.2%
homogenization layer 2	0.0%	0.8%	0.2%	0.5%	2.5%	0.2%
insulation layer 3	0.0%	1.0%	0.1%	0.4%	0.2%	0.2%
homogenization layer 3	0.0%	0.8%	0.2%	0.5%	2.3%	0.2%
insulation layer 4	0.0%	1.1%	0.0%	0.5%	0.1%	0.2%
homogenization layer 4	0.0%	0.9%	0.2%	0.5%	2.0%	0.2%
insulation layer 5	0.0%	1.1%	0.0%	0.5%	0.0%	0.2%
cold plate	0.0%	0.8%	0.1%	0.5%	1.9%	0.2%
insulation layer 6	0.0%	0.8%	0.1%	0.4%	0.1%	0.1%
drum	99.1%	0.1%	94.6%	0.1%	60.7%	0.0%
measurement chamber	0.3%	0.2%	0.0%	0.2%	0.0%	0.1%
ghost chamber walls	0.1%	1.2%	0.3%	0.6%	3.0%	0.3%
ghost cell and phantom	0.1%	0.4%	0.1%	1.3%	0.5%	0.7%
ghost cell reference part	0.0%	2.2%	0.0%	1.1%	0.4%	0.4%
measurement plates	0.0%	1.2%	0.1%	0.4%	0.6%	0.2%
octagonal structure	0.0%	1.0%	0.1%	0.4%	0.2%	0.2%
reference plates	0.0%	2.6%	0.0%	0.9%	0.2%	0.4%
total:	**99.9%**	**0.1%**	**97.1%**	**0.1%**	**81.7%**	**0.1%**
detected:	**99.3%**	**0.1%**	**94.6%**	**0.1%**	**61.0%**	**0.1%**

Table 14 shows that almost 100% of the 100 keV neutron radiation is deposited inside the system. However, even for particles of relatively low energy and the source placed at the centre of the drum, the radiation can penetrate past the reference parts and cause a bias of around 0.7%. As expected for higher energies, the radiation leakage affects the measurement more and for a source of 5 MeV about 82% of its energy is deposited whereas only 61% is detected.

3.5.2 Homogenous source (scenario II: homogeneously distributed source)

TABLE 15. ENERGY DEPOSITION AT THE VARIOUS PARTS OF THE LVC CALORIMETER FOR DIFFERENT ENERGIES, 2ND SCENARIO, GAMMA SOURCE.

source energy [MeV/particle]:	0.1		1		5	
Layer:	energy deposition:	rel. Error:	energy deposition:	rel. Error:	energy deposition:	rel. Error:
thermal block	7.0%	0.3%	6.8%	0.1%	6.1%	0.1%
insulation layer 1	0.0%	0.5%	0.0%	0.2%	0.0%	0.1%
homogenization layer 1	2.5%	0.5%	4.0%	0.2%	3.9%	0.1%
insulation layer 2	0.0%	0.6%	0.0%	0.2%	0.0%	0.1%
homogenization layer 2	1.3%	0.7%	3.2%	0.2%	3.5%	0.1%
insulation layer 3	0.0%	0.9%	0.0%	0.2%	0.0%	0.1%
homogenization layer 3	0.7%	0.9%	2.5%	0.2%	3.1%	0.1%
insulation layer 4	0.0%	1.3%	0.0%	0.3%	0.0%	0.2%
homogenization layer 4	0.4%	1.2%	2.0%	0.2%	2.7%	0.2%
insulation layer 5	0.0%	2.0%	0.0%	0.3%	0.0%	0.2%
cold plate	0.2%	1.7%	1.7%	0.3%	2.7%	0.2%
insulation layer 6	0.0%	2.2%	0.0%	0.3%	0.0%	0.2%
drum	80.5%	0.1%	64.5%	0.1%	49.6%	0.1%
measurement chamber	0.0%	0.3%	0.0%	0.2%	0.0%	0.1%
ghost chamber walls	3.8%	0.5%	5.5%	0.3%	5.8%	0.3%
ghost cell and phantom	0.1%	3.7%	0.5%	1.1%	0.7%	0.9%
ghost cell reference part	0.0%	3.9%	0.0%	0.8%	0.0%	0.5%
measurement plates	2.7%	0.3%	1.9%	0.2%	1.6%	0.1%
octagonal structure	0.0%	0.3%	0.0%	0.2%	0.0%	0.1%
reference plates	0.6%	0.7%	0.4%	0.4%	0.4%	0.4%
total:	**99.8%**	**0.2%**	**93.2%**	**0.1%**	**80.3%**	**0.1%**
detected:	**82.5%**	**0.2%**	**65.5%**	**0.1%**	**50.2%**	**0.1%**

As expected, for the uniformly distributed radioactive material, the radiation leakage increases and not all the heat is detected. It is worthwhile to point out that even in the case of low energy gamma radiation (i.e. 100keV), and

despite almost 100% of the energy is deposited inside the system, more radiation penetrates the layers and only around 83% of the energy is detected. For higher energies, half of the energy may not be detected.

TABLE 16. ENERGY DEPOSITION AT THE VARIOUS PARTS OF THE LVC CALORIMETER FOR DIFFERENT ENERGIES, 2ND SCENARIO, NEUTRON SOURCE.

source energy [MeV/particle]:	0.1		1		5	
Layer:	energy deposition:	rel. Error:	energy deposition:	rel. Error:	energy deposition:	rel. Error:
thermal block	1.7%	0.3%	2.2%	0.2%	4.8%	0.1%
insulation layer 1	1.0%	0.3%	0.8%	0.2%	0.4%	0.1%
homogenization layer 1	0.8%	0.3%	1.4%	0.2%	3.5%	0.1%
insulation layer 2	0.9%	0.3%	0.7%	0.2%	0.4%	0.1%
homogenization layer 2	0.6%	0.4%	1.3%	0.2%	3.2%	0.1%
insulation layer 3	0.7%	0.3%	0.6%	0.2%	0.3%	0.1%
homogenization layer 3	0.4%	0.4%	1.1%	0.2%	3.0%	0.1%
insulation layer 4	0.2%	0.3%	0.2%	0.2%	0.1%	0.2%
homogenization layer 4	0.3%	0.4%	0.9%	0.2%	2.7%	0.1%
insulation layer 5	0.1%	0.3%	0.1%	0.3%	0.1%	0.2%
cold plate	0.3%	0.4%	0.8%	0.2%	2.5%	0.1%
insulation layer 6	0.4%	0.2%	0.3%	0.2%	0.2%	0.1%
drum	80.6%	0.1%	69.5%	0.1%	41.1%	0.1%
measurement chamber	0.3%	0.2%	0.0%	0.2%	0.0%	0.1%
ghost chamber walls	1.1%	0.5%	1.7%	0.3%	4.0%	0.2%
ghost cell and phantom	0.2%	0.8%	0.3%	0.8%	0.7%	0.6%
ghost cell reference part	0.1%	0.9%	0.2%	0.5%	0.5%	0.4%
measurement plates	0.5%	0.3%	0.4%	0.2%	0.8%	0.1%
octagonal structure	0.9%	0.3%	0.5%	0.2%	0.3%	0.1%
reference plates	0.1%	0.7%	0.1%	0.4%	0.2%	0.3%
total:	**91.2%**	**0.1%**	**83.1%**	**0.1%**	**68.8%**	**0.1%**
detected:	**82.1%**	**0.1%**	**70.3%**	**0.1%**	**41.7%**	**0.1%**

For the uniformly distributed particles and a 100 keV neutron source, around 9% of the energy escapes the system and 18% is not detected. For higher energies less than half of the energy escapes the calorimeter undetected.

3.5.3 Least conservative source (scenario III: source close to the edge of the drum)

TABLE 17. ENERGY DEPOSITION AT THE VARIOUS PARTS OF THE LVC CALORIMETER FOR DIFFERENT ENERGIES, 3RD SCENARIO, GAMMA SOURCE.

source energy [MeV/particle]:	0.1		1		5	
Layer:	energy deposition:	rel. Error:	energy deposition:	rel. Error:	energy deposition:	rel. Error:
thermal block	13.0%	0.2%	9.4%	0.1%	7.5%	0.1%
insulation layer 1	0.0%	0.3%	0.0%	0.2%	0.0%	0.1%
homogenization layer 1	4.5%	0.3%	5.2%	0.2%	4.6%	0.1%
insulation layer 2	0.0%	0.5%	0.0%	0.2%	0.0%	0.1%
homogenization layer 2	2.4%	0.5%	4.1%	0.2%	4.0%	0.1%
insulation layer 3	0.0%	0.7%	0.0%	0.2%	0.0%	0.1%
homogenization layer 3	1.3%	0.7%	3.2%	0.2%	3.4%	0.1%
insulation layer 4	0.0%	1.0%	0.0%	0.3%	0.0%	0.2%
homogenization layer 4	0.7%	0.9%	2.5%	0.2%	3.1%	0.1%
insulation layer 5	0.0%	1.4%	0.0%	0.3%	0.0%	0.2%
cold plate	0.3%	1.2%	2.1%	0.3%	3.1%	0.2%
insulation layer 6	0.0%	1.6%	0.0%	0.3%	0.0%	0.2%
drum	43.7%	0.1%	35.9%	0.1%	28.4%	0.1%
measurement chamber	0.0%	0.2%	0.0%	0.2%	0.0%	0.2%
ghost chamber walls	25.1%	0.2%	23.1%	0.1%	19.6%	0.2%
ghost cell and phantom	0.6%	1.4%	1.8%	0.6%	1.9%	0.5%
ghost cell reference part	0.0%	1.8%	0.0%	0.4%	0.0%	0.3%
measurement plates	7.2%	0.2%	3.7%	0.1%	2.8%	0.1%
octagonal structure	0.0%	0.4%	0.0%	0.3%	0.0%	0.3%
reference plates	0.5%	0.8%	0.3%	0.6%	0.3%	0.6%
total:	**99.6%**	**0.2%**	**91.5%**	**0.1%**	**78.9%**	**0.1%**
detected:	**49.9%**	**0.2%**	**37.5%**	**0.1%**	**29.1%**	**0.1%**

Table 17 shows that even a 100 keV gamma particle can escape the measurement parts and may not be detected. Although 99.6% of the energy is deposited in the different layers, nearly half of the heat is not detected. For higher energies this rate increases up to 62% for 1 MeV source and up to 71% for 5 MeV particles.

TABLE 18. ENERGY DEPOSITION AT THE VARIOUS PARTS OF THE LVC CALORIMETER FOR DIFFERENT ENERGIES, 3RD SCENARIO, NEUTRON SOURCE.

source energy [MeV/particle]:	0.1		1		5	
Layer:	energy deposition:	rel. Error:	energy deposition:	rel. Error:	energy deposition:	rel. Error:
thermal block	3.8%	0.2%	4.4%	0.1%	5.9%	0.1%
insulation layer 1	2.3%	0.2%	1.4%	0.1%	0.4%	0.1%
homogenization layer 1	1.8%	0.2%	2.9%	0.1%	4.1%	0.1%
insulation layer 2	1.9%	0.2%	1.2%	0.1%	0.4%	0.1%
homogenization layer 2	1.3%	0.2%	2.6%	0.1%	3.8%	0.1%
insulation layer 3	1.6%	0.2%	1.1%	0.2%	0.4%	0.1%
homogenization layer 3	1.0%	0.2%	2.2%	0.1%	3.4%	0.1%
insulation layer 4	0.5%	0.2%	0.4%	0.2%	0.1%	0.2%
homogenization layer 4	0.8%	0.3%	1.8%	0.2%	3.0%	0.1%
insulation layer 5	0.3%	0.2%	0.2%	0.2%	0.1%	0.2%
cold plate	0.7%	0.3%	1.7%	0.2%	2.9%	0.1%
insulation layer 6	1.0%	0.2%	0.6%	0.1%	0.2%	0.1%
drum	50.5%	0.1%	40.0%	0.1%	23.3%	0.1%
measurement chamber	0.1%	0.3%	0.0%	0.2%	0.0%	0.1%
ghost chamber walls	7.5%	0.2%	7.8%	0.1%	10.2%	0.1%
ghost cell and phantom	0.6%	0.5%	1.2%	0.4%	1.6%	0.4%
ghost cell reference part	0.5%	0.4%	0.9%	0.3%	1.2%	0.2%
measurement plates	1.5%	0.2%	0.9%	0.1%	1.1%	0.1%
octagonal structure	1.1%	0.3%	0.6%	0.2%	0.2%	0.2%
reference plates	0.1%	0.7%	0.1%	0.5%	0.2%	0.5%
total:	**78.9%**	**0.1%**	**72.0%**	**0.1%**	**62.6%**	**0.1%**
detected:	**53.0%**	**0.1%**	**41.2%**	**0.1%**	**24.1%**	**0.1%**

One can see in Table 18, that for the neutron source close to the drum edge, the radiation leakage is very important. Even for a 100 keV source 21% of the energy leaves the system and only one half is detected. For 5 MeV source, the total heat deposition is around 63% and only ¼ of the energy is detected.

The results showed that a part of gamma radiation of energies higher than 100 keV is not deposited inside the LVC calorimeter, especially when the radiation source is placed nearby the edge of the drum (i.e. homogenous and least conservative sources). Despite a good part of the energy being deposited inside the calorimeter chamber, some gamma radiation penetrates the outer layers and escapes. Some other part of radiation may also be deposited inside the reference parts of the calorimeter and cause a double-bias, as it would be recognized as the reference level and thus decrease the measured signal. To summarize, the total simulated errors of the measurement for each of the scenarios at different energies are presented in Figure 19.

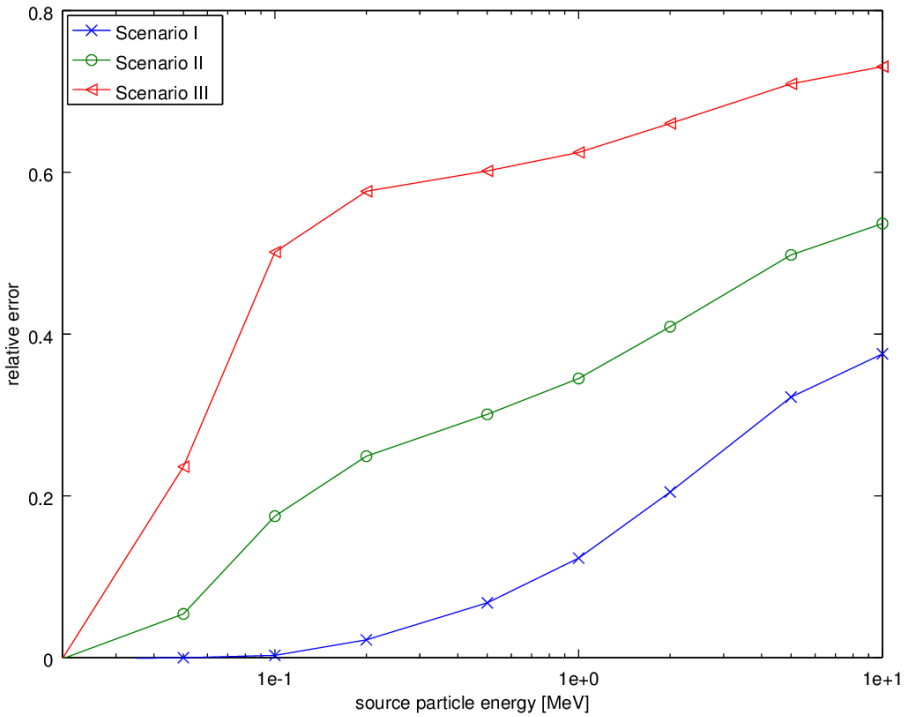

FIGURE 19. TOTAL MEASUREMENT ERROR FOR DIFFERENT SCENARIOS AND ENERGIES. GAMMA RADIATION.

One can see that the total error of the measurement, connected with the penetrative character of the gamma radiation, is more or less proportional to logarithm of the source energy. As for the energy deposition and detection probability, the results suggest that even for a 50 keV gamma source placed close to the edge of the drum around 24% of the emitted energy cannot be detected. For the least conservative scenario at the highest simulated energy, even around 73% escapes detection.

TABLE 19. THE TOTAL HEAT DETECTION. GAMMA RADIATION.

scenario:	I		II		III	
source energy [MeV]:	detection:	rel. error:	detection:	rel. error:	detection:	rel. error:
0.01	100.0%	0.1%	100.0%	0.1%	100.0%	0.1%
0.02	100.0%	0.1%	100.0%	0.1%	100.0%	0.1%
0.05	100.0%	0.1%	94.6%	0.1%	76.4%	0.2%
0.1	99.7%	0.1%	82.5%	0.2%	49.9%	0.2%
0.2	97.8%	0.1%	75.1%	0.1%	42.3%	0.2%
0.5	93.2%	0.1%	69.9%	0.1%	39.8%	0.1%
1	87.7%	0.1%	65.5%	0.1%	37.5%	0.1%
2	79.5%	0.1%	59.1%	0.1%	34.0%	0.2%
5	67.8%	0.1%	50.2%	0.1%	29.1%	0.1%
10	62.4%	0.1%	46.3%	0.1%	26.9%	0.1%

An extended version of the chart above is listed in Table 19. This table contains the total detected energy for each of the scenarios at energies between 10 keV - 10 MeV. The results from a simplified geometric set-up demonstrate the different influence of the radiation escape rate due to subtle variations in the layers geometry and material composition of the embedding matrix.

3.5.4 Neutron radiation

The simulations showed that, as expected, neutron particles are more penetrative than gamma radiation, therefore the errors associated with heat produced by neutron interactions are of course higher, as they deposit energy outside the drum and the measurement chamber. Figure 20 shows the total measurement error depending on the scenario and energy of the source. The error was calculated as relative part of the energy that would not be detected:

$$Err = 1 - \frac{E_d}{E_e} \tag{3.14}$$

Where E_d is the detected energy (eV) and E_e is the emitted energy (eV).

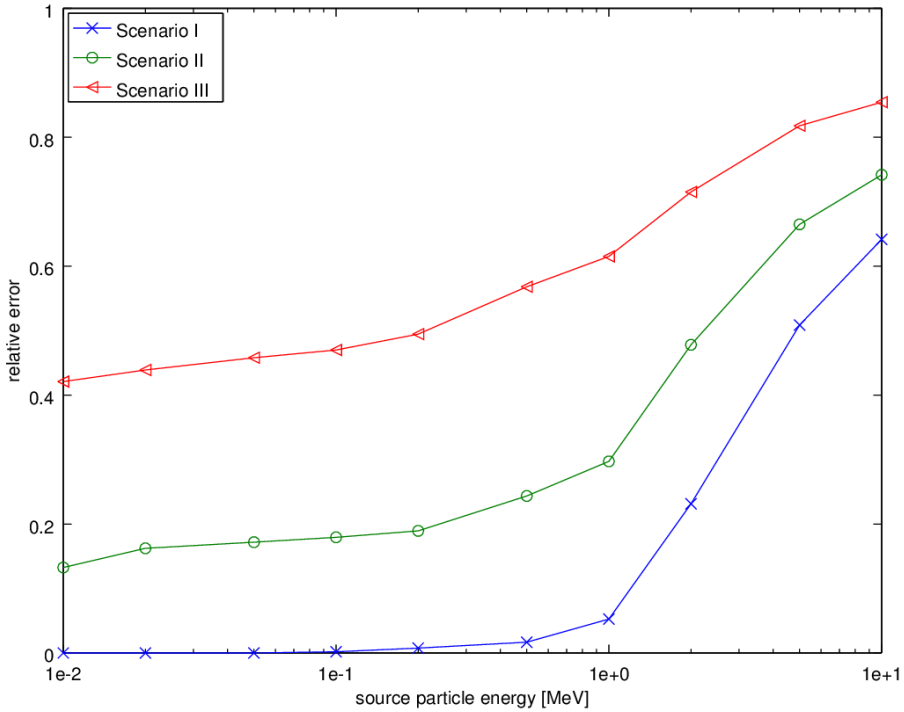

FIGURE 20. TOTAL MEASUREMENT ERROR FOR DIFFERENT SCENARIOS AND ENERGIES. NEUTRON RADIATION.

One can see that even for low energies the error can be around 40%. It increases significantly for energies > 1 MeV and 10 MeV source it can be around 60-85%.

TABLE 20. THE TOTAL HEAT DETECTION. NEUTRON RADIATION.

scenario:	**I**		**II**		**III**	
source energy [MeV]:	**detection:**	**rel. error:**	**detection:**	**rel. error:**	**detection:**	**rel. error:**
0.01	100.0%	0.1%	86.7%	0.1%	57.9%	0.1%
0.02	100.0%	0.1%	83.8%	0.1%	56.1%	0.1%
0.05	100.0%	0.1%	82.8%	0.1%	54.2%	0.1%
0.1	99.3%	0.1%	82.1%	0.1%	53.0%	0.1%
0.2	99.0%	0.1%	81.1%	0.1%	50.5%	0.1%
0.5	98.3%	0.1%	75.6%	0.1%	43.2%	0.1%
1	94.7%	0.1%	70.3%	0.1%	38.5%	0.1%
2	76.9%	0.1%	52.2%	0.1%	28.5%	0.1%
5	49.1%	0.1%	33.5%	0.1%	18.2%	0.1%
10	35.8%	0.1%	25.8%	0.1%	14.6%	0.1%

Table 20 shows the total detection rate for three scenarios at various energies. One can see that in case of neutrons all heat is detected only for the most conservative scenario and at energies < 100 keV. Nevertheless, it is worth remembering that for the calculations of values presented in the Figure 20 and Table 20 total absorption of neutrons of energy below 1 eV was assumed.

3.6 Spectrum overlapping

It may happen that a waste drum will contain high-energy gamma radiation emitters (e.g. Cs-137, Co-60). Then, while these elements will be easily detected by gamma spectrometry, their spectrum may cover other peaks originating from other isotopes. To illustrate the spectrum overlapping an MCNP simulation was performed for the ANDRA vector containing Cm-244, Am-241, Tc-99, plutonium isotopes and Cs-137 (Table 21).

TABLE 21. ANDRA'S VECTOR NO 1.

isotope	abundance
Cm244	26,1%
Pu239	2,3%
Pu240	2,5%
Pu238	12,1%
Am241	46,7%
Cs137	9,2%
Tc99	1,1%

The spectrum of radiation that leaves the drum is shown below. 662 keV peak from Cs-137 and the radiation from the interaction of these particles with the material of the matrix and drum are the more important. Some peaks may not be detected for three reasons (see Figure 21):

- because of too low energy, some particles are not able to leave the matrix and the drum at all and will not contribute to the spectrum
- because of Cs-137 peak interaction with matter, which can cover other peaks. The main part of the spectrum comes from Compton scattering, i.e. scattering of the 662keV gamma particles on the electrons in the matrix.
- because of too little statistics, for high-energy particles that manage to leave the drum, however, it happens too rarely to allow characterization of the isotope on this basis

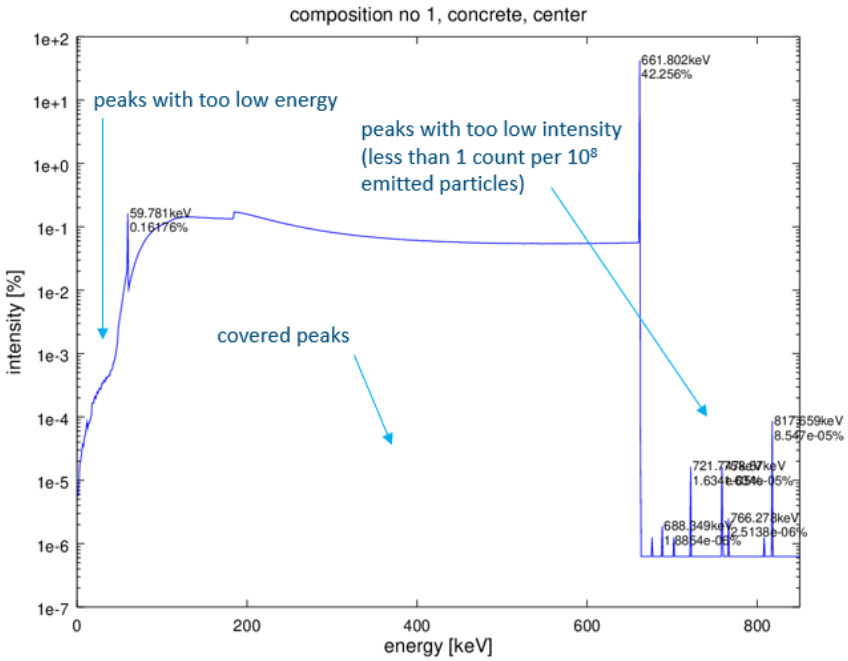

FIGURE 21. SPECTRUM FOR ANDRA'S VECTOR NO 1.

The isotopes that could be characterized based on selected peaks are presented below (Pu240, Pu239 and Tc99 were not characterized). Based on the analysis of individual peaks, the equivalent mass was determined, and then, based on these masses, the percentage share of each isotope was determined (Table 22).

TABLE 22. CALCULATION OF PERCENTAGE SHARE FOR ANDRA'S VECTOR NO 1.

isotope	E [keV]	counts	intensity [%]	BR [%]	activity [Bq/g]	equivalent mass [g]:	measured	real
Cm244	758.57	2.60E+01	1.63E-05	1.27E-05	3.03E+12	6.19E-02	30.0%	26.1%
Pu238	766.28	4.00E+00	2.51E-06	2.20E-05	6.34E+11	2.63E-02	12.7%	12.1%
Am241	721.75	2.60E+01	1.63E-05	1.96E-04	1.27E+11	9.58E-02	46.4%	46.7%
Cs137	661.80	6.72E+07	4.23E+01	8.51E+01	3.21E+12	2.26E-02	10.9%	9.2%

Table 22 present selected single peaks for the isotopes that could be characterized (the spectrum allowed characterization). The columns contain respectively: name of the isotope, energy of the peak, number of counts in the simulation (per $4{\cdot}10^8$ total simulated particles), peak intensity, branching ration (probability of emission of a particle with the given energy per decay), activity of the given isotope, mass that was calculated using formula (3.2), share of a given isotope (based on the calculated basses) and expected masses.

Then, for the determined composition the effective thermal power $P_{eff} = \sum_i P_i \cdot R_i = 987 mW/g$ was calculated. A simulation of energy deposition in the drum was performed and a thermal power emitted by the drum $\mathrm{W} = 854\mathrm{mW}$ was obtained. It gives the mass $m = \frac{W}{P_{eff}} = \frac{854\ mW}{987\ mW/g} = 0.87g$ of radioactive material. Table 23 shows the summary of the results compared with the simulated composition. One can see that masses of the isotopes were determined with relative error below 15%. Three isotopes: Pu239, Pu240 and Tc99 were not characterized due to overlapping of their spectrum with Cs137 spectrum.

TABLE 23. SUMMARY OF THE RESULTS - ANDRA VECTOR NO 1.

isotope	measured	u(Ri)	mass [g]	u(m) [g]	real mass [g]	diff [g]	diff [%]
Cm244	30%	1%	0.262	0.003	0.261	-0.001	0%
Pu238	13%	3%	0.111	0.004	0.121	0.009	8%
Am241	46%	2%	0.405	0.007	0.467	0.062	15%
Cs137	11%	4%	0.095	0.003	0.092	-0.003	3%
Pu240	0%	-	0.000	-	0.025	-	-
Pu239	0%	-	0.000	-	0.023	-	-
Tc99	0%	-	0.000	-	0.011	-	-
total	100%		0.873	0.033	1.000	0.127	15%

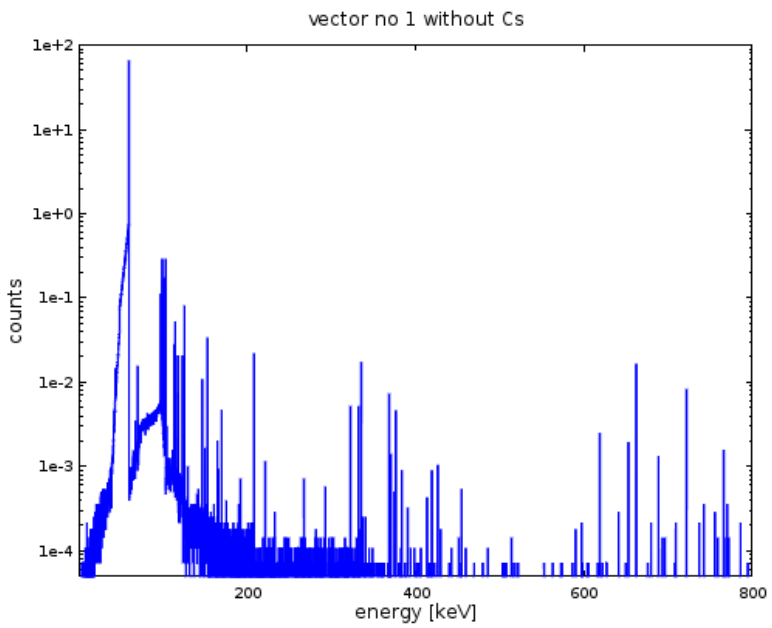

FIGURE 22. SPECTRUM FOR ANDRA'S VECTOR NO 1, WITHOUT CS-137.

Additionally, the simulations were performed without Cs-137 (Figure 22). By comparing the intensity of the peaks, it can be concluded that, to be able to analyse other isotopes, the mass content of Cs-137 should not exceed 0.01%. For vectors with a higher concentration of this isotope, other methods should be used, e.g. based on neutron techniques.

3.7 Andra vectors no 3 and 4

Spectrometric simulations were performed for the remaining Andra vectors 3 and 4. These vectors, however, contain a significant amount of gamma emitters - Am-241 and most of all Cs-137, the spectrum of which covers most of the peaks and only this isotope is recognized. Hence, doing an exercise on the combination of techniques would not be very interesting, as the gamma spectrometry would only be sensitive to the main gamma emitters, while not providing any information on the other isotopes, while neutron measurements or calorimetry would only be sensitive to another subset of isotopes. Without any strong prior correlation between the gamma emitters and

the heat producing/neutron emitting isotopes, any combination of techniques would then be the equivalent of taking the gamma measurement results for the gamma emitters, and neutron/calorimeter measurement results for the others, without further potential reductions of uncertainty. Thus, vectors 3 and 4 have not been more deeply investigated concerning the use of calorimetry in the characterization of radioactive waste. The results would be rather similar to those of the other vectors, with the exception that good a priori knowledge on the vector would be required, as gamma spectrometry cannot inform us about that in this case. Spectra that could be measured outside the drum are presented in Figure 23 and Figure 24.

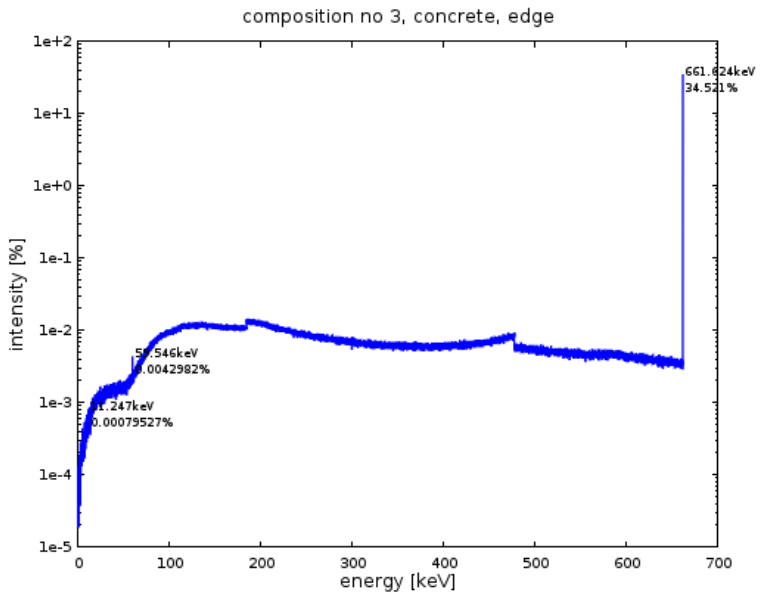

FIGURE 23. SPECTRUM FOR ANDRA'S VECTOR NO 3

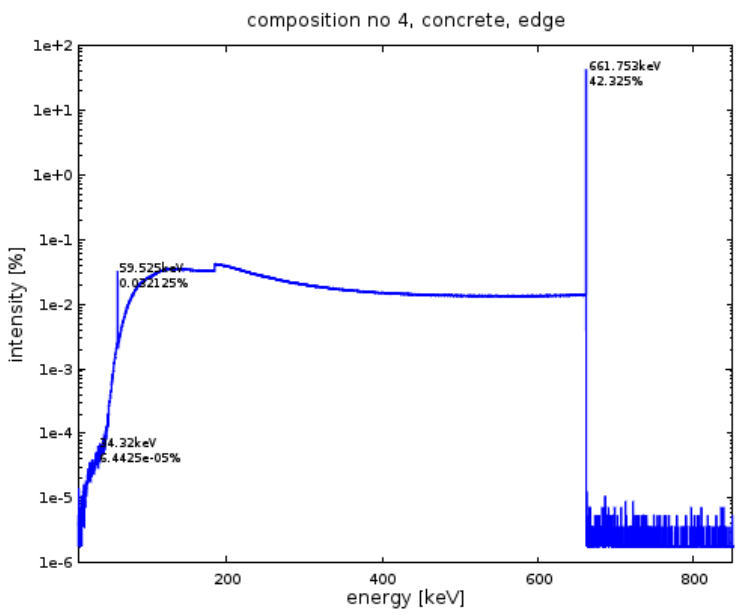

FIGURE 24. SPECTRUM FOR ANDRA'S VECTOR NO 4.

3.8 Radiation influence on electronics and materials in the LVC-CHANCE calorimeter

In this part the influence of gamma and neutron radiation on electronics and materials inside the calorimeter was estimated using available literature. As the most fragile parts in the point of view of calorimetric measurement are Peltier elements, influence of radiation on bismuth telluride was studied first, but other materials that build up the calorimeter were considered too, namely aluminium and polyethylene. For each nuclear vector the dose rate was simulated using the ICRP (international Commission on Radiological Protection) phantom modelled as 30x30x15cm homogenized block made of O (76.2%), C (11.1%), H (10.1%) and N (2.6%) [10]. The phantom was considered to be placed next to the drum, 50cm from the drum and 100cm from the drum. Two different locations of the source were considered: centre and edge of the drum. Table below shows the dose rate calculated using the Geant4 code.

TABLE 24. DOSE RATE FOR ANDRA'S VECTORS.

dose rate, mix no 1		
phantom position	source position (1g of radioactive material)	
	Centre	edge
next to the drum	13 uGy/h	2.0 mGy/h
0.5m from the drum	2 uGy/h	0.5 mGy/h
1m from the drum	3 uGy/h	0.2 mGy/h

dose rate, mix no 2		
phantom position	source position (1g of radioactive material)	
	centre	edge
next to the drum	0.1 uGy/h	0.7 mGy/h
0.5m from the drum	-	0.3 mGy/h
1m from the drum	-	0.1 mGy/h

dose rate, mix no 3		
phantom position	source position (1g of radioactive material)	
	Centre	edge
next to the drum	0.2 Gy/h	9.9 Gy/h
0.5m from the drum	28 mGy	1.6 Gy
1m from the drum	13 mGy/h	0.6 Gy/h

dose rate, mix no 4		
phantom position	source position (1g of radioactive material)	
	centre	edge
next to the drum	62 mGy/h	5.8 Gy/h
0.5m from the drum	16 mGy/h	1.0 Gy/h
1m from the drum	6.4 mGy/h	0.4 Gy/h

Vectors 3 and 4 are characterized by the highest dose rate (up to almost 10 Gy/h/g), however, these vectors contain mainly Cs-137 and the dose rate comes mainly from the emission of the 662keV gamma particles. For vectors 1 and 2 the dose rate is below 2mGy/h/g. The simulated dose rate may indicate the maximum radiation dose that Peltier elements and other parts of the calorimeter may receive. As shown in the table above, depending on the drum composition, source location and distance from the considered materials, the dose received by the calorimeter elements should not exceed 10Gy per year for vectors 1, 2 and 10kGy per year for vectors 3, 4 (assuming the average dose rates from the table). The table below shows the effects of gamma and neutron radiation on bismuth telluride, aluminium and polyethylene. These materials are the main building materials for the calorimeter. The data are based on the literature and show doses representing many years of exposure to the calorimeter; however, they can still be a certain indicator of the potential influence of radiation on the performance of the calorimeter components. These effects require further experimental verification.

TABLE 25. RADIATION INFLUENCE ON THE CALORIMETER'S MATERIALS.

	Gammas			Neutrons		
	Dose	effects	ref	Fluence/flux	effects	ref
aluminium	206 kGy (Co-60) 0-150kGy	dramatic change in surface morphology, decreased corrosion resistance (in demineralized water) no change in crystal structure	[11] [12]	10^{23} neutrons/ cm^2 (E > 0.1MeV)	strength increases were measured at test temperatures in the range 25 to 200°C, loss of ductility, transmutation-produced silicon was found to cause about 1.1% internal swelling Potential activation, (n, gamma) reaction, <10^4 neutrons/cm^2/s per 1g	[13]
bismuth telluride	50kGy-100kGy	(synthesized Bi2Te3 nanoparticles), increase in crystallite size and a decrease in the micro strain, atomic percentage of tellurium decrease with the increasing dose	[14]	10^{18} n/cm^2 (E > 0.1 MeV)	for n-type material power factor higher at lower temperatures, for the p-type materials, Seebeck coefficient not affected by irradiation, electrical resistivity decreased slightly	[15]
polyethylene	20kGy - 750kGy	HDPE (0.950 g/cm3), improvement in mechanical strength properties as dose increases, predominance of cross-linking over oxidative degradation	[16]	10^{10}-10^{13} n/cm^2/s 10^{16}-10^{18} n/cm^2	Increase in electrical resistance PET films, degradation of the chemical structure and the creation of new chromophores neutrons moderation, low activation	[17] [18]

While single measurements lead to small doses and therefore slight changes in the structure and properties of the materials used in the calorimeter, the accumulation of the dose over the years may lead to certain changes, especially in the most extreme scenario in which the measured waste drums contain a lot of high-energy gamma (e.g. Cs-137, Co-60, Am-241) emitters or neutron emitting isotopes (e.g. Cm-244) located near the edge of the drum. Even though these scenarios are unlikely and the dosages under consideration are highly overestimated, it would be advisable for the calorimeter to undergo recurring calibration to avoid variations due to potential changes in material properties of the Peltier elements and other parts of the calorimeter.

3.9 Conclusions with respect to the calorimeter modelling

The simulations performed confirm that calorimetry can be a complementary method to the standard non-destructive methods for the characterization of radioactive materials. Calorimetry can reduce the characterization error and/or identify additional materials inside the drum that have not been detected by other methods. Nevertheless, the analyses performed may suggest some problems related to the characterization of large-volume heterogeneous forms of radioactive waste drums. These are:

- the effects of radiation attenuation, then some of the isotopes may not be recognized or their amount may be incorrectly estimated,
- the effects of radiation leakage for which the calorimetric measurement may be disturbed due to penetration of the calorimeter and energy deposition, especially in the reference elements,
- the presence of high energetic gamma emitters, which are easy to characterize, but their spectrum can potentially cover the spectrum from isotopes with lower gamma emission, meaning there is some loss of information on the isotopic vector, which is very important for a neutron or calorimeter measurement,
- degradation of the calorimeter elements, which may cause changes in the operation of Peltier elements over the years, however, these effects require further experimental verification

Four nuclear vectors provided by ANDRA were considered in the simulations. Vectors 1 and 2 mainly consist of alpha and gamma emitters, and as the simulations have confirmed, this radiation is not able to escape from the matrix and drum wall, so they deposit all energy inside the waste and are suitable for calorimetric analysis. Additionally, these vectors contain Am-241 which, using the infinite energy method, can be used for self-attenuation analysis and improve radionuclide mass/activity estimation. In the case of vectors 3 and 4 there is a greater amount of gamma emitters, which cover any gamma peaks from neutron/heat producing isotopes. Therefore, in those cases, a characterization exercise would come down to independent gamma/neutron/calorimeter characterization of subsets of isotopes, where a priori information on the complete isotopic vector would be very important.

4 Probabilistic modelling for the CEA experiments

4.1 Introduction

Gamma-ray spectrometry is often employed with other measurement techniques such as passive neutron coincidence counting (PNCC) that brings information concerning plutonium isotopes with even mass numbers, 238,240,242Pu [19, 20]. Gamma-ray spectrometry can also be used with calorimetry, but given the complexity of calorimetric measurement, this technique is usually used for measuring small volumes [21]. However, being in principle free of bias and offering a high accuracy, calorimetric measurements are a very interesting solution for characterizing large volume radioactive waste drums [22, 23, 24, 25]. To estimate the added value of calorimetry regarding uncertainties reduction, plutonium samples have been introduced in different positions inside a concrete mock-up drum with holes. Calorimetry, PNCC and gamma spectroscopy measurements are coupled together using a Bayesian frame. Previous studies [26, 27, 28, 29, 30] showed that this probabilistic approach is indeed interesting since it allows fusing all available information within a coherent frame. Also, such a Bayesian frame allows handling uncertainties in a natural way.

4.2 Measurements presentation

4.2.1 Calorimeter description

The large size calorimeter called CHANCE LVC (Large Volume Calorimeter) shown in Figure 1 developed and built by KEP Technologies allows measurements of radioactive waste drums having volumes up to 220 L. the CHANCE LVC measures a differential heat-flow between the waste drum and a reference sample having a calorific capacity similar to the waste drum and kept at a constant temperature.

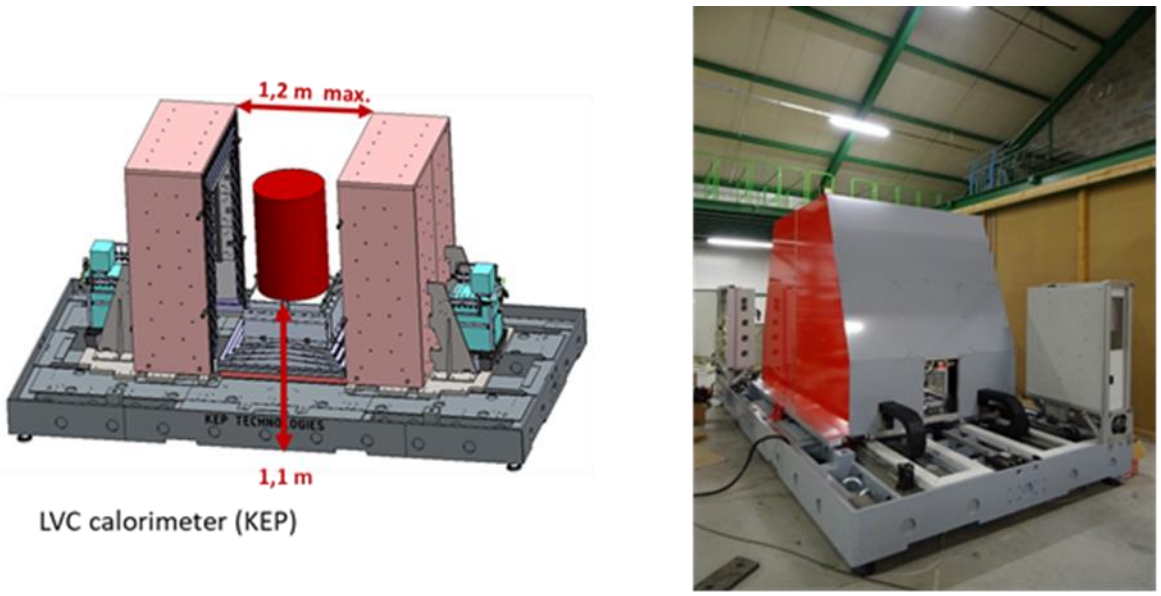

FIGURE 25. CAD VIEW AND REAL PICTURE OF THE LVC CHANCE CALORIMETER.

Peltier elements placed at different positions convert the heat fluxes associated to the waste and the reference sample into voltage signals V_i. Because the signal related to the heat flux is weak and subjected to various sources

of noise, such as temperature fluctuations in the experimental hall, a differential measurement is implemented to significantly cancel out the noise. In addition to the measurement cell, ghost cells are arranged in symmetrical configurations inside the calorimeter and act as reference cells (Figure 2). Simultaneous measurements of the sample and reference voltages permit a differential cancellation of noise and offsets. As the calorimeter consists of two shells and the base, each of these parts contains its own measurement system and the output of the calorimeter at a given time is the sum of all three signals:

$$V_s = \sum_{l,c,r} \left(V_i^{\text{meas}} - V_i^{\text{ref}}\right) \tag{1}$$

where l, c and r stand for the left, centre and right parts of the calorimeter, V_i^{meas} and V_i^{ref} are respectively the signals registered by the measuring sensors and reference sensors.

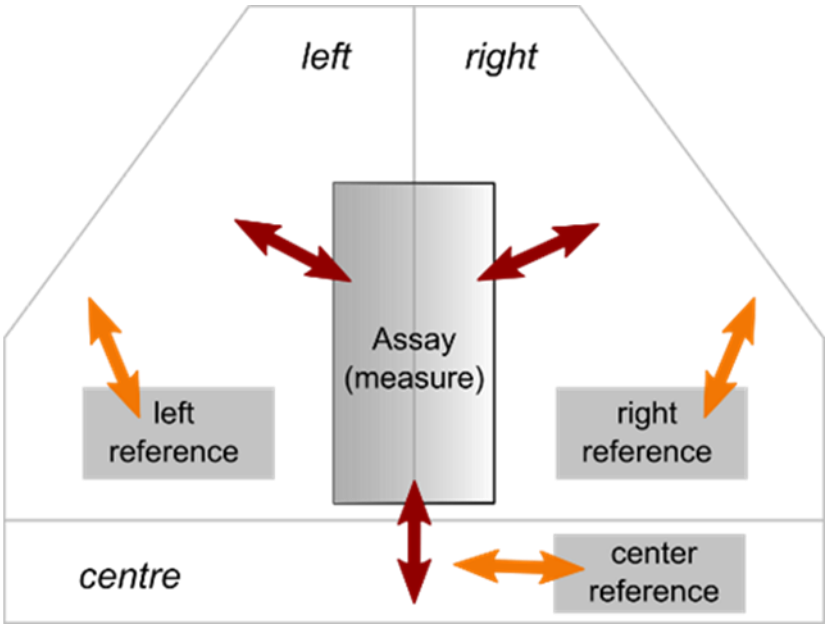

FIGURE 26. THERMAL TRANSFERS BETWEEN THE NUCLEAR ASSAY AND THE LEFT, RIGHT AND CENTRE PARTS OF THE CALORIMETER (NOT TO SCALE). EACH ARROW DEPICTS HEAT FLUXES INSIDE THE CALORIMETER (BROWN ARROWS REPRESENT HEAT FLUXES BETWEEN THE DRUM AND THE MEASURING PELTIER ELEMENTS, ORANGE ARROWS REPRESENT HEAT FLUXES BETWEEN REFERENCE PELTIER ELEMENTS AND CALORIMETER SHELLS AND BASE HEATED BLOCKS. THESE FLUXES GENERATE INDEPENDENT VOLTAGE SIGNALS V_i MEASURED BY AN ASSEMBLY OF PELTIER ELEMENTS. ALL THESE CONTRIBUTIONS ARE SUMMED ACCORDING TO (1) TO GIVE THE SIGNAL VOLTAGE V_s.

To precisely evaluate the heat flux generated by a waste drum, calorimeter base line voltages $V_{\text{BL}\,1}$ and $V_{\text{BL}\,2}$ are measured without heat source in the calorimeter, before and after the measurement of the radioactive waste drum that generates heat. The average base line $\bar{V}_{\text{BL}} = \frac{V_{\text{BL}\,1}+V_{\text{BL}\,2}}{2}$ is subtracted to the signal measured with the heat generating waste drum V_s to obtain a net signal $\Delta V_{\text{net}} = V_s - \bar{V}_{\text{BL}}$.

Due to fluctuations of the regulation and of the room temperature, the signals vary over time. After subtraction of the periodic component related to room temperature variation, the uncertainty σ_j associated to a signal V_j is the RMS calculated over the N voltages $v_j(t_i)$ measured at time $\{t_i\}_{i=1,\dots,N}$ after voltage stabilization is achieved. In these conditions, the standard deviation $\sigma_{\Delta Vnet}$ of ΔV_{net} is $\sigma_{\Delta Vnet} = \sqrt{\left(\sigma_{V_s}^2 + \sigma_{V_{BL}}^2\right)}$.

The total heat generated by the sample W_{item} is related to the measured voltage ΔV_{net} through:

$$W_{\text{item}} = \frac{\Delta V_{\text{net}}}{S}\ , \tag{2}$$

with S (µV/mW) the sensitivity of the calorimeter. S is estimated using dedicated "Joule effect cells" with embedded resistors providing a known and controllable electrical power fully converted into a precisely known heat.

4.2.2 Calorimetry measurement

The room in which the calorimeter was placed, at CEA Cadarache TOTEM facility, was poorly insulated from the outside, leading to significant and fast temperature variations that were difficult to mitigate. In these conditions, it took about two weeks for the drum temperature to reach a satisfactory stability allowing meaningful measurement interpretation. A first baseline measurement was performed with the 526 kg concrete mock-up drum, but without the plutonium samples inside. Then, the measurement with the plutonium samples inserted inside dedicated instrumented holes was done. The baseline was then subtracted to obtain the net power due to plutonium.

Placing the sample in the centre of the drum leads to a calorimetric measurement of W_{meas}= (99.7 ± 16.4) mW with a coverage factor k = 2 for the expanded uncertainty confidence interval. This result is compatible with the expected $W_{Pu\ samples}$ = (110 ± 6) mW heat power of the plutonium samples for confidence intervals corresponding to two standard deviations. The measured net heat W is mainly produced by alpha emitters (and ^{241}Pu beta emitter) and is calculated as follow [1]:

$$W = m \cdot (568 \cdot f_{238Pu} + 1.93 \cdot f_{239Pu} + 7.08 \cdot f_{240Pu} + 3.41 \cdot f_{241Pu} + 0.16 \cdot f_{242Pu} + 114 \cdot f_{241Am}),$$

with m the total plutonium mass and f_X the mass fraction of isotope X in the measured sample. The coefficients associated to each isotope are their specific heat in W.g^{-1}.

Placing the sample in the centre of the drum leads to a calorimetric measurement of (99.7 ± 16.4) mW, which is compatible with the expected (110 ± 6) mW heat power of the plutonium samples for confidence intervals corresponding to one standard deviation. Note that for confidentiality reasons, neither the plutonium isotopic composition nor its mass can be reported. The experimental hall in which the calorimeter was implemented in CEA Cadarache TOTEM facility is poorly isolated from the outside, leading to significant temperature variations between night (14°C) and day (17°C), see Fig. 3 and 4: in these conditions, a stabilization period of more than 100 h is necessary before measuring the heat flow. A first measurement consisted in measuring the baseline of the heat flow between the concrete drum and a reference cell (differential calorimeter), without the plutonium samples (Fig. 3). Then, a measurement was done inserting the plutonium samples in the drum, inside dedicated instrumented tubes. The first measurement campaign shown in Figure 3 served to estimate a heat flow baseline with the empty calorimeter.

The baseline thus obtained is then subtracted to the heat flow measured with the concrete drum containing plutonium shown in Figure 4. Note also that due to large daily variations of the experimental hall temperature (typically 3 degrees between night and day), temperature stabilisation and subtraction of the reference cell baseline is more difficult than in an environment with smaller temperature fluctuations, for which calorimetric measurements should lead to more precise heat flow estimations.

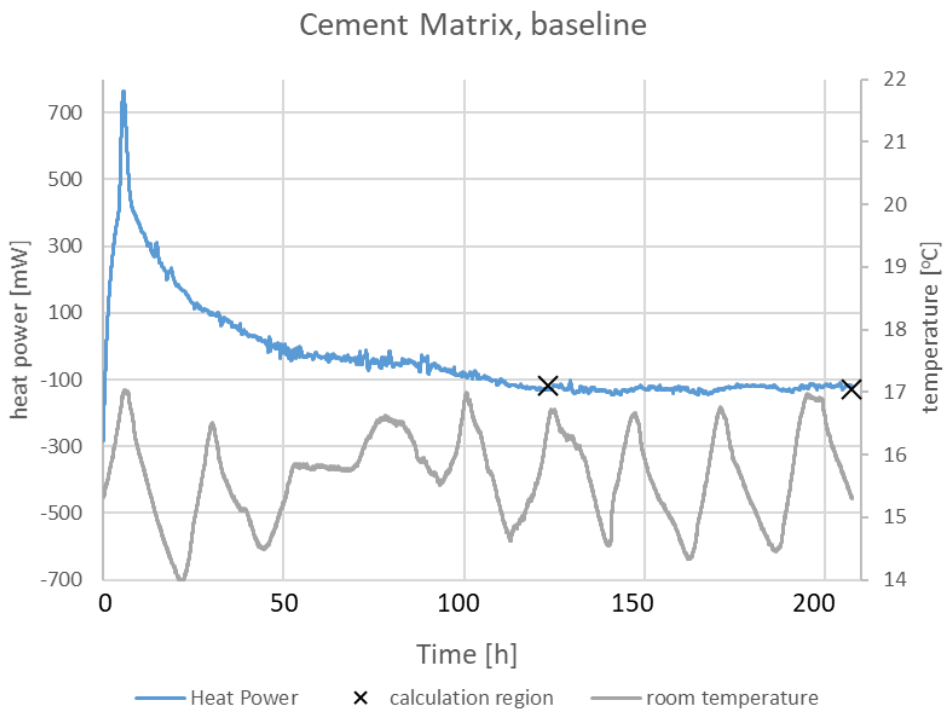

FIGURE 27. HEAT FLOW BASELINE MEASUREMENT AFTER PLACING THE CONCRETE DRUM (WITHOUT PLUTONIUM) IN THE CALORIMETER.

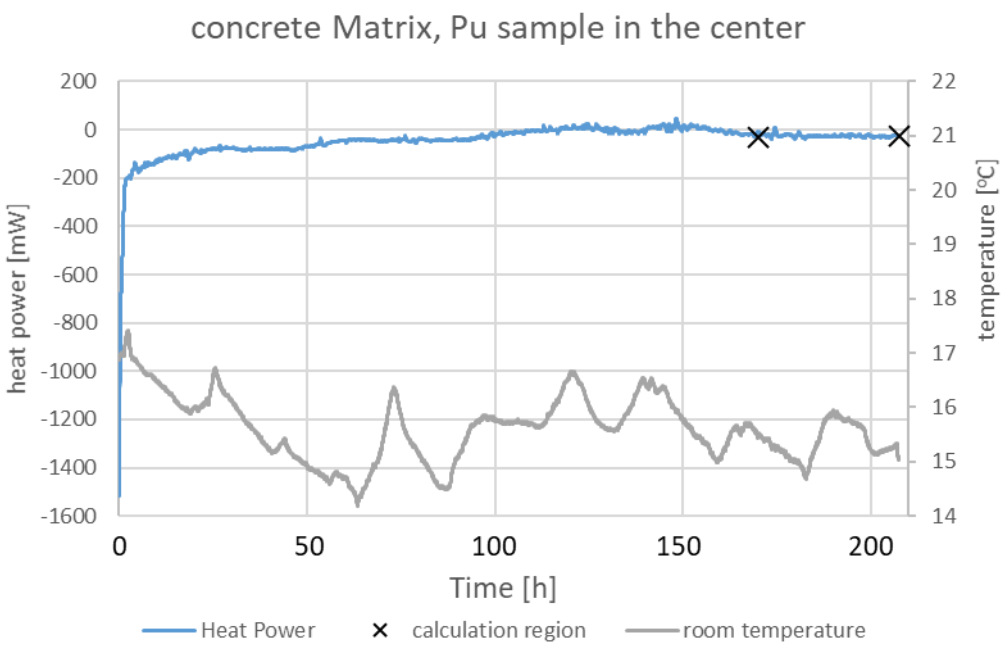

FIGURE 28. HEAT FLOW MEASUREMENT AFTER PLACING THE PLUTONIUM SAMPLES IN THE CENTRE OF THE CONCRETE DRUM.

Given the project calendar and needed stabilization times, measurements at other positions than the central position were not possible. However, calorimetric measurements are in principle not sensitive to the heat source position [23, 25]. Therefore, in the following, the same heat production will be assumed for all the positions of the plutonium source.

4.2.3 Passive neutron Coincidence Counting

The concrete drum has also been measured with the relocatable passive neutron coincidence counting (PNCC) system shown in Figure 5. This system aims at measuring ^{240}Pu equivalent mass by counting the rate of passive neutron coincidences (neutron pairs counted with a JSR-14 shift register analyser from Mirion Technologies) in 200 L drums with ^{3}He counters surrounded by polyethylene thermalizing blocs. This relocatable system is used, for instance, to characterize legacy waste drums in their storage facility at CEA Cadarache. In the frame of CHANCE project, it was used in TOTEM facility of the Nuclear Measurement Laboratory, to perform the PNCC measurements with the concrete drum.

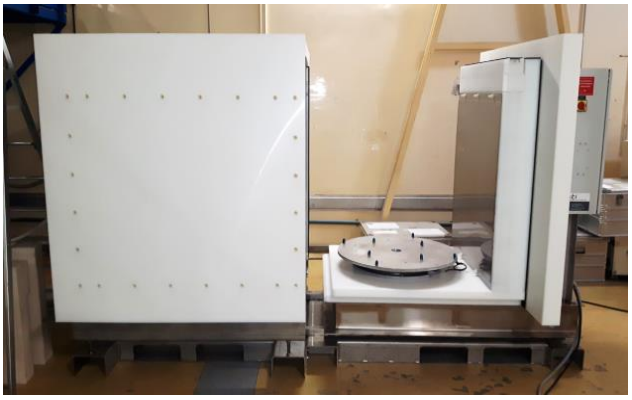

FIGURE 29. RELOCATABLE PNCC SYSTEM DEVELOPED BY THE NUCLEAR MEASUREMENT LABORATORY AT CEA CADARACHE.

The "equivalent ^{240}Pu mass" $m_{^{240}Pu\ eq}$ (see definition below) is related to the measured neutron coincidence count rate R_n via a calibration coefficient CC (in $s^{-1}.g_{240Pu}^{-1}$) through the relation:

$$m_{^{240}Pu\ eq} = \frac{R_n}{CC}$$

$m_{^{240}Pu\ eq}$ is related to the total plutonium mass m_{Pu} and to its isotopic composition thought the following relation [1]:

$$m_{^{240}Pu\ eq} = m_{Pu} \cdot (2.52 \cdot f_{238Pu} + 1 \cdot f_{240Pu} + 1.68 \cdot f_{242Pu})$$

The calibration coefficient CC (in $s^{-1}.g_{^{240}Pu}^{-1}$ units) is assessed with a spontaneous fission ^{252}Cf source placed at different positions in the drum instrumentation holes, while the drum is in continuous rotation during acquisition, using the following relation to convert the ^{252}Cf signal into a ^{240}Pu CC:

$$CC\,(s^{-1}.\boldsymbol{g}^{-1}_{240_{Pu}}) = \frac{R_{252_{Cf}}}{\frac{En_{252_{Cf}}}{\overline{\upsilon_{252_{Cf}}}}\cdot\overline{\left(\frac{\upsilon(\upsilon-1)}{2}\right)_{252_{Cf}}}} \cdot \frac{En^{s}_{240_{Pu}}}{\overline{\upsilon_{240_{Pu}}}} \cdot \overline{\left(\frac{\upsilon(\upsilon-1)}{2}\right)_{240_{Pu}}}$$

With $\boldsymbol{R}_{252_{Cf}}$ the coincidence rate (neutron pairs) measured with the ^{252}Cf source (in s^{-1}), $\boldsymbol{En}_{252_{Cf}}$ the neutron emission rate of ^{252}Cf by spontaneous fission (in s^{-1}), $En^{s}_{240_{Pu}}$ the specific neutron emission rate of ^{240}Pu by spontaneous fission (in $s^{-1}.g^{-1}_{240_{Pu}}$), $\overline{\upsilon_X}$ the average number of neutrons emitted per spontaneous fission of X, $\overline{\left(\frac{\upsilon(\upsilon-1)}{2}\right)_X}$ the average number of neutron pair combinations (as counted by the JSR-14 shift register [1]) emitted per spontaneous fission of X. The values of the parameters involved in the calculation of CC are given in Table 1.

TABLE 26. SPECIFIC NEUTRON EMISSION RATE AND AVERAGE NUMBER OF NEUTRONS EMITTED PER SPONTANEOUS FISSIONS FOR ^{252}CF AND ^{240}PU.

$En_{252_{Cf}}$	45184 s^{-1}
$En_{240_{Pu}}$	1020 s^{-1}. g_{240Pu}^{-1}
$\overline{\upsilon_{252_{Cf}}}$	3.757
$\overline{\upsilon_{240_{Pu}}}$	2.156
$\overline{\left(\frac{\upsilon(\upsilon-1)}{2}\right)_{252_{Cf}}}$	5.981
$\overline{\left(\frac{\upsilon(\upsilon-1)}{2}\right)_{240_{Pu}}}$	1.913

The large density and hydrogen content of the concrete matrix induces large neutron attenuation, which makes the calibration coefficient very sensitive to the SF source position. For instance, the measured CC is 18 times larger in the outskirt of the drum than in the middle, making PNCC very imprecise with such matrices when the plutonium position is unknown. Using the available measurements of ^{252}Cf in different heights and radii inside the drum, the experimental calibration coefficient is fitted with the following function:

$$CC(r,h)_0 = \sum_{i=0}^{2} a_i \cdot h^i + \left(\sum_{i=0}^{2} b_i \cdot h^i\right) \cdot e^{\left(\sum_{i=0}^{2} c_i \cdot h^i\right)\cdot r}$$

with r and h the radial and axial (height) positions of the source inside the drum, respectively. Such an analytical form allows taking into account the expected exponential neutron attenuation through the drum radius.

Then three PNCC measurements have been done with the plutonium samples at the same axial position $h = \frac{1}{2}$ times the height of the drum (mid-height), but at three different radial positions r=0, 0.43 and 1 times the radius of the drum. $CC(r,h)_0$ and the measured CC are presented in Figure 6.

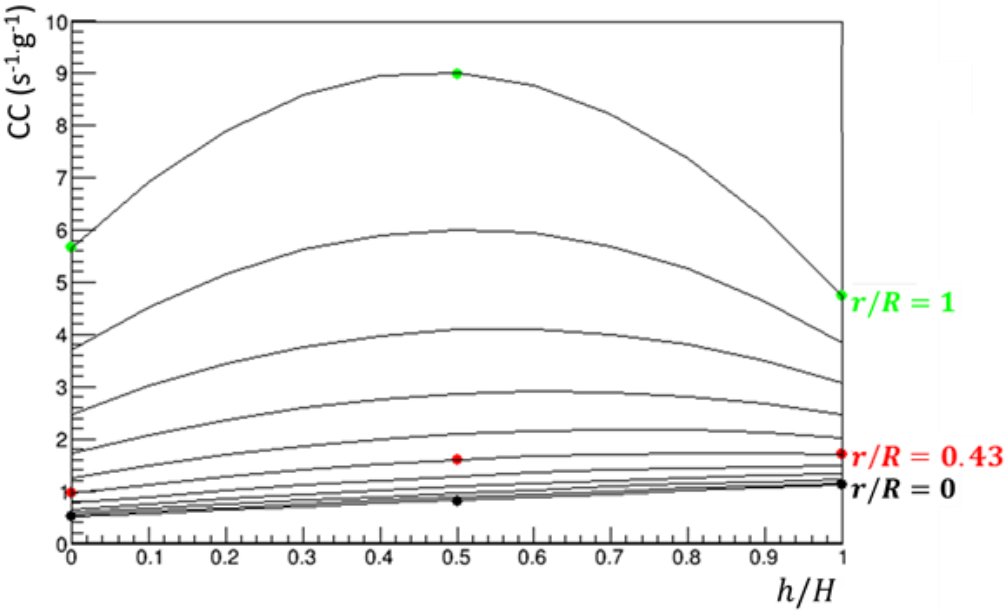

FIGURE 30. PNCC CALIBRATION COEFFICIENT VERSUS PLUTONIUM HEIGHT POSITIN FOR DIFFERENT RADIAL POSITIONS (POINTS) AND $CC(r,h)_0$ FIT AND EXTRAPOLATIONS (LINE).

4.2.4 Gamma ray spectrometry

The gamma-ray spectra of the plutonium samples have been measured with a 9 % relative efficiency Broad Energy Germanium Detector (Mirion-Canberra BEGe2020 described in [31]) surrounded by lead shielding and aligned with the drum centre and the source position. A thin tin plate is placed in front of this HPGe (high-purity germanium) detector entrance surface to attenuate low energy γ- and X-rays. The samples are placed inside the instrumentation holes at the three same positions as for PNCC, but without drum rotation (no rotating platform being available at the period of measurements), as shown in Figure 7. The measurement in peripheral position (r=1) has been performed with two setups, first (measurement #0) with the four plutonium platelets closely stacked at the same height and forming a thick sample, in order to maximize gamma self-absorption, then (measurement #1) with the four platelets superimposed vertically to minimize self-absorption. For measurements #2 and #3, the plutonium samples stacked vertically were respectively placed in the centre (r=0) and in the intermediate radius of the drum (r=0.43), plutonium being placed in the line defined by the drum centre and the HPGe axis. The four plutonium samples are considered as a single plutonium lump with different self-absorption coefficients, depending on whether they are superimposed vertically or closely stacked at the same height.

The Genie2000 spectroscopy software [32] was used to determine the presence of the following gamma rays: 766 keV (^{238}Pu), 129 keV, 203 keV, 345 keV, 375 keV, 414 keV and 451 keV (^{239}Pu), 160 keV and 642 keV (^{240}Pu), 149 keV (^{241}Pu), 59 keV, 125 keV and 722 keV (^{241}Am).

FIGURE 31. GAMMA SPECTROSCOPIC MEASUREMENT OF THE CONCRETE MOCK-UP DRUM WITH THE HPGE DETECTOR (LEFT) AND TOP VIEW OF THE CONCRETE TEST DRUM SHOWING THE HOLES OF THE TUBES TO INSERT PU SAMPLES (RIGHT).

4.3 Bayesian formalism

The calorimeter measures a thermal power W_{meas} with uncertainty σ_W and PNCC measures a neutron coincidence rate R_{meas} with uncertainty σ_R. For an isotope i emitting a gamma ray e having an energy $E_{i,e}$, Genie2000 provides an estimation of the number of noise counts $B_{i,e}$ associated to the Compton continuous background below the peak, and a net signal counts $N_{i,e}$ with uncertainty $\sigma_{i,e}$ when the estimated peak area is above a decision threshold equal to $1.645\sqrt{2 \cdot B_{i,e}}$ [14], corresponding to a 90 % confidence interval.

The unknown variables related to the plutonium samples are the total plutonium mass m, the isotopic composition $\{f_i\}_{i=0,\dots,5}$, with i=0,1,2,3,4,5 for ^{238}Pu, ^{239}Pu, ^{240}Pu, ^{241}Pu, ^{242}Pu, ^{241}Am, respectively, and the plutonium position in a cylindrical frame (r, h, θ). The plutonium position determines the PNCC calibration coefficient $CC(r,h)_0$ with the drum in rotation (no angle dependence), the concrete thickness $k(r,h,\theta)$ crossed by photons towards the HPGe detector, and the distance $d(r,h,\theta)$ between the plutonium samples and the HPGe detector. In the model, we also introduce the plutonium thickness d_{Pu} as an unknown variable to characterize plutonium self-absorption. Plutonium is in a metallic form but with some uncertainties on its geometry inside the platelets, so we keep some flexibility regarding its mass attenuation coefficient (μ/ρ in cm²/g) and density, by introducing an additional variable δ_{Pu} associated to the possible deviation on the product of the Pu mass attenuation by its density. Similarly, to take into account the uncertainty on concrete density and composition, we introduce a variable deviation δ_c on the product of concrete mass attenuation coefficient by its density. δ_{Pu} and δ_c are in the range [0.9;1.1] and follow a Gaussian distribution with mean 1 and standard deviation 0.05.

Attenuation due to the drum iron cast and the HPGe thin plate of tin is known, but the possibility of having an additional attenuation caused by the presence of a zirconium sheet (around the Pu platelets) is also taken into account with a variable d_{Zr} representing the zirconium thickness.

A Bayesian formalism allows linking the measured quantities with the set of unknown variables $\boldsymbol{X} = \{m, \{f_0, f_1, f_2, f_3, f_5\}, r, h, \theta, d_{Pu}, d_{Zr}, \delta_{Pu}, \delta_c\}$ using prior information through the relation:

$$P(\boldsymbol{X}|W_{meas}, R_{meas}, \{N_{i,e}, B_{i,e}, \sigma_{i,e}\}_{\substack{i=0,\dots,5 \\ e=0,\dots,n_i}})$$

$$\alpha$$

$$Gauss(\widehat{W} - W_{meas}, \sigma_W) \cdot Gauss(\hat{R} - R_{meas}, \sigma_R) \cdot \prod_{i=0}^{5} \prod_{e=0}^{n_i} P_\gamma(\widehat{N_{i,e}}, N_{i,e}, B_{i,e}, \sigma_{i,e}|\boldsymbol{X}) \cdot P_0(\boldsymbol{X})$$

with $Gauss(x, y)$ the Gaussian distribution of the variable x with mean 0 and standard deviation y, n_i the number of selected gamma rays for isotope i and $\widehat{W}, \hat{R}, \widehat{N_{i,e}}$ the expected calorimeter heat flux, neutron coincidence rate, and gamma-ray net area, respectively:

$$\widehat{W} = m \cdot (568 \cdot f_0 + 1.93 \cdot f_1 + 7.08 \cdot f_2 + 3.41 \cdot f_3 + 0.16 \cdot f_4 + 114 \cdot f_5)$$

$$\hat{R} = m_{^{240}Pu} \cdot CC(r, h)_0$$

$$\widehat{N_{i,e}} = m_{Pu} \cdot f_i \cdot T \cdot A_i^S \cdot BR(E_{i,e}) \cdot att_0(E_{i,e}) \cdot e^{-\left(\frac{\mu}{\rho}\right)_c (E_{i,e}) \cdot \rho_c \cdot \delta_c \cdot k(r,h,\theta)} \cdot e^{-\left(\frac{\mu}{\rho}\right)_{Zr} (E_{i,e}) \cdot \rho_{Zr} \cdot d_{Zr}} \cdot \frac{1 - e^{-\left(\frac{\mu}{\rho}\right)_{Pu} (E_{i,e}) \cdot \rho_{Pu} \cdot \delta_{Pu} \cdot d_{Pu}}}{\left(\frac{\mu}{\rho}\right)_{Pu} (E_{i,e}) \cdot \rho_{Pu} \cdot \delta_{Pu} \cdot d_{Pu}} \cdot \frac{\varepsilon(E_{i,e})}{4\pi \cdot d(r,h,\theta)^2}$$

with T the gamma ray measurement time, A_i^S the specific activity of isotope i, $BR(E_{i,e})$ the branching ratio for isotope i to emit a photon with energy $E_{i,e}$, $att_0(E_{i,e})$ the attenuation caused by the drum iron cast and the tin thin plate, $\left(\frac{\mu}{\rho}\right)_M (E)$ the mass attenuation coefficient of material M (M=c,Zr or Pu, "c" corresponding to concrete) at energy E, ρ_M the density of material M and ε(E) the HPGe intrinsic detection efficiency at energy E (number of counts in the net area per photon entering in the germanium crystal).

If Genie2000 is able to provide a number of counts N_(i,e) related to the gamma ray i of isotope e, the posterior density function related to gamma-ray spectrometry is:

$$P_\gamma(\widehat{N_{i,e}}, N_{i,e}, B_e, \sigma_{i,e} | \boldsymbol{X}) = Gauss(\widehat{N_{i,e}} - N_{i,e}, \sigma_{i,e})$$

with $\sigma_{i,e}$ the global uncertainty on the net peak area that takes into account the statistical uncertainty $\sigma_{i,e,0}$ estimated by Genie2000 and δ_{HPGe} the relative uncertainty on the HPGe intrinsic detection efficiency (typically 5 %):

$$\sigma_{i,e} = \sqrt{{\sigma_{i,e,0}}^2 + {\delta_{HPGe}}^2 \cdot {N_{i,e}}^2}$$

Note that for the 59 keV gamma ray of 241Am, δ_{HPGe}= 50 %, to take into account the extremely high gamma-ray attenuation at such a low energy and the associated uncertainty.

If the net area is below the decision threshold, the posterior density function is:

$$P_\gamma(\widehat{N_{i,e}}, N_{i,e}, B_{i,e}, \sigma_{i,e} | \boldsymbol{X}) = PoissonCDF(\widehat{N_{i,e}}, 1.645\sqrt{2 \cdot B_{i,e}}),$$

PoissonCDF being the complement of the Poisson cumulative distribution function.

4.4 NDA characterization methods in conjunction with calorimetry

The posterior estimation $\widehat{m}$ of the plutonium mass m is obtained by integrating: $P(\boldsymbol{X}|W_{meas}, R_{meas}, \{N_{i,e}, B_{i,e}, \sigma_{i,e}\}_{\substack{i=0,\dots,5 \\ e=0,\dots,N_i}})$ over $\{\{f_0, f_1, f_2, f_3, f_5\}, r, h, \theta, d_{Pu}, d_{Zr}, \delta_{Pu}, \delta_{Zr}\}$.

The integration is done by means of a Markov Chain Monte Carlo (MCMC) sampling using the Metropolis-Hasting algorithm implemented in the ROOTStat statistical tools based on the CERN's ROOTFit package [33].

To investigate the impact of PNCC and calorimetry on plutonium mass estimation, for each of the four gamma-ray measurements, MCMC sampling is performed with or without the information brought by PNCC and calorimetry. For each of these configurations, 5 MCMC sampling chains have been generated with about $8 \cdot 10^8$ iterations starting

from a randomly chosen position. The posterior probability distributions are shown in Figure 8 to Figure 1. The mass obtained by MCMC sampling $\hat{m}$ is normalized to the true plutonium mass m.

Although starting from different points, MCMC chains associated to a given configuration lead to the same posterior mass distributions, which is a good indication that the chain is long enough to guaranty convergence. Consequently, the mean plutonium mass and RMS of these distributions are consistent, as shown in Figure 12.

The traditional coupling of gamma ray spectrometry with PNCC or with calorimetry greatly improves plutonium mass estimation compared to the use of only gamma spectrometry, in particular when plutonium is located in the drum centre where gamma ray attenuation is the strongest. However, for measurements 0, 1, 2 and 3, the uncertainty of PNCC coupled with gamma ray spectrometry is respectively a factor 2.0, 2.4, 4.0 and 3.3 times higher than the uncertainty of calorimetry coupled with gamma ray spectrometry. The greater precision of the calorimetric measurement is due to calorimetry insensitivity to the position of plutonium in the drum. In addition, the plutonium contains mainly ^{239}Pu. PNCC is not sensitive to 239Pu, which is not the case for calorimetry.

Given the better uncertainty obtain with calorimetry, the uncertainty obtained by coupling calorimetry and PNCC is nearly equal to the calorimetric measurement uncertainty.

The added value of calorimetric measurement for plutonium measurement in 200 L radioactive waste drums should be further investigated, for example with setups having several plutonium samples placed simultaneously at different positions in the drum or taking into account the possibility of homogeneously distributed plutonium, either in the whole drum or in some drum sections. If more plutonium sources are involved, it will probably be necessary to perform several gamma-ray spectrometry measurements at different positions, or with the drum in rotation.

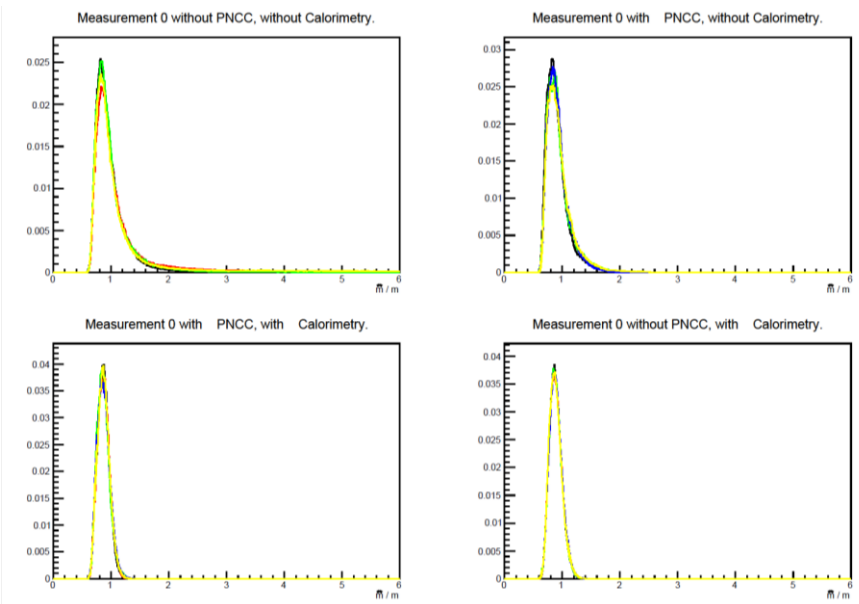

FIGURE 32. POSTERIOR PLUTONIUM MASS DISTRIBUTIONS OBTAINED WITH 5 MCMC CHAINS FOR MEASUREMENT #0 (4 PLUTONIUM PLATELETS IN THE PERIPHERY, STUCK TOGETHER AT THE SAME HEIGHT TO MAXIMIZE GAMMA SELF-ABSORPTION), WHEN PNCC AND/OR CALORIMETRY MEASUREMENTS ARE TAKEN INTO ACCOUNT, FOR MCMC SAMPLING CHAINS STARTING FROM DIFFERENT POSITIONS IN THE PARAMETER SPACE. THE MASS IS REPRESENTED AS A RATIO BETWEEN THE OBTAINED MCMC PLUTONIUM MASS AND THE TRUE PLUTONIUM MASS. EACH MASS DISTRIBUTION OBTAINED WITH ONE MCMC CHAIN IS REPRESENTED WITH A DIFFERENT COLOR.

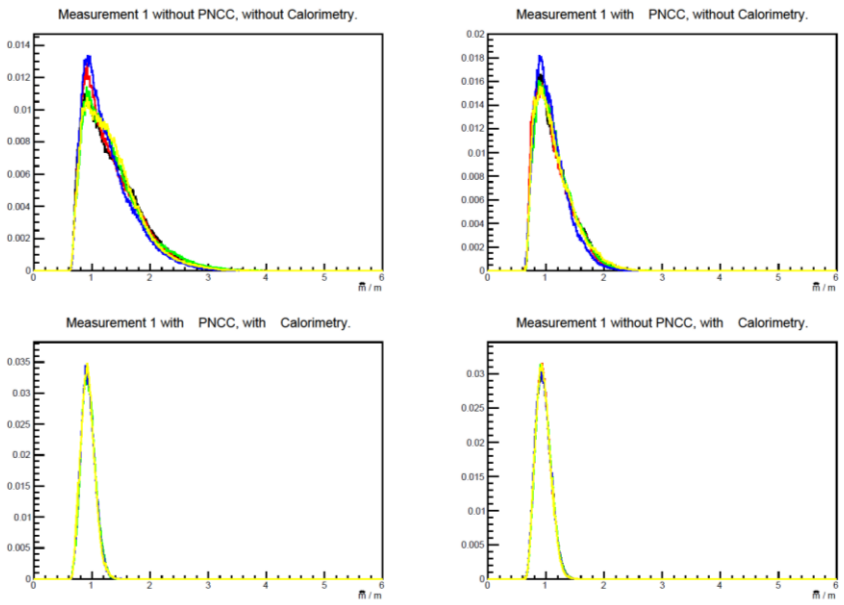

FIGURE 33. POSTERIOR PLUTONIUM MASS DISTRIBUTIONS OBTAINED WITH 5 MCMC CHAINS FOR MEASUREMENT #1 (4 PLUTONIUM PLATELETS IN THE PERIPHERY, STACKED VERTICALLY), WHEN PNCC AND/OR CALORIMETRY MEASUREMENTS ARE TAKEN INTO ACCOUNT, FOR MCMC SAMPLING CHAINS STARTING FROM DIFFERENT POSITIONS IN THE PARAMETER SPACE. THE MASS IS REPRESENTED AS A RATIO BETWEEN THE OBTAINED MCMC PLUTONIUM MASS AND THE TRUE PLUTONIUM MASS. EACH MASS DISTRIBUTION OBTAINED WITH ONE MCMC CHAIN IS REPRESENTED WITH A DIFFERENT COLOR.

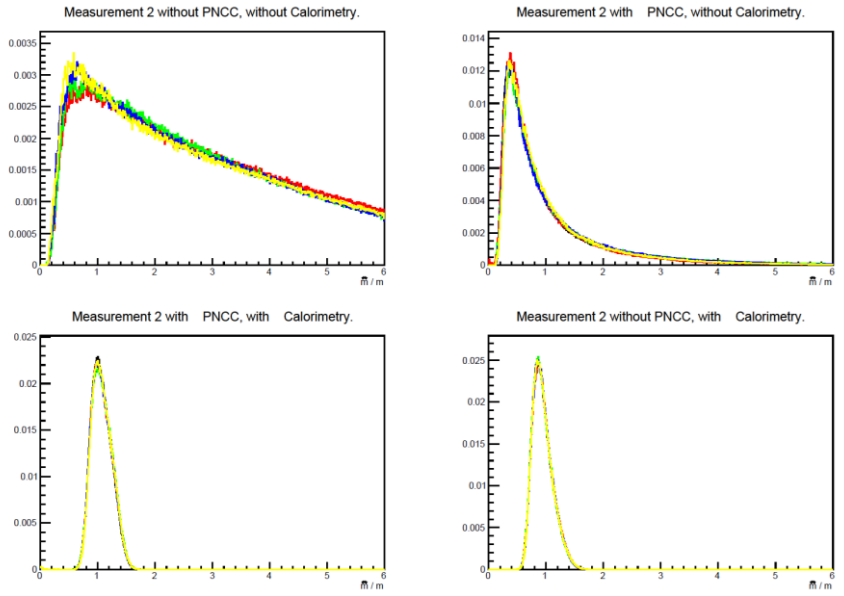

FIGURE 34. POSTERIOR PLUTONIUM MASS DISTRIBUTIONS OBTAINED WITH 5 MCMC CHAINS FOR MEASUREMENT #2 (4 PLUTONIUM PLATELETS IN THE DRUM CENTRE, STACKED VERTICALLY), WHEN PNCC AND/OR CALORIMETRY MEASUREMENTS ARE TAKEN INTO ACCOUNT, FOR MCMC SAMPLING CHAINS STARTING FROM DIFFERENT POSITIONS IN THE PARAMETER SPACE. THE MASS IS REPRESENTED AS A RATIO BETWEEN THE OBTAINED MCMC PLUTONIUM MASS AND THE TRUE PLUTONIUM MASS. EACH MASS DISTRIBUTION OBTAINED WITH ONE MCMC CHAIN IS REPRESENTED WITH A DIFFERENT COLOR.

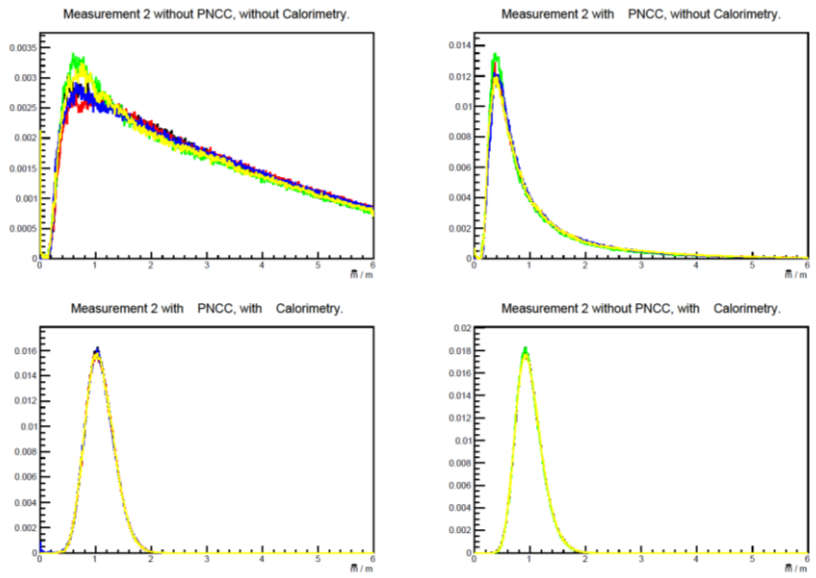

FIGURE 35. POSTERIOR PLUTONIUM MASS DISTRIBUTIONS OBTAINED WITH 5 MCMC CHAINS FOR MEASUREMENT #3 (4 PLUTONIUM PLATELETS PLACED AT 0.43·R, STACKED VERTICALLY), WHEN PNCC AND/OR CALORIMETRY MEASUREMENTS ARE TAKEN INTO ACCOUNT, FOR MCMC SAMPLING CHAINS STARTING FROM DIFFERENT POSITIONS IN THE PARAMETER SPACE. THE MASS IS REPRESENTED AS A RATIO BETWEEN THE OBTAINED MCMC PLUTONIUM MASS AND THE TRUE PLUTONIUM MASS. EACH MASS DISTRIBUTION OBTAINED WITH ONE MCMC CHAIN IS REPRESENTED WITH A DIFFERENT COLOR.

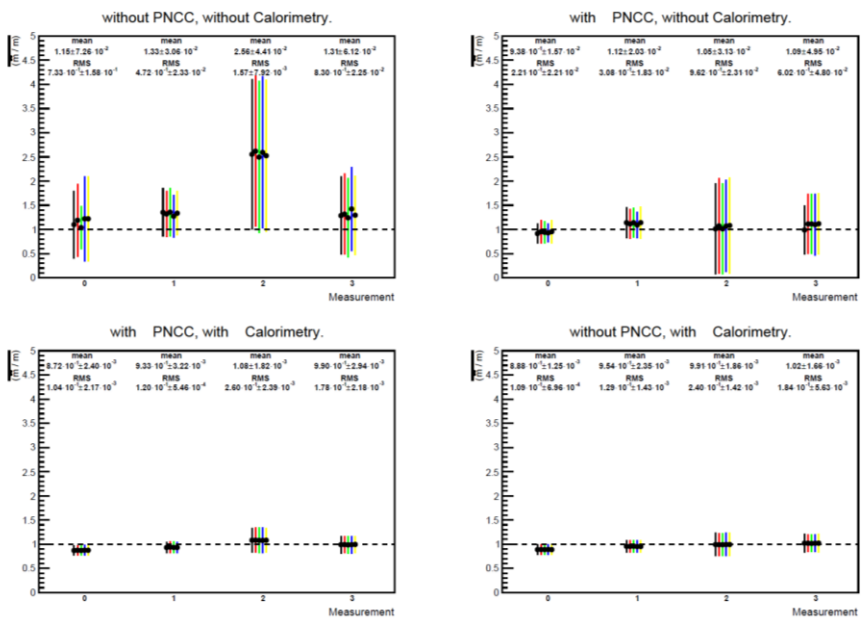

FIGURE 36. MEAN PLUTONIUM MASSES $\overline{(\widehat{m}/m)}$ FOR THE DIFFERENT MEASUREMENTS #0 TO #3, USING OR NOT PNCC AND CALORIMETRY. EACH SET OF 5 POINTS CORRESPONDS TO THE SET OF 5 SPECTRA (OBTAINED WITH 5 MCMC CHAINS) SHOWN IN FIG.8 TO FIG. 11, WITH ERROR BARS CORRESPONDING TO THE SPECTRA RMS. EACH ERROR BAR HAS THE SAME COLOR AS THE SPECTRUM THAT SERVED TO CALCULATE THE MEAN AND THE RMS. FOR EXAMPLE, FOR MEASUREMENT #3 WITHOUT PNCC AND CALORIMETRY, THE POINT WITH A BLUE ERROR BAR CORRESPONDS

4.5 Conclusions with respect to the CEA exercise

The measurements show interesting complementarities. PNCC is sensitive to plutonium isotopes with an even atomic number, mainly ^{240}Pu for our samples. Calorimetry is sensitive to intense alpha emitters, mainly ^{239}Pu, ^{240}Pu and ^{241}Am in our case. Gamma-ray spectrometry is sensitive to plutonium isotopes and ^{241}Am, and it is particularly interesting for ^{239}Pu that emits several gamma rays on the 100-500 keV range, which brings information on gamma attenuation in the cement matrix. In addition, Calorimetry is not sensitive to the plutonium sample position inside this matrix, contrary to PNCC and gamma-ray spectrometry, these last showing important uncertainties due to matrix attenuation effects.

Figure 13 allows comparing the uncertainties obtain during the Cadarache measurement campaign by switching ON or OFF calorimetry and PNCC. The experimental investigations with plutonium samples in the 200 L concrete drum show that calorimetry allows significantly reducing the uncertainty on the Pu activity compared to the use of gamma spectroscopy and/or PNCC. Such a result is due to the isotopic composition of the plutonium samples and would need further investigations with plutonium having different isotopic composition.

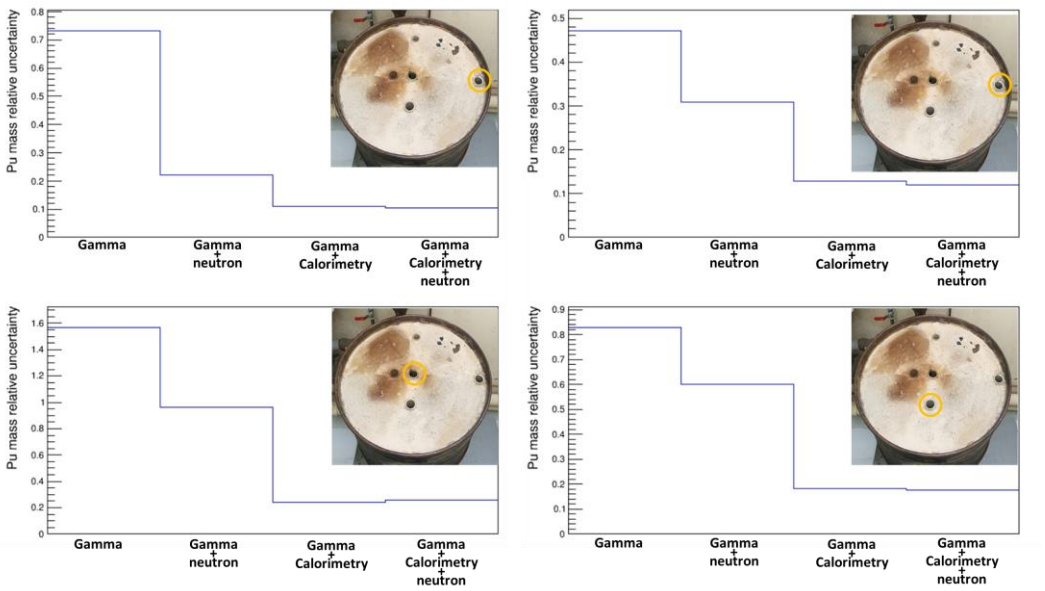

FIGURE 37. PLUTONIUM MASS UNCERTAINTY AS FUNCTION OF MEASUREMENTS COMBINATIONS.

5 Probabilistic modelling for the SCK CEN experiments

5.1 Introduction

As detailed in [1], at SCK CEN, the experimental plan was focused around the six setups presented in Table 27. Each of the setups was subjected to open geometry gamma spectrometry (ISOCS) and FRAM analysis of the spectrum, Q2 gamma spectrometry (with 3 fixed detectors at different heights), passive neutron coincidence counting (PNCC), and a calorimeter (CAL) measurement. Setup 1 (real drum) was also measured by segmented gamma scanning (3AX) but not with Q2. Additionally, a series of extra joule effect pulses (500, 375, 250, 200, 150, and 50 mW) was also measured with the calorimeter, for enabling more reliable calibration of the calorimeter sensitivity coefficients, as only a single pulse (500 mW) had been measured before at KEP. Based on all these results, the following three sets of exercises were performed, to quantify uncertainties, and investigate the information provided by the different types of techniques:

1. Calibration of the calorimeter sensitivity coefficients (Section 5.2),
2. Different exercises based on the mock-up drum and reference source measurements (Setups 2-6; Section 5.3), were
    - A first exercise is performed, accounting for all prior knowledge, to check all measurements and MNCP-calculated efficiencies for consistency. Here the only unknown quantities are thus the activities, while count statistics are still in play as well. All other variables are fixed to prescribed values. We refer to this setup as ”FULLY KNOWN”.
    - A second exercise is performed, accounting for a realistic amount of prior knowledge, to assess what the uncertainties could look like in practice. Here all considered uncertainties are accounted for but some assumptions are favoured a priori. The inference is then allowed to move away from these assumptions if needed to fit the measurement data. We refer to this setup as “REALISTIC”.
    - A third and final exercise, where we assume little to no prior knowledge is available, to assess what the data can tell us in such a case. Overall, here only the fit to the measurement data is guiding the inference, which should be representative for the characterization of a “mystery drum”, or legacy waste that comes with very little documentation. We refer to this setup as the ”MYSTERY DRUM” case.
3. The real unconditioned waste drum exercise (Setup 1; Section 5.4).

For the first, we obviously made use of the joule effect calibration measurements, but the inclusion of the mock-up drum measurements with reference sources (Setups 2-6) was investigated as well, resulting in a total of 12 calibration data points.

Similarly, as in [26] we used the open-source greta package [34] to perform the HMC-based MCMC sampling. The greta package is an R [35] interface to some of the MCMC sampling algorithms implemented in the Tensorflow-probability package [36] which itself relies on the Tensorflow (TF) machine learning platform [37]. The most useful MCMC sampler available through greta and used herein is HMC [38, 39]. This TFP-based HMC implementation can evolve several Markov chains in parallel on both CPUs and GPUs, with the different chains exchanging information during warmup to speedup convergence.

TABLE 27. OVERVIEW OF THE TARGETED SETUPS IN THE SCK CEN MEASUREMENT CAMPAIGN.

Setup nr.	Description
Setup 1	Real unconditioned waste drum
Setup 2	7 pins (21 sources) inside mock-up 206 (mortar & XPS)
Setup 3	1 pin (single source) in the centre of mock-up 206
Setup 4	1 pin (single source) at the border of mock-up 206
Setup 5	7 pins (21 sources) inside mock-up 201 (ethafoam)
Setup 6	7 pins (21 sources) inside mock-up 205 (ethafoam, pvc, steel)

5.2 The calorimeter calibration and corresponding uncertainties

5.2.1 Methodology

In [1] and Section 4 above, the results of a calibration exercise at KEP were used for the interpretation of the calorimeter measurements performed at CEA. Another calibration exercise at KEP with a 500 mW pulse was used during the SCK CEN measurement campaign for preliminary interpretations, while this was updated for [1] with the additional joule effect pulses performed at SCK CEN and a standard linear regression approach per block, and for the total signal, where

$$V_l = P \times S_l \tag{5.1}$$

$$V_r = P \times S_r \tag{5.2}$$

$$V_c = P \times S_c \tag{5.3}$$

$$V_t = P \times S_t \tag{5.4}$$

and

$$S_t = S_l + S_r + S_c$$

$$V_t = V_l + V_r + V_c$$

with V the net voltage, P the thermal power, S the sensitivity coefficient and subscripts l, r, c and t referring to the left block, right block, central block, and total (summed) signal respectively. The linear regression model fits, and available data points, including those of the mock-up drum experiments, are displayed in Figure 38.

From Figure 38, it is clear that not all data point uncertainty intervals are consistent with the obtained sensitivity coefficients and their confidence intervals, and especially for some of the mock-up drum measurements, where the exact same reference sources were used, but they were placed in a different location, there is a systematic shift in the net voltage. This does suggest that we are not trying to find a unique (set of) sensitivity coefficient(s) here, but that these may depend on the properties of the actual object measured, or at least on the location of heat production within the object. When realizing this, it seems to make sense to let the sensitivity coefficients vary on a measurement by measurement basis, which is why we turn here to a hierarchical, or multi-level, Bayesian regression approach. To allow for comparison with the classic approach, we perform the Bayesian regression as well for the case where we consider the total signal (sum), corresponding to equation (5.4), but we additionally include the baseline and gross voltages B and G, and use here index i to differentiate between different measurements:

$$\begin{bmatrix} G_{l,i} \\ G_{r,i} \\ G_{c,i} \end{bmatrix} = P_i \times \frac{S_t}{3} + \begin{bmatrix} B_{l,i} \\ B_{r,i} \\ B_{c,i} \end{bmatrix} \tag{5.5}$$

Additionally, we consider the equivalent of equations (5.1), (5.2) and (5.3), where we look at the combination of the three blocks with each their own coefficient:

$$\begin{bmatrix} G_{l,i} \\ G_{r,i} \\ G_{c,i} \end{bmatrix} = P_i \times \begin{bmatrix} S_l \\ S_r \\ S_c \end{bmatrix} + \begin{bmatrix} B_{l,i} \\ B_{r,i} \\ B_{c,i} \end{bmatrix} \tag{5.6}$$

And finally, we consider the hierarchical case, where every measurement i has its own sensitivity coefficient:

$$\begin{bmatrix} G_{l,i} \\ G_{r,i} \\ G_{c,i} \end{bmatrix} = P_i \times \begin{bmatrix} S_{l,i} \\ S_{r,i} \\ S_{c,i} \end{bmatrix} + \begin{bmatrix} B_{l,i} \\ B_{r,i} \\ B_{c,i} \end{bmatrix} \tag{5.7}$$

Obviously, we end up here with a large number of parameters to fit, while we do only have a limited dataset, but the power of the Bayesian approach here lies in the regularization properties obtained through an appropriate definition of the prior distributions, or hyperpriors in case of the hierarchical approach for the sensitivity coefficients.

Before specifying the priors, however, let us first mention here that we consider all $G_{l,i}$, $G_{r,i}$, and $G_{c,i}$ quantities to be the mean of a Gaussian likelihood for our observed gross voltages (mean of the noise-corrected gross measurement signal), where the standard deviation equals the standard error on the mean signal from the batch means estimator, as detailed in [1].

Then, we need a prior distribution for all inferred parameters. This includes for the powers P_i only those of the ESARDA reference sources, as we assume the joule effect pulse uncertainty to be negligible. For the ESARDA sources, a very informative Gaussian prior with a standard deviation of 2 mW, to allow for a minimum amount of uncertainty. The baseline voltage is also inferred here, and we basically use the same approach as for the gross voltage likelihood: a Gaussian prior, where the mean equals the mean of the noise-corrected baseline measurement signal, and the standard deviation comes from the batch means estimator. Finally, for the sensitivity coefficients, the not-so-informative priors depend on the approach:

- For Equations (5.5) and (5.6), the priors for $S_t/3$, S_l, S_r or S_c are all Gaussian with a mean of 50 and standard deviation of 20 µV/mW,
- For Equation (5.7), the hyperpriors on the three means for all 12x3 Gaussian priors for the three block sensitivities are the same as that above (Gaussian, mean = 50, sd = 20), while those for the three standard deviations are exponential distributions with rate parameter 3.

The latter hierarchical approach with hyperpriors makes sure that the minimum variation possible in sensitivity coefficients of different measurements is allowed, while still making sure that all observed data points are consistent with the model.

Do note that the noise correction discussed in [1] was used as such here because of time limitations and is not included in the probabilistic model at this point. For future analyses, it is recommended to include the full data-generating process in the model, which means starting from the full raw signal time series from the reference and measurement Peltier elements, instead of the batch means estimator already applied to the combination of those two.

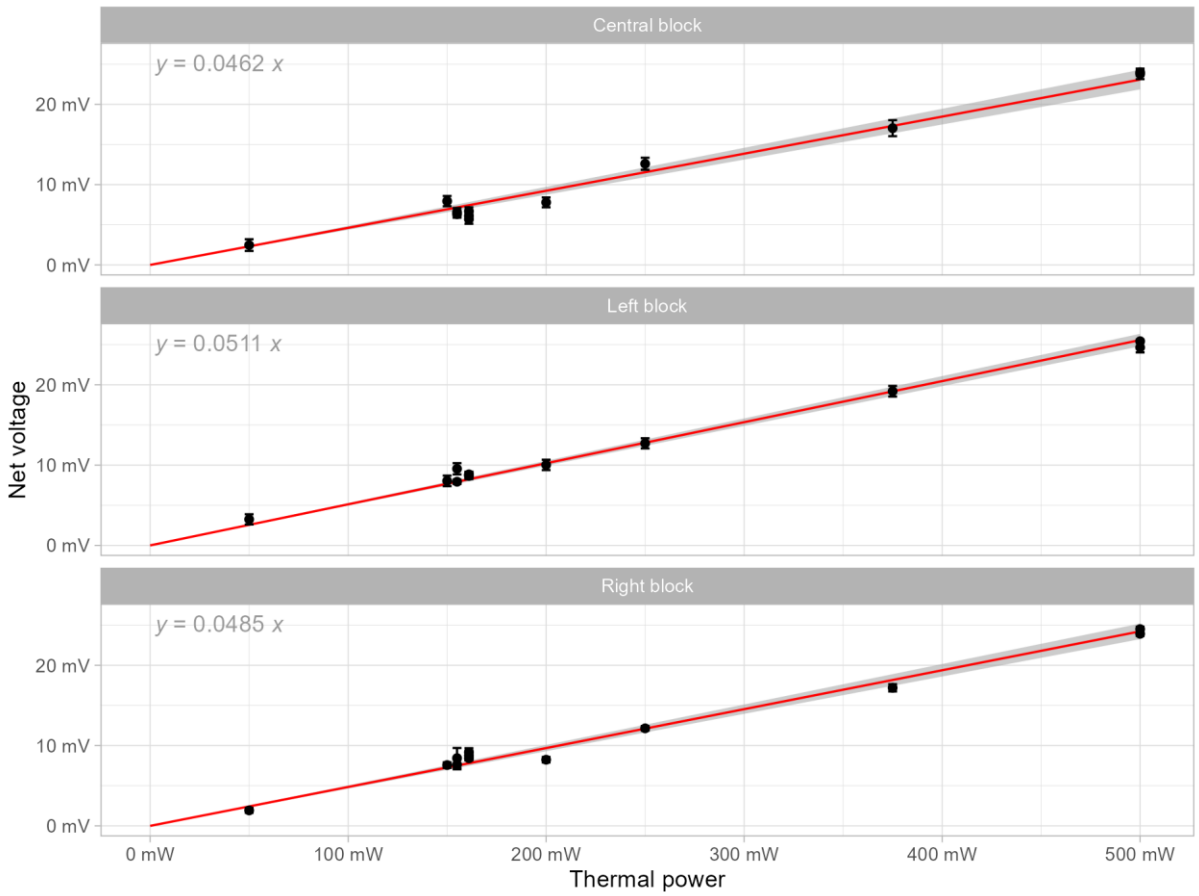

FIGURE 38. OVERVIEW OF CLASSIC LINEAR MODEL FITS, WITHOUT INTERCEPT, AND THE CORRESPONDING 95% CONFIDENCE INTERVALS, FOR EVERY CALORIMETER BLOCK INDIVIDUALLY. THE SENSITIVITY COEFFICIENT EQUALS THE SLOPE OF THE FITTED LINE IN THIS CASE.

5.2.2 Posterior distributions of sensitivity coefficients

The three Bayesian regression exercises were implemented and MCMC sampling was performed with a warmup of 5000 samples for the two simpler cases, and 20000 for the hierarchical approach. After warmup, 5000 draws of the posterior were collected each time. The point estimate of the multivariate potential scale reduction factor was always <= 1.06, indicating convergence is reached in all cases. The exercise was repeated by only considering the joule effect pulses to see how including all data points would compare to the standard calibration approach. The results of the latter where then passed on to the following exercises described in Sections 5.3 and 5.4.

An overview on all obtained sensitivity coefficient estimates is provided in Table 28. Note that although we provide a mean and standard deviation, this does not necessarily mean these follow a Gaussian distribution. For the

hierarchical approach we need mixed predictive replication (posterior vs prior predictive check for the hyperparameters vs sensitivity priors) to obtain draws of the sensitivity coefficients applicable to any new measurement that would be performed. In almost all cases the resulting distribution exhibits slightly heavier tails than a Gaussian one. A Gaussian distribution is however still a reasonable, and definitely practical, approximation here, so this is used in Sections 5.3 and 5.4, using the parameters from Table 28 for the Bayesian hierarchical approach with only joule effect pulse data.

Finally, to make sure that the probabilistic model fit is satisfactory, we performed posterior predictive checks. The results for the pulse data set are provided in Figure 39, which makes very clear that some gross voltages cannot be reproduced in case of a single sensitivity coefficient for the total signal, or unique sensitivity coefficients per block. Instead, the hierarchical approach allows to fit all observed gross voltages very well, and hence the larger uncertainty on the sensitivity coefficients, as shown in Table 28, is justified.

TABLE 28. OVERVIEW OF THE MEAN AND STANDARD DEVIATION ESTIMATES FOR THE DIFFERENT APPROACHES. IN CASE OF BAYESIAN INFERENCE, THE POSTERIOR DISTRIBUTIONS ARE NOT NECESSARILY GAUSSIAN, AND THE VALUES WHERE A SHAPIRO-WILK TEST WOULD REJECT THAT HYPOTHESIS AT SIGNIFICANCE LEVEL OF 0.05 ARE LABELLED WITH AN ASTERISK.

Method	Approach	Data	S_l		S_r		S_c	
			Mean	SD	Mean	SD	Mean	SD
Classic	Single	Pulses	48.47	0.60	48.47	0.60	48.47	0.60
Bayesian	Single	Pulses	49.07	0.10	49.07	0.10	49.07	0.10
Classic	Triple	Pulses	50.50	0.51	47.62	0.81	47.28	1.01
Bayesian	Triple	Pulses	49.31	0.14	49.05	0.16	48.08	0.29
Bayesian	Hierarchical	Pulses	49.13*	1.41*	47.22*	2.72*	46.91*	3.37*
Classic	Single	All	48.60	0.48	48.60	0.48	48.60	0.48
Bayesian	Single	All	49.09	0.10	49.09	0.10	49.09	0.10
Classic	Triple	All	51.15	0.71	48.45	0.88	46.19	1.11
Bayesian	Triple	All	49.54	0.13	49.21	0.16	46.79	0.27
Bayesian	Hierarchical	All	51.62*	2.49*	49.24*	3.07*	43.19	3.84

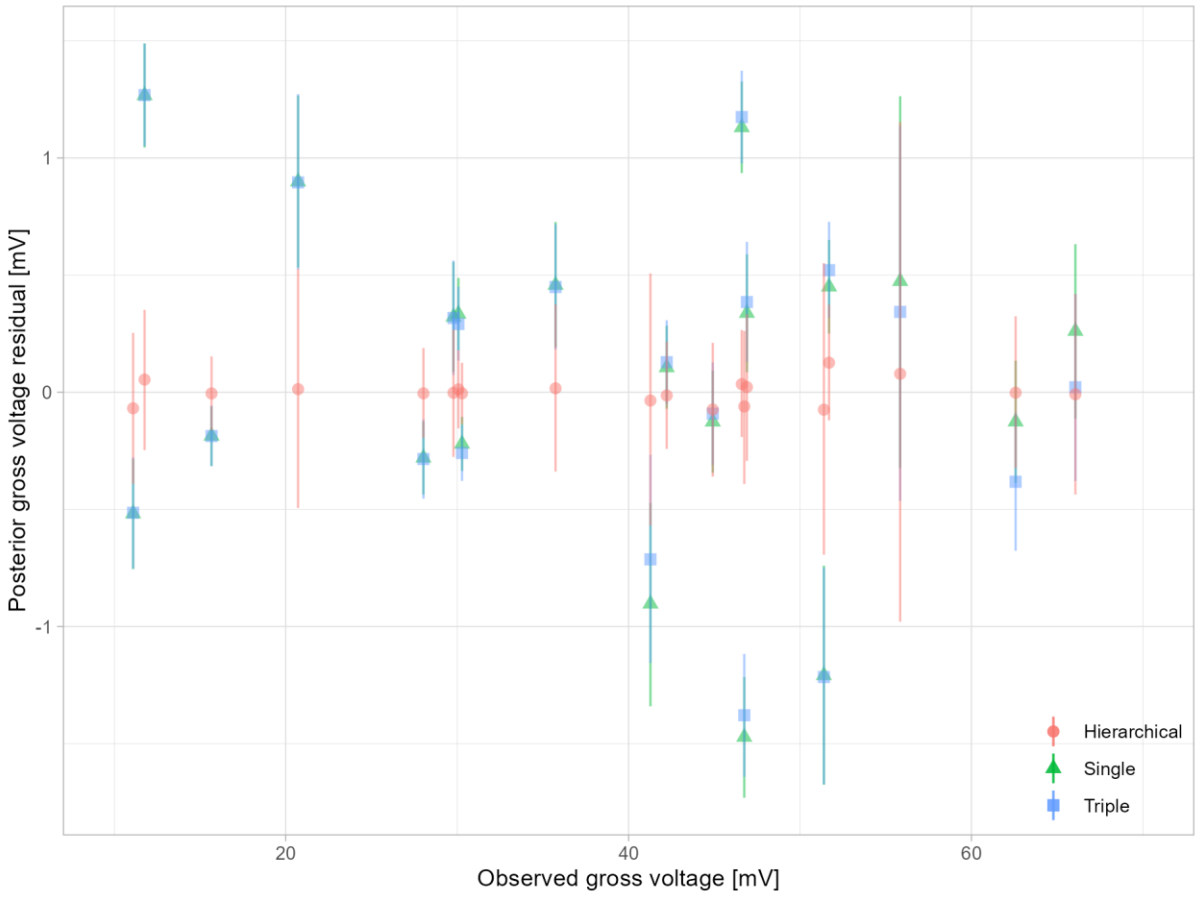

FIGURE 39. POSTERIOR PREDICTIVE CHECK FOR THE GROSS VOLTAGES, FOR THE THREE APPROACHES APPLIED TO THE JOULE EFFECT PULSE DATA. THE MEAN IS USED HERE AS MEASURE OF CENTRAL TENDENCY, WHILE THE ERROR BARS REPRESENT THE 95% CREDIBLE INTERVAL.

5.3 The mock-up drums and reference sources exercise

5.3.1 Methodology

The mock-up drums were stylized as containing 21 potential point source locations (brown cylinders in Figure 40). With respect to gamma spectrometry, we used the forward model described in [28] to go from the distributions of activities across the 21 locations (instead of segments in [28]) to simulated counts. We then applied the same idea to (1) the PNCC model presented by [40] to simulate the PNCC data, and (2) the CAL model described in Section 5.2 to simulate the CAL data, assuming 100% efficiency for the latter.

Some methodological advances were introduced here, however, compared to [28]. These are detailed for the real drum in [41], and briefly described for the mock-up drums here. As described in [41], we use Dirichlet prior distributions for the inferred quantities that must sum to one: the isotopic vector, spatial distribution of the fractions of the total Pu content across the 21 locations and the 3 matrix-efficiency coefficients. The latter coefficients are introduced here, as for the mock-up drums exercise, we were working with three different drum matrices, each with its own set of efficiencies for the different measurement techniques, while for the real unconditioned waste drum, the matrix properties were constant and considered deterministic. Hence we now interpolate efficiencies linearly between three end members: Mock-up 201 (ethafoam), mock-up 205 (PVC, steel and ethafoam) and mock-

up 206 (XPS and mortar). The total Pu content was itself assigned a log uniform prior between 10^{-2} g and 100 g. Depending on the considered information context (FULLY KNOWN, REALISTIC or MYSTERY DRUM), we use either flat Dirichlet priors (MYSTERY DRUM case, nothing is known in advance) or a combination of flat and informative Dirichlet priors (REALISTIC case, where the spatial distribution is not known, but some information is available on the isotopic vector and drum matrix).

The used likelihood functions are a Poisson likelihood for the count data (ISOCS and Q2), a Gaussian likelihood for the PNCC datum, and 3 other Gaussian likelihoods for the 3 CAL signals. Convergence of the MCMC was monitored with the R-hat convergence criterion by [42].

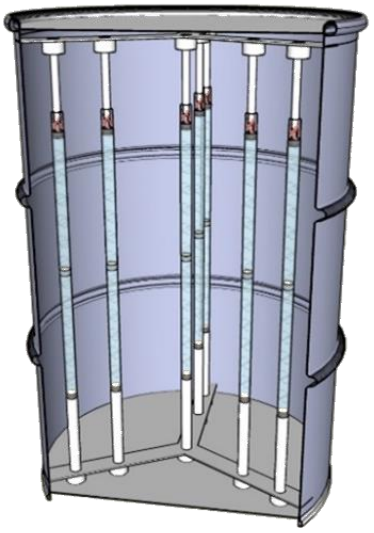

FIGURE 40. POSSIBLE SOURCE LOCATIONS (SMALL BROWN CYLINDERS) WITHIN A MOCK-UP DRUM, WITH THREE LOCATIONS (LOWER, MID, AND UPPER) FOR EACH OF SEVEN PINHOLES.

5.3.2 Posterior distributions of radioisotope masses

The inference results for the 5 mock-up setups are presented in Figure 41 to Figure 70. Overall, it is observed that the gamma spectrometry data (whether ISOCS or 3AX-SGS) mostly always allow for an accurate characterization of the gamma-emitting radionuclides together with those non-gamma emitting ones of which prior estimates can be obtained by gamma-based isotopic composition analysis (Pu-242, Np-237, U-235) using for instance the FRAM software. If a sufficiently informative (and accurate) prior distribution is used for the isotopic vector, then CAL, PNCC and the combination CAL-PNCC can also recover relatively accurate mean estimates of the masses of these radionuclides but with a larger uncertainty than for 3AX-SGS and ISOCS.

5.3.2.1 Setup 5 (mock-up 201 with ethafoam – 21 sources)

Figure 41 to Figure 46 present the inversion results for Setup 5 (drum 201 – 21 sources) and the three information degrees, FULLY KNOWN, REALISTIC and MYSTERY DRUM. For each information degree, 11 combinations of measurement methods are considered.

It is seen that under the FULLY KNOWN assumption, all the ISOCS-based estimates are biased while the Q2-based ones are quite good. This seems to indicate that our calculated ISOCS-associated efficiencies have some bias while the calculated Q2-asscociated efficiencies are very accurate. In contrast, under the more flexible REALISTIC and

MYSTERY DRUM assumptions, the ISOCS-based results get to some extent better, in the sense that the posterior radionuclide mass distributions tend to peak near the true values. As expected, these posterior distributions are also wider (that is, more uncertain). For the Q2-based estimates, the opposite situation is observed. When the MCMC has more flexibility to fit the measurement data (REALISTIC and MYSTERY DRUM hypotheses) the radionuclide mass estimates become quite biased. The MCMC jumps to these wrong estimates because in combination with specific sampled values of the other unknown parameters, they induce a better fit to the data (not shown). This indicates that complex compensation effects are at play and warrants further investigations.

Overall, it is also observed that CAL and PNCC have little added value here when combined with gamma spectrometry (ISOCS and Q2). The main raison for this is that our gamma spectrometry setups measured a lot of counts (matrix densities are rather limited) while we mostly have gamma-emitting nuclides in our sources (all considered nuclides but Np-237 and Pu-242, both present in low amounts). Moreover, when prior information is available about the isotopic vector (REALISTIC assumption) then CAL and PNCC provide good estimates though with some relatively large uncertainty. Not surprisingly, if no information about the vector is available (MYSTERY DRUM) CAL and PNCC fail to provide any meaningful characterization when not combined with other techniques.

Despite the large amount of information obtained here from the gamma spectrometry measurement, the relative robustness of calorimetry with respect to the matrix effect is still visible in the REALISTIC and MYSTERY DRUM combinations involving Q2, and the MYSTERY DRUM combinations involving ISOCS. The combinations involving calorimetry led there to the smallest uncertainties.

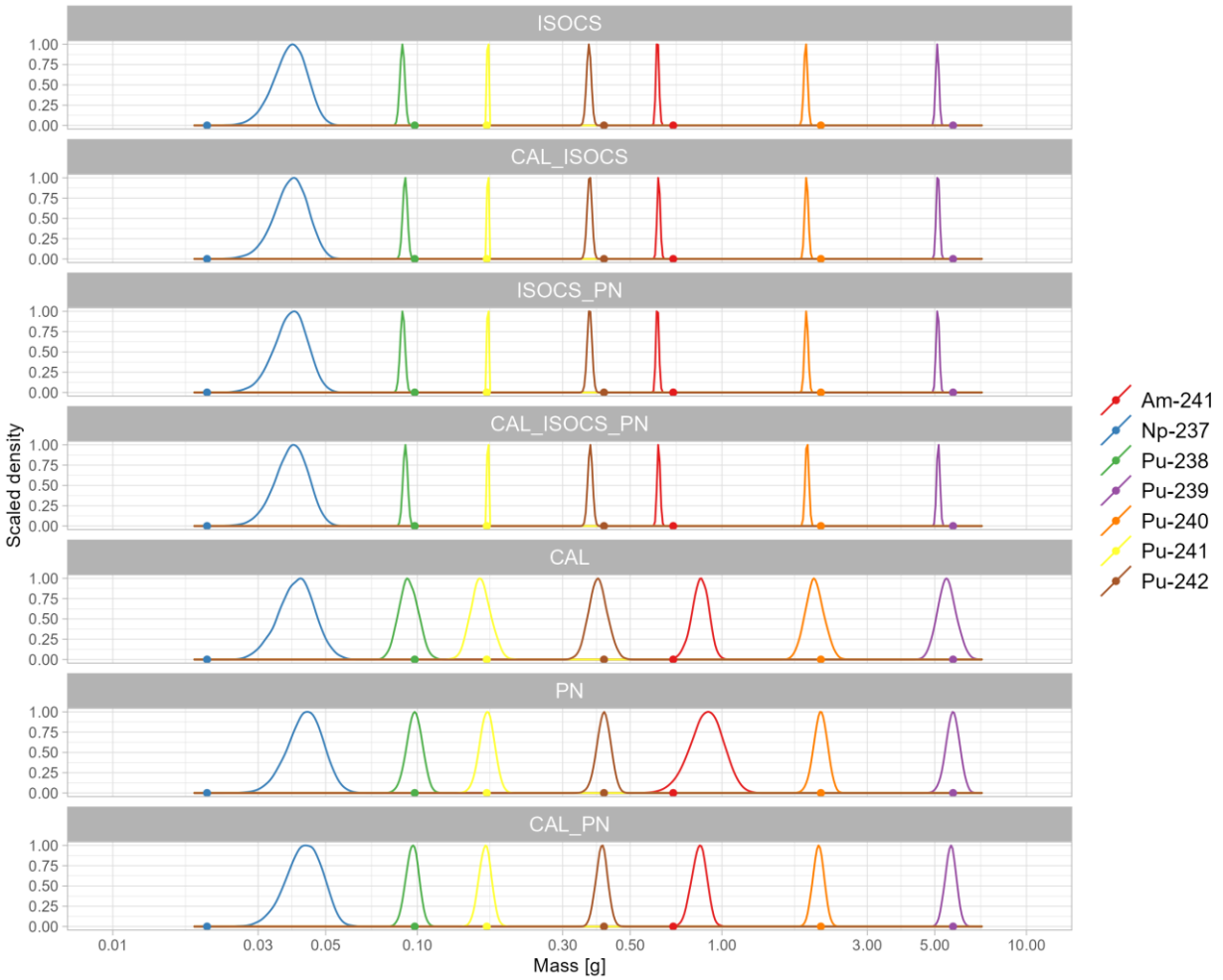

FIGURE 41. POSTERIOR DISTRIBUTIONS OF THE INFERRED RADIONUCLIDES' MASSES OVER THE WHOLE DRUM 201 (21 SOURCES) FOR DIFFERENT MEASUREMENT TECHNIQUES AND COMBINATIONS THEREOF (ISOCS, CAL-ISOCS, ISOCS-PN, CAL-ISOCS-PN, CAL, PN AND CAL-PN). THE CONSIDERED INFORMATION DEGREE IS FULLY KNOWN WHERE THE ONLY UNKNOWNS ARE BASICALLY THE RADIONUCLIDES' ACTIVITIES WHILE THE DRUM'S MATRIX, ISOTOPIC VECTOR AND PU SPATIAL DISTRIBUTION ARE ASSUMED TO BE KNOWN. PN MEANS PNCC. THE SOLID DOTS DENOTE THE TRUE VALUES.

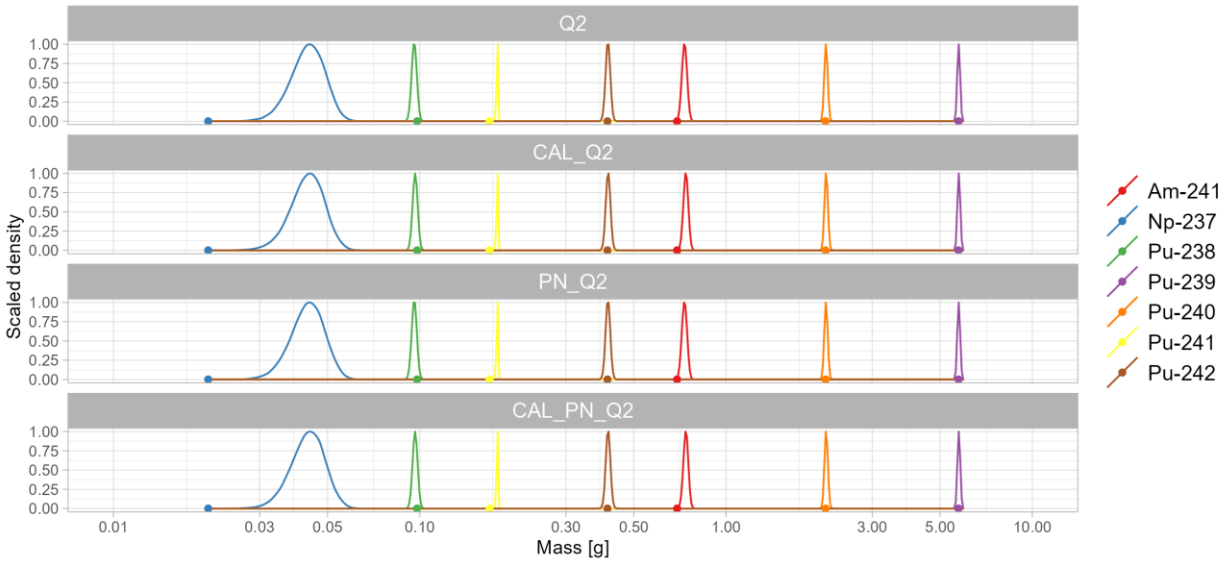

FIGURE 42. POSTERIOR DISTRIBUTIONS OF THE INFERRED RADIONUCLIDES' MASSES OVER THE WHOLE DRUM 201 (21 SOURCES) FOR DIFFERENT MEASUREMENT TECHNIQUES AND COMBINATIONS THEREOF (Q2, CAL-Q2, PN-Q2 AND CAL-PN-Q2). THE CONSIDERED INFORMATION DEGREE IS FULLY KNOWN WHERE THE ONLY UNKNOWNS ARE BASICALLY THE RADIONUCLIDES' ACTIVITIES WHILE THE DRUM'S MATRIX, ISOTOPIC VECTOR AND PU SPATIAL DISTRIBUTION ARE ASSUMED TO BE KNOWN. PN MEANS PNCC. THE SOLID DOTS DENOTE THE TRUE VALUES.

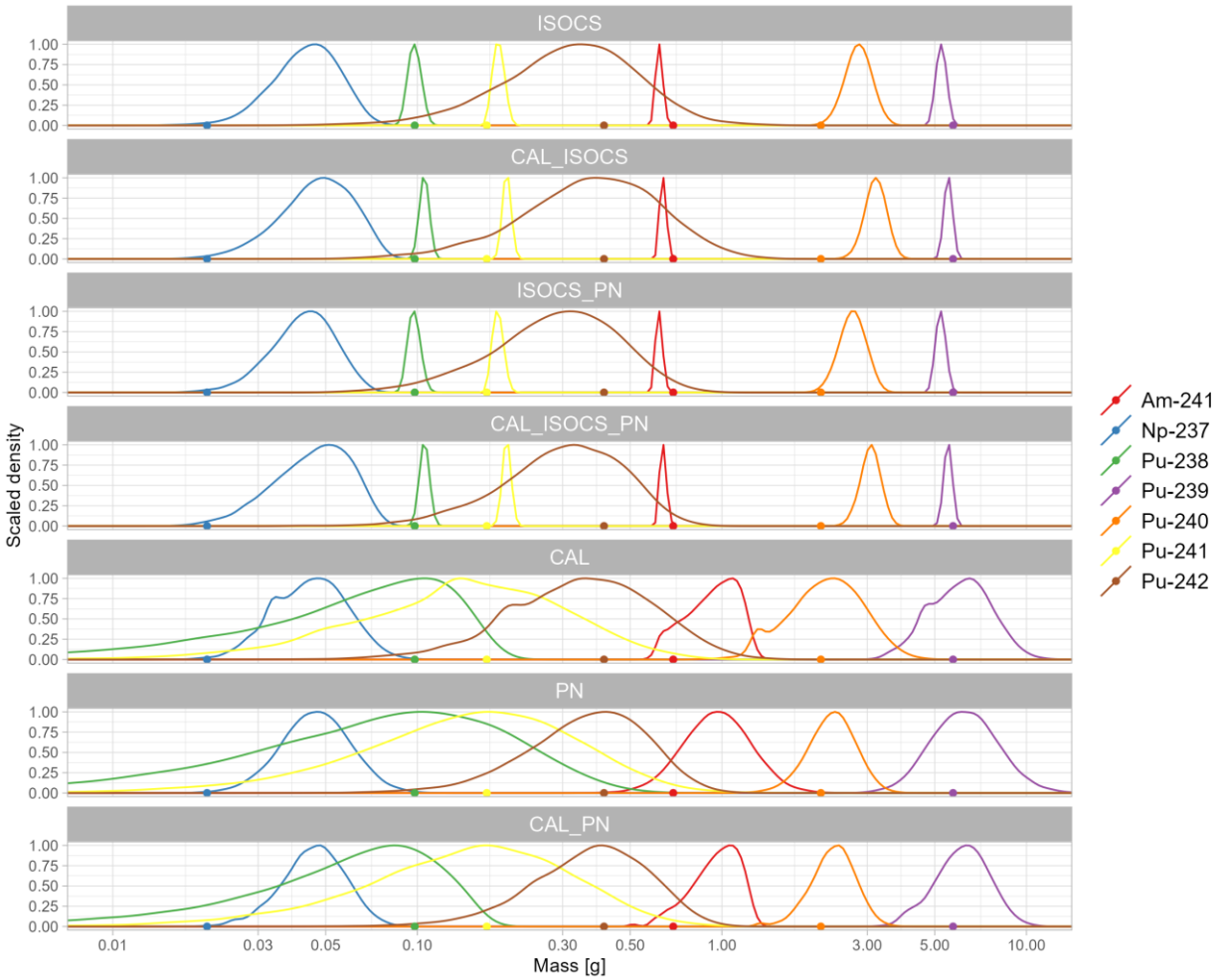

FIGURE 43. POSTERIOR DISTRIBUTIONS OF THE INFERRED RADIONUCLIDES' MASSES OVER THE WHOLE DRUM 201 (21 SOURCES) FOR DIFFERENT MEASUREMENT TECHNIQUES AND COMBINATIONS THEREOF (ISOCS, CAL-ISOCS, ISOCS-PN, CAL-ISOCS-PN, CAL, PN AND CAL-PN). THE CONSIDERED INFORMATION DEGREE IS REALISTIC WHERE REALISTIC PRIOR KNOWLEDGE ON THE DRUM'S MATRIX AND ISOTOPIC VECTOR IS TAKEN INTO ACCOUNT. PN MEANS PNCC. THE SOLID DOTS DENOTE THE TRUE VALUES.

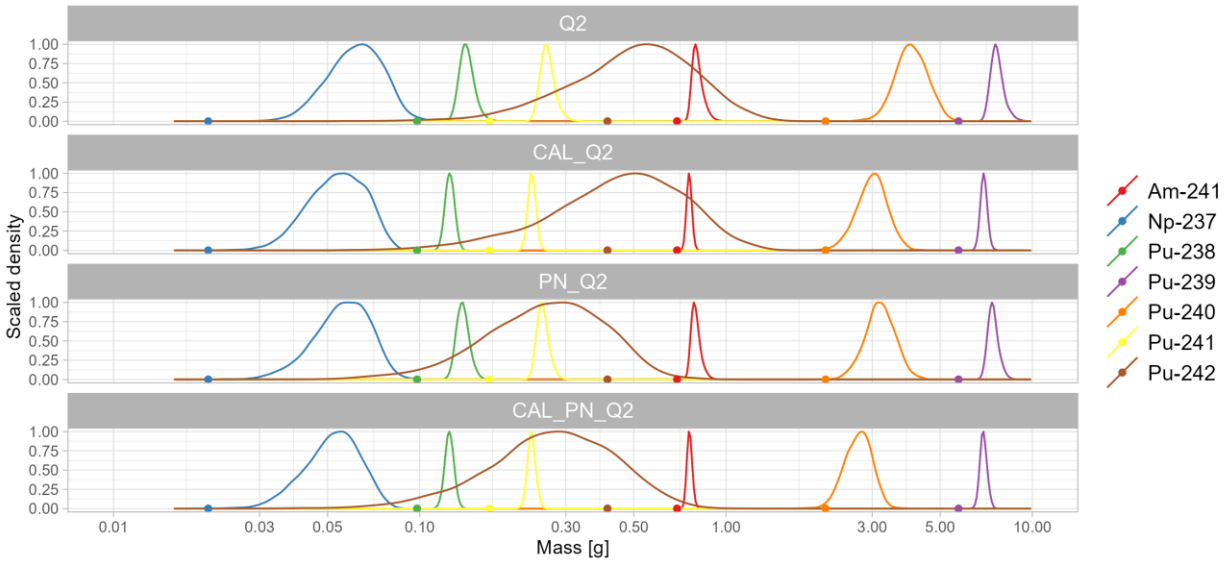

FIGURE 44. POSTERIOR DISTRIBUTIONS OF THE INFERRED RADIONUCLIDES' MASSES OVER THE WHOLE DRUM 201 (21 SOURCES) FOR DIFFERENT MEASUREMENT TECHNIQUES AND COMBINATIONS THEREOF (Q2, CAL-Q2, PN-Q2 AND CAL-PN-Q2). THE CONSIDERED INFORMATION DEGREE IS REALISTIC WHERE REALISTIC PRIOR KNOWLEDGE ON THE DRUM'S MATRIX AND ISOTOPIC VECTOR IS TAKEN INTO ACCOUNT. PN MEANS PNCC. THE SOLID DOTS DENOTE THE TRUE VALUES.

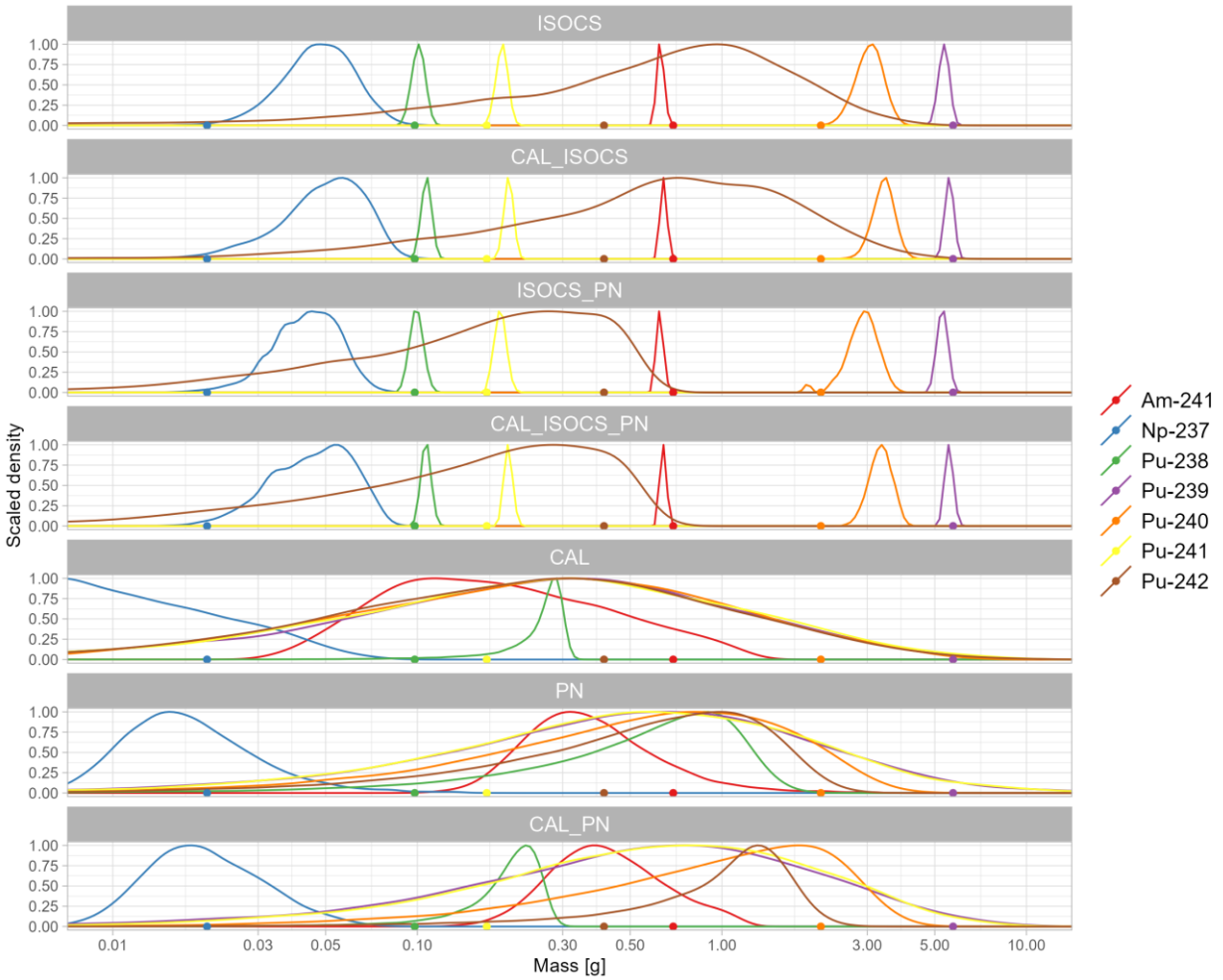

FIGURE 45. POSTERIOR DISTRIBUTIONS OF THE INFERRED RADIONUCLIDES' MASSES OVER THE WHOLE DRUM 201 (21 SOURCES) FOR DIFFERENT MEASUREMENT TECHNIQUES AND COMBINATIONS THEREOF (ISOCS, CAL-ISOCS, ISOCS-PN, CAL-ISOCS-PN, CAL, PN AND CAL-PN). THE CONSIDERED INFORMATION DEGREE IS MYSTERY DRUM WHERE NO PRIOR KNOWLEDGE ON THE DRUM'S MATRIX AND ISOTOPIC VECTOR IS CONSIDERED. PN MEANS PNCC. THE SOLID DOTS DENOTE THE TRUE VALUES.

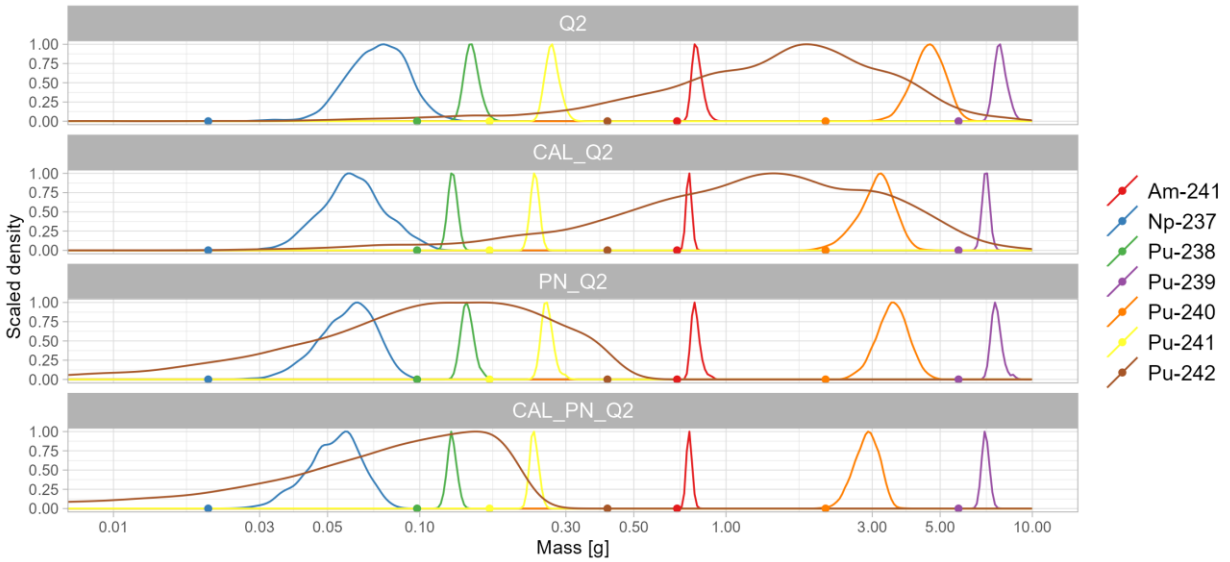

FIGURE 46. POSTERIOR DISTRIBUTIONS OF THE INFERRED RADIONUCLIDES' MASSES OVER THE WHOLE DRUM 201 (21 SOURCES) FOR DIFFERENT MEASUREMENT TECHNIQUES AND COMBINATIONS THEREOF (Q2, CAL-Q2, PN-Q2 AND CAL-PN-Q2). THE CONSIDERED INFORMATION DEGREE IS MYSTERY DRUM WHERE NO PRIOR KNOWLEDGE ON THE DRUM'S MATRIX AND ISOTOPIC VECTOR IS CONSIDERED. PN MEANS PNCC. THE SOLID DOTS DENOTE THE TRUE VALUES.

5.3.2.2 Setup 6 (mock-up 205 with ethafoam, steel and pvc – 21 sources)

Figure 47 to Figure 52 display the inversion results for Setup 6 (drum 201 – 21 sources). These figures reveal very similar findings as for drum 201 – 21 sources (section 5.3.2.1) which for brevity, are not repeated here.

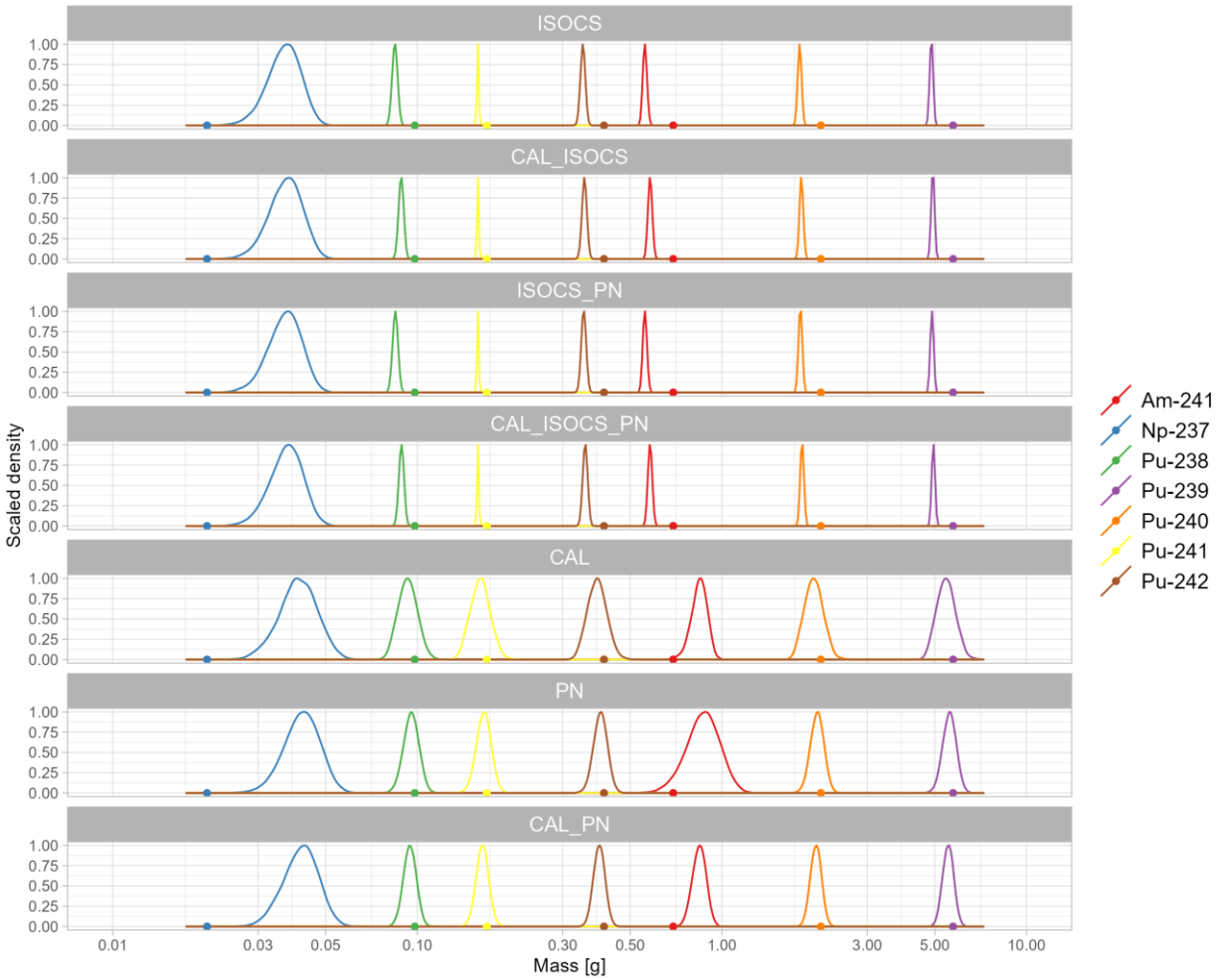

FIGURE 47. POSTERIOR DISTRIBUTIONS OF THE INFERRED RADIONUCLIDES' MASSES OVER THE WHOLE DRUM 205 (21 SOURCES) FOR DIFFERENT MEASUREMENT TECHNIQUES AND COMBINATIONS THEREOF (ISOCS, CAL-ISOCS, ISOCS-PN, CAL-ISOCS-PN, CAL, PN AND CAL-PN). THE CONSIDERED INFORMATION DEGREE IS FULLY KNOWN WHERE THE ONLY UNKNOWNS ARE BASICALLY THE RADIONUCLIDES' ACTIVITIES WHILE THE DRUM'S MATRIX, ISOTOPIC VECTOR AND PU SPATIAL DISTRIBUTION ARE ASSUMED TO BE KNOWN. PN MEANS PNCC.

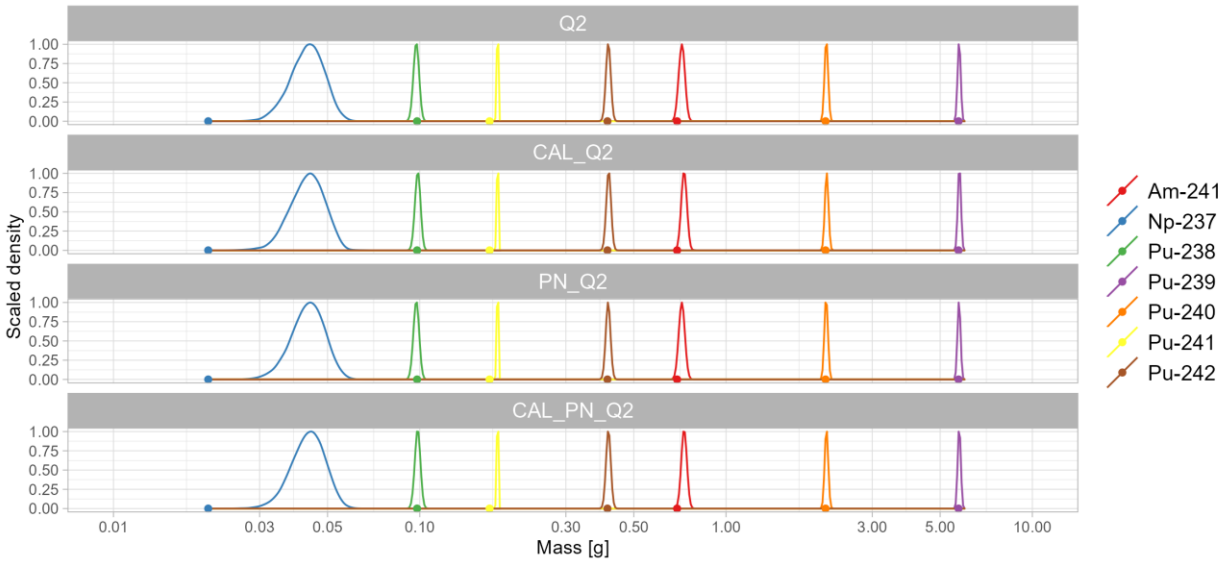

FIGURE 48. POSTERIOR DISTRIBUTIONS OF THE INFERRED RADIONUCLIDES' MASSES OVER THE WHOLE DRUM 205 (21 SOURCES) FOR DIFFERENT MEASUREMENT TECHNIQUES AND COMBINATIONS THEREOF (Q2, CAL-Q2, PN-Q2 AND CAL-PN-Q2). THE CONSIDERED INFORMATION DEGREE IS FULLY KNOWN WHERE THE ONLY UNKNOWNS ARE BASICALLY THE RADIONUCLIDES' ACTIVITIES WHILE THE DRUM'S MATRIX, ISOTOPIC VECTOR AND PU SPATIAL DISTRIBUTION ARE ASSUMED TO BE KNOWN. PN MEANS PNCC. THE SOLID DOTS DENOTE THE TRUE VALUES.

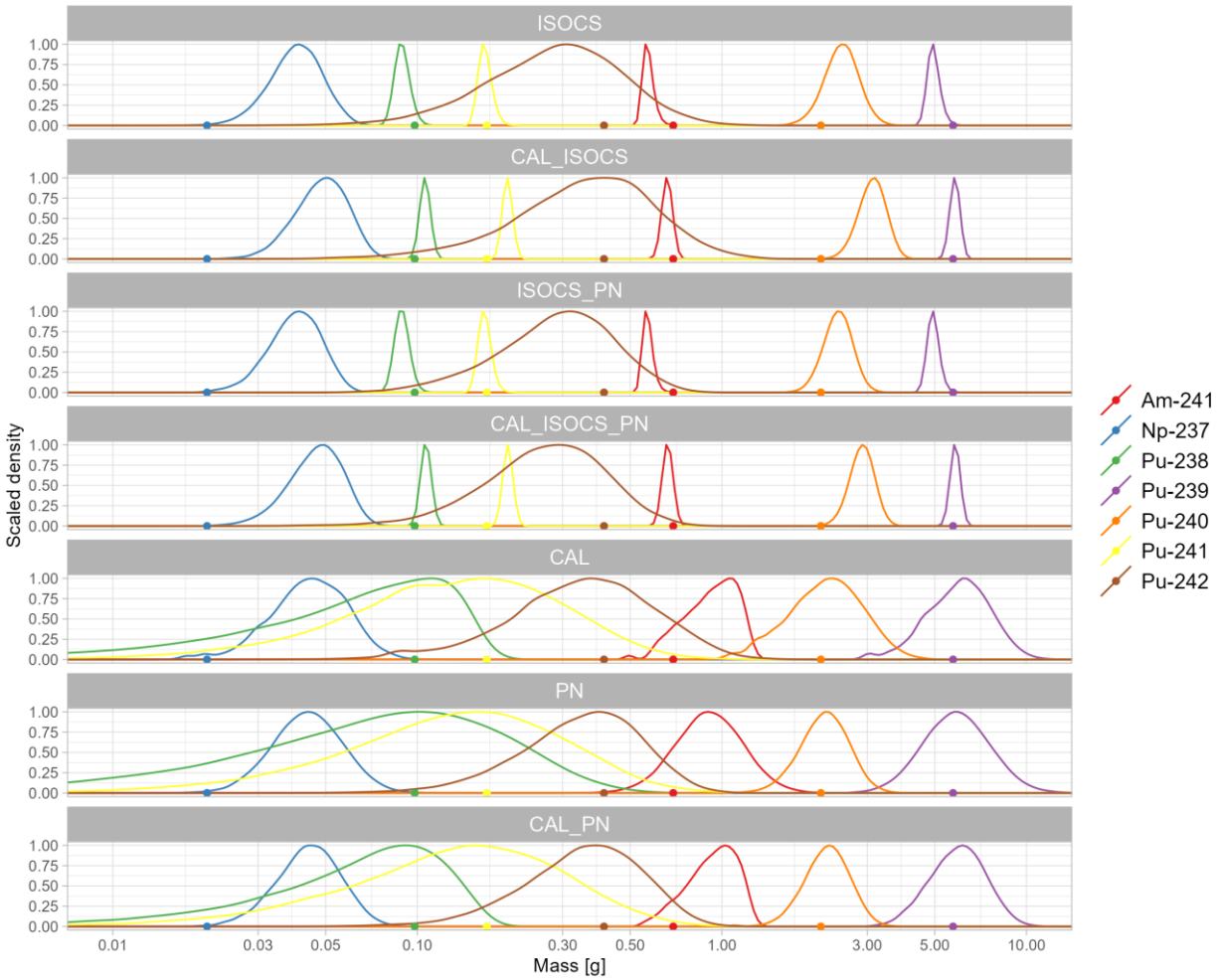

FIGURE 49. POSTERIOR DISTRIBUTIONS OF THE INFERRED RADIONUCLIDES' MASSES OVER THE WHOLE DRUM 205 (21 SOURCES) FOR DIFFERENT MEASUREMENT TECHNIQUES AND COMBINATIONS THEREOF (ISOCS, CAL-ISOCS, ISOCS-PN, CAL-ISOCS-PN, CAL, PN AND CAL-PN). THE CONSIDERED INFORMATION DEGREE IS REALISTIC WHERE REALISTIC PRIOR KNOWLEDGE ON THE DRUM'S MATRIX AND ISOTOPIC VECTOR IS TAKEN INTO ACCOUNT. PN MEANS PNCC. THE SOLID DOTS DENOTE THE TRUE VALUES.

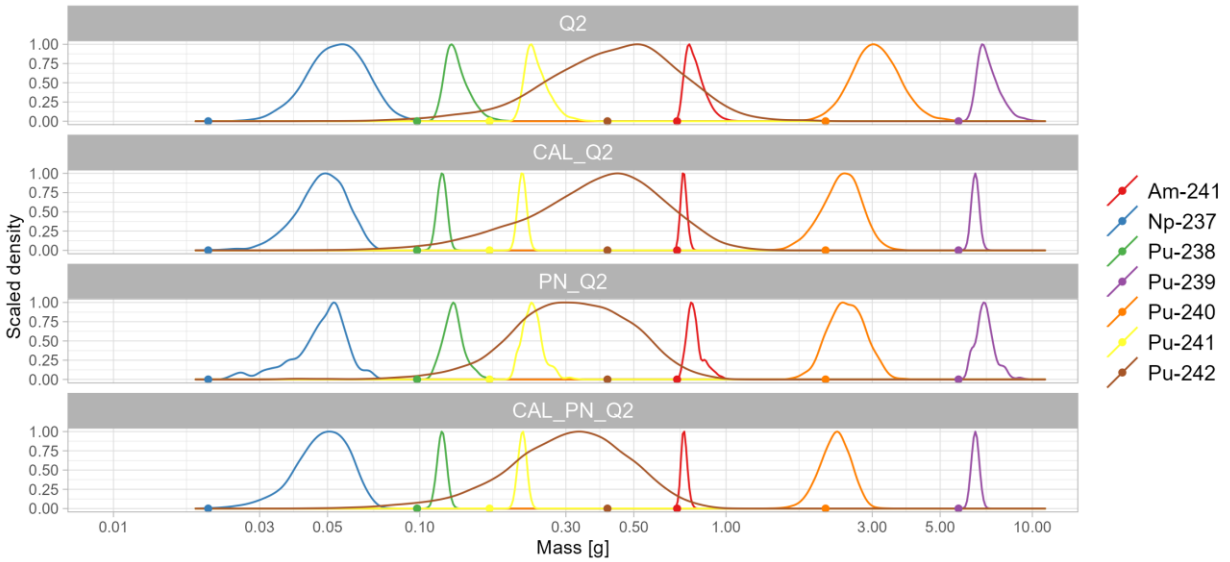

FIGURE 50. POSTERIOR DISTRIBUTIONS OF THE INFERRED RADIONUCLIDES' MASSES OVER THE WHOLE DRUM 205 (21 SOURCES) FOR DIFFERENT MEASUREMENT TECHNIQUES AND COMBINATIONS THEREOF (Q2, CAL-Q2, PN-Q2 AND CAL-PN-Q2). THE CONSIDERED INFORMATION DEGREE IS REALISTIC WHERE REALISTIC PRIOR KNOWLEDGE ON THE DRUM'S MATRIX AND ISOTOPIC VECTOR IS TAKEN INTO ACCOUNT. PN MEANS PNCC. THE SOLID DOTS DENOTE THE TRUE VALUES.

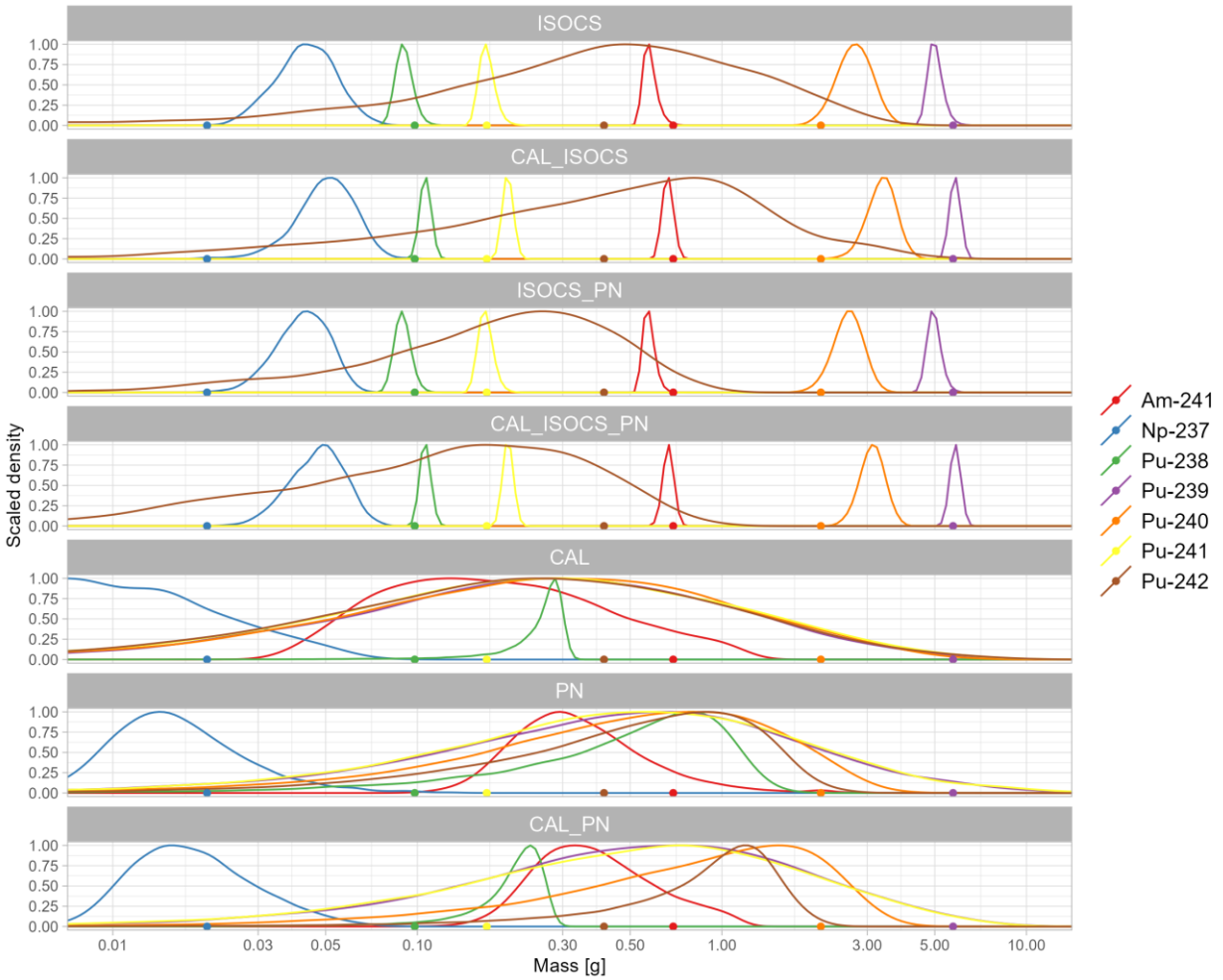

FIGURE 51. POSTERIOR DISTRIBUTIONS OF THE INFERRED RADIONUCLIDES' MASSES OVER THE WHOLE DRUM 205 (21 SOURCES) FOR DIFFERENT MEASUREMENT TECHNIQUES AND COMBINATIONS THEREOF (ISOCS, CAL-ISOCS, ISOCS-PN, CAL-ISOCS-PN, CAL, PN AND CAL-PN). THE CONSIDERED INFORMATION DEGREE IS MYSTERY DRUM WHERE NO PRIOR KNOWLEDGE ON THE DRUM'S MATRIX AND ISOTOPIC VECTOR IS CONSIDERED. PN MEANS PNCC. THE SOLID DOTS DENOTE THE TRUE VALUES.

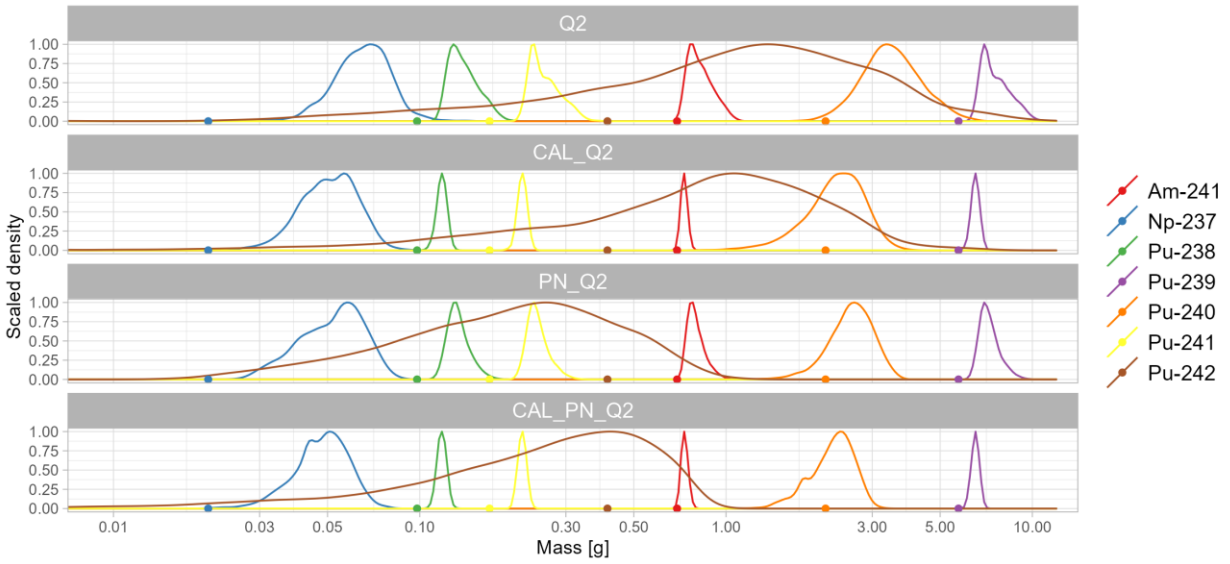

FIGURE 52. POSTERIOR DISTRIBUTIONS OF THE INFERRED RADIONUCLIDES' MASSES OVER THE WHOLE DRUM 205 (21 SOURCES) FOR DIFFERENT MEASUREMENT TECHNIQUES AND COMBINATIONS THEREOF (Q2, CAL-Q2, PN-Q2 AND CAL-PN-Q2). THE CONSIDERED INFORMATION DEGREE IS MYSTERY DRUM WHERE NO PRIOR KNOWLEDGE ON THE DRUM'S MATRIX AND ISOTOPIC VECTOR IS CONSIDERED. PN MEANS PNCC. THE SOLID DOTS DENOTE THE TRUE VALUES.

5.3.2.3 Setup 2 (mock-up 206 with mortar and XPS – 21 sources)

The global results for Setup 2 (mock-up 206-21 sources) are different than those obtained for Setups 5 and 6 (which as stated above are rather similar). Here both the ISOCS and Q2 efficiencies show some bias under the FULLY KNOWN assumption (Figure 53 and Figure 54). In contrast, PNCC and CAL remain rather accurate, but exhibit larger uncertainties. When moving to the REALISTIC setup, posterior uncertainty increases significantly but the ISOCS and Q2-based posterior distributions now peak near the correct values (Figure 55, Figure 56). Lastly, under the MYSTERY DRUM assumption the posterior uncertainty associated with the ISOCS-based inversions can get very large, such as for Pu-240 (orange lines in Figure 57). This is not observed for the Q2-based inversions for which posterior uncertainty remains reasonable (Figure 58).

Again, REALISTIC and MYSTERY DRUM combinations involving calorimetry reveal slightly less uncertain and more accurate results because of robustness with respect to the matrix effect.

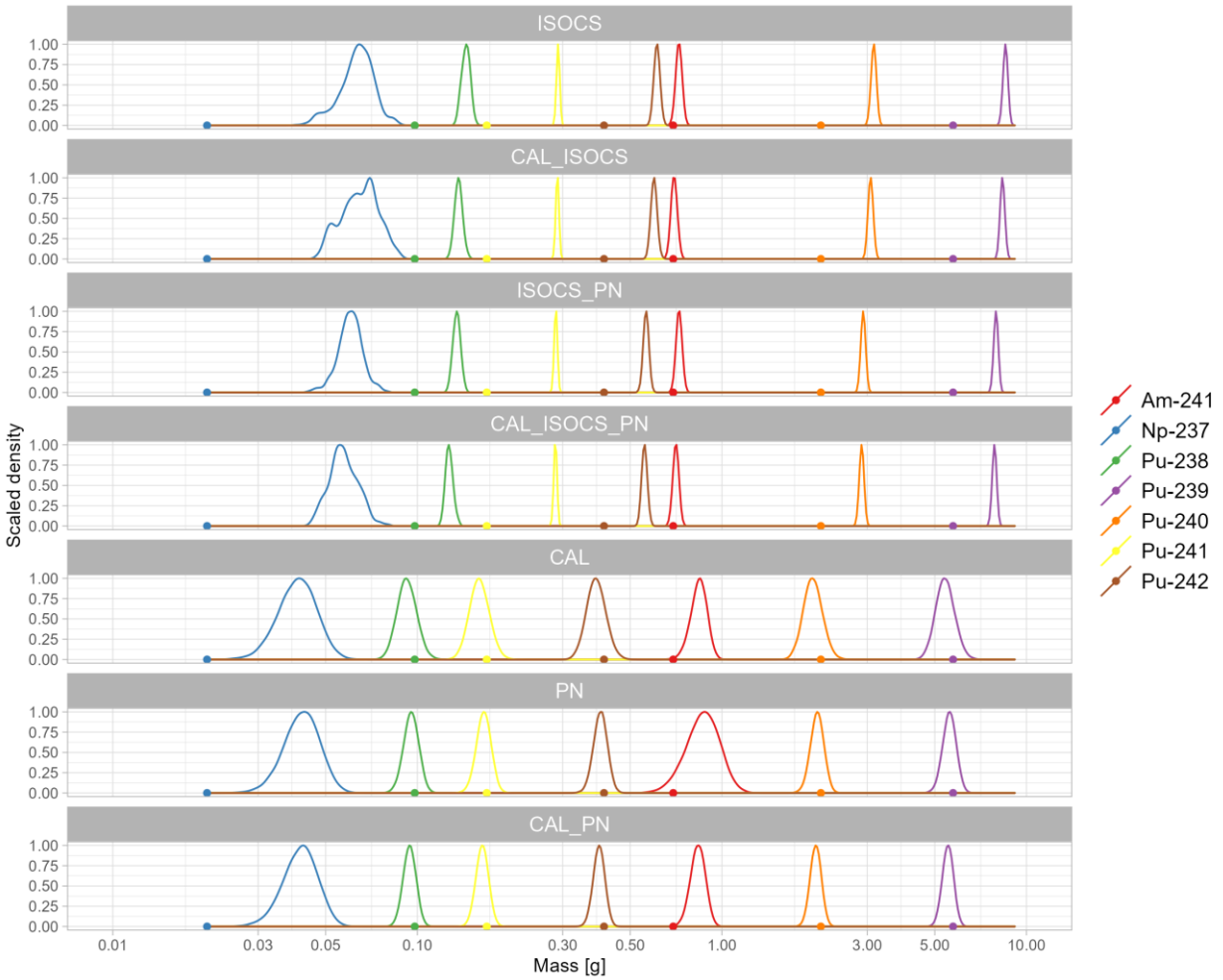

FIGURE 53. POSTERIOR DISTRIBUTIONS OF THE INFERRED RADIONUCLIDES' MASSES OVER THE WHOLE DRUM 206 (21 SOURCES) FOR DIFFERENT MEASUREMENT TECHNIQUES AND COMBINATIONS THEREOF (ISOCS, CAL-ISOCS, ISOCS-PN, CAL-ISOCS-PN, CAL, PN AND CAL-PN). THE CONSIDERED INFORMATION DEGREE IS FULLY KNOWN WHERE THE ONLY UNKNOWNS ARE BASICALLY THE RADIONUCLIDES' ACTIVITIES WHILE THE DRUM'S MATRIX, ISOTOPIC VECTOR AND PU SPATIAL DISTRIBUTION ARE ASSUMED TO BE KNOWN. PN MEANS PNCC. THE SOLID DOTS DENOTE THE TRUE VALUES.

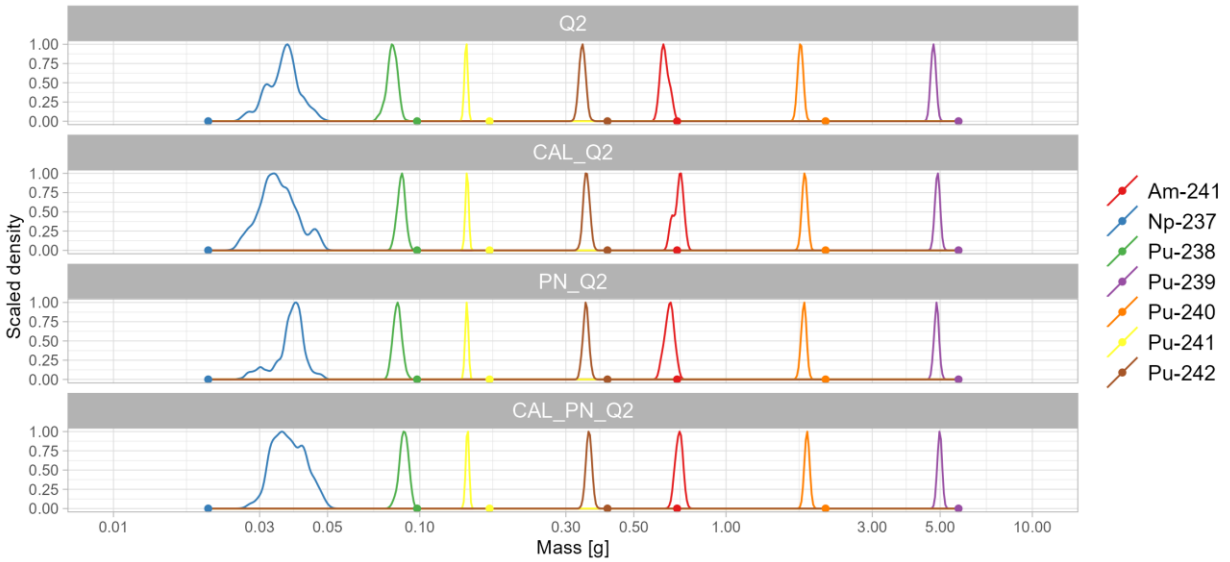

FIGURE 54. POSTERIOR DISTRIBUTIONS OF THE INFERRED RADIONUCLIDES' MASSES OVER THE WHOLE DRUM 206 (21 SOURCES) FOR DIFFERENT MEASUREMENT TECHNIQUES AND COMBINATIONS THEREOF (Q2, CAL-Q2, PN-Q2 AND CAL-PN-Q2). THE CONSIDERED INFORMATION DEGREE IS FULLY KNOWN WHERE THE ONLY UNKNOWNS ARE BASICALLY THE RADIONUCLIDES' ACTIVITIES WHILE THE DRUM'S MATRIX, ISOTOPIC VECTOR AND PU SPATIAL DISTRIBUTION ARE ASSUMED TO BE KNOWN. PN MEANS PNCC. THE SOLID DOTS DENOTE THE TRUE VALUES.

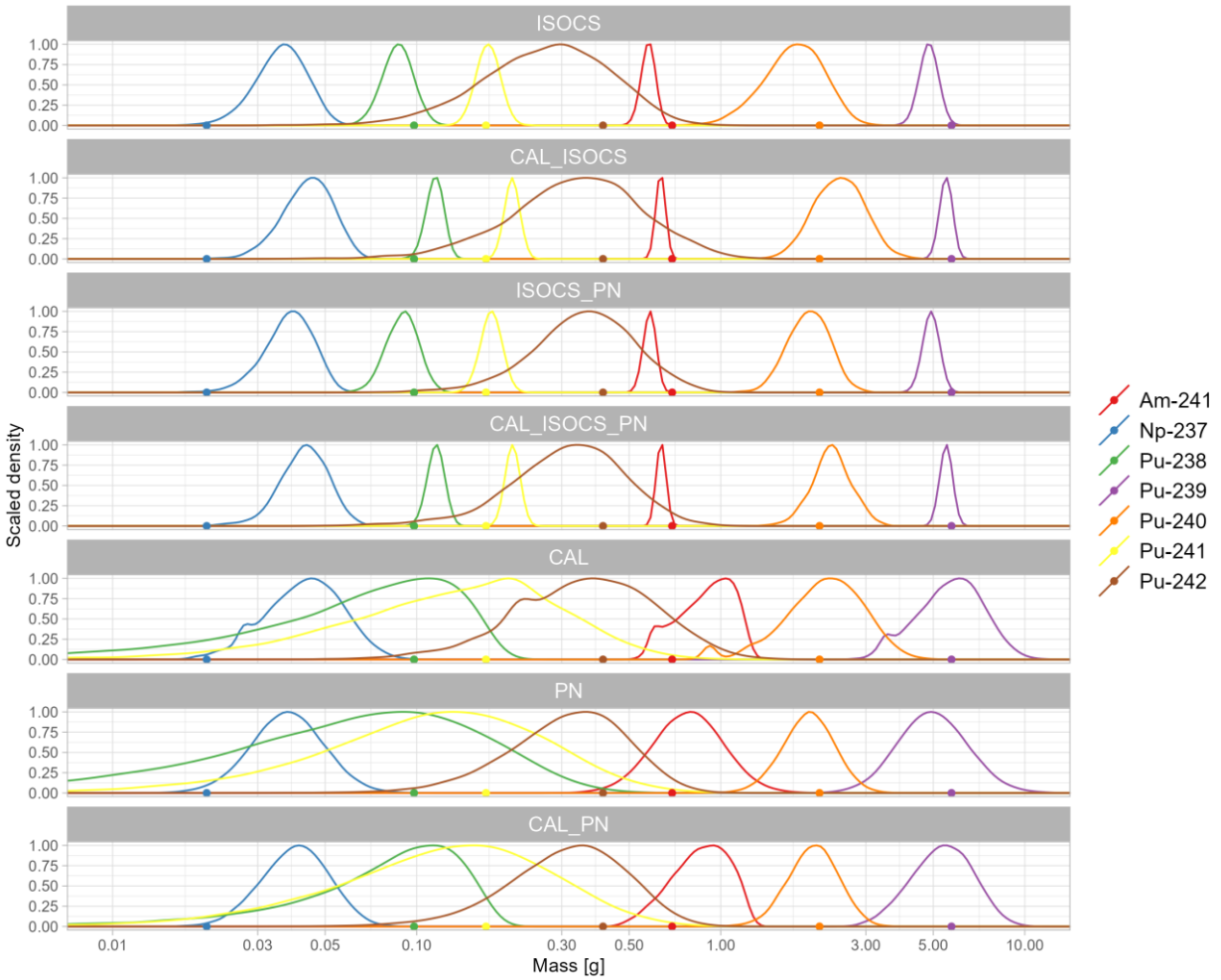

FIGURE 55. POSTERIOR DISTRIBUTIONS OF THE INFERRED RADIONUCLIDES' MASSES OVER THE WHOLE DRUM 206 (21 SOURCES) FOR DIFFERENT MEASUREMENT TECHNIQUES AND COMBINATIONS THEREOF (ISOCS, CAL-ISOCS, ISOCS-PN, CAL-ISOCS-PN, CAL, PN AND CAL-PN). THE CONSIDERED INFORMATION DEGREE IS REALISTIC WHERE REALISTIC PRIOR KNOWLEDGE ON THE DRUM'S MATRIX AND ISOTOPIC VECTOR IS TAKEN INTO ACCOUNT. PN MEANS PNCC. THE SOLID DOTS DENOTE THE TRUE VALUES.

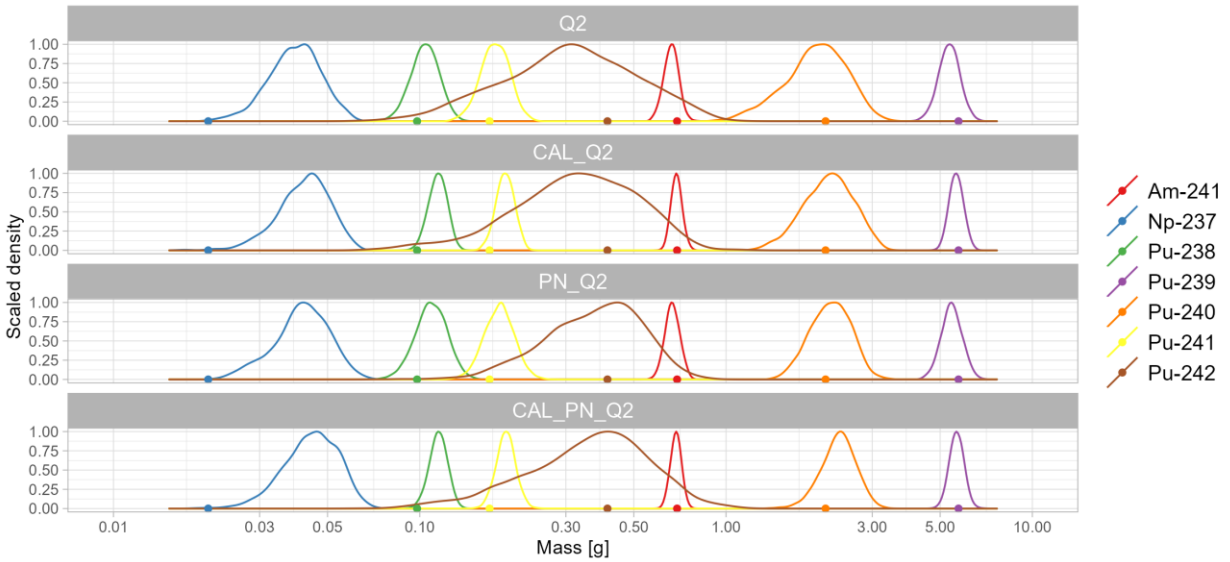

FIGURE 56. POSTERIOR DISTRIBUTIONS OF THE INFERRED RADIONUCLIDES' MASSES OVER THE WHOLE DRUM 206 (21 SOURCES) FOR DIFFERENT MEASUREMENT TECHNIQUES AND COMBINATIONS THEREOF (Q2, CAL-Q2, PN-Q2 AND CAL-PN-Q2). THE CONSIDERED INFORMATION DEGREE IS REALISTIC WHERE REALISTIC PRIOR KNOWLEDGE ON THE DRUM'S MATRIX AND ISOTOPIC VECTOR IS TAKEN INTO ACCOUNT. PN MEANS PNCC. THE SOLID DOTS DENOTE THE TRUE VALUES.

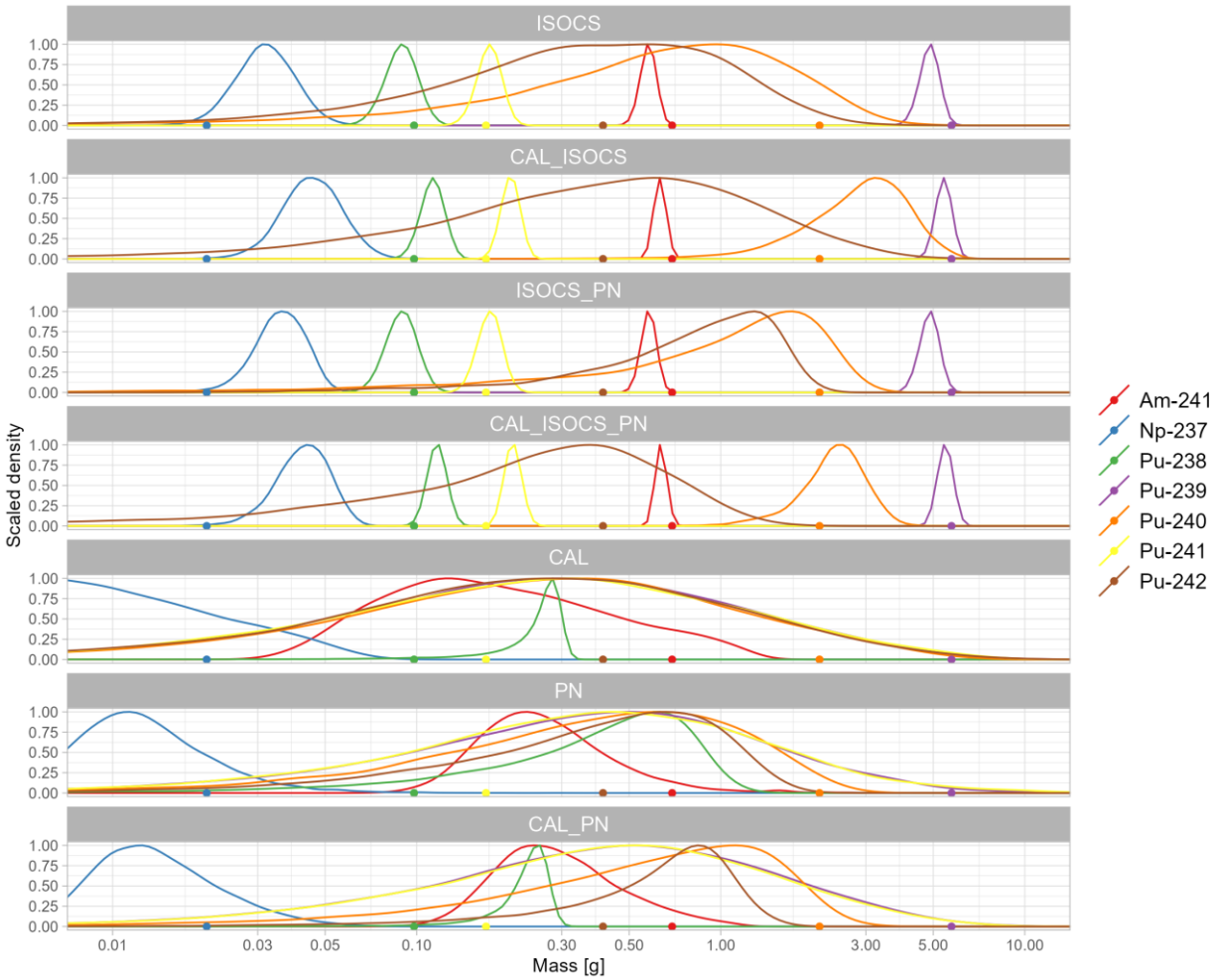

FIGURE 57. POSTERIOR DISTRIBUTIONS OF THE INFERRED RADIONUCLIDES' MASSES OVER THE WHOLE DRUM 206 (21 SOURCES) FOR DIFFERENT MEASUREMENT TECHNIQUES AND COMBINATIONS THEREOF (ISOCS, CAL-ISOCS, ISOCS-PN, CAL-ISOCS-PN, CAL, PN AND CAL-PN). THE CONSIDERED INFORMATION DEGREE IS MYSTERY DRUM WHERE NO PRIOR KNOWLEDGE ON THE DRUM'S MATRIX AND ISOTOPIC VECTOR IS CONSIDERED. PN MEANS PNCC. THE SOLID DOTS DENOTE THE TRUE VALUES.

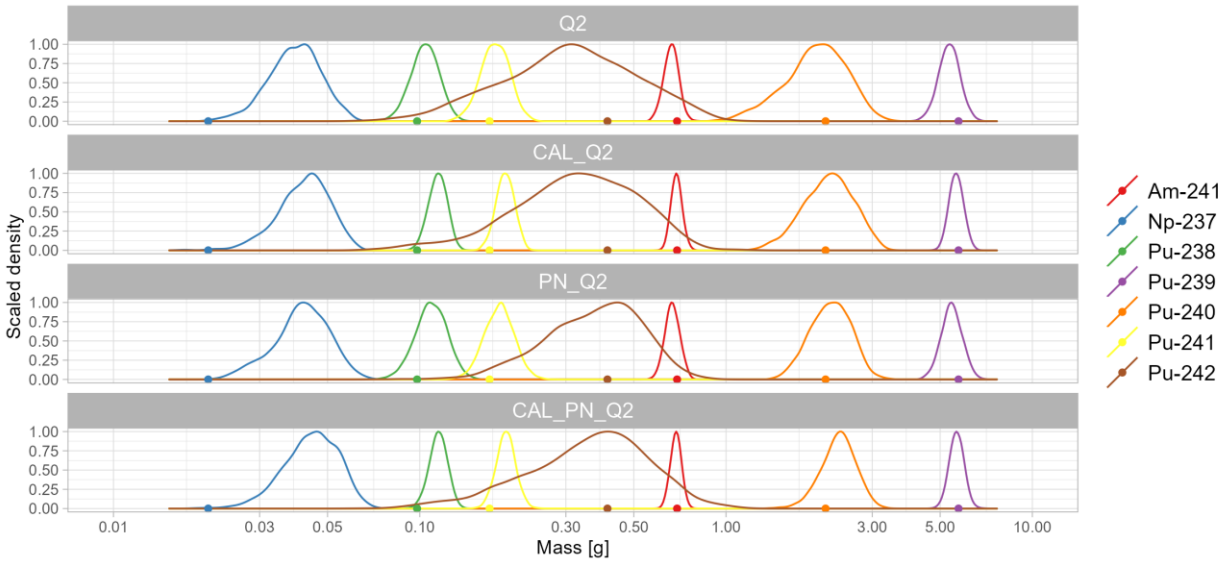

FIGURE 58. POSTERIOR DISTRIBUTIONS OF THE INFERRED RADIONUCLIDES' MASSES OVER THE WHOLE DRUM 206 (21 SOURCES) FOR DIFFERENT MEASUREMENT TECHNIQUES AND COMBINATIONS THEREOF (Q2, CAL-Q2, PN-Q2 AND CAL-PN-Q2). THE CONSIDERED INFORMATION DEGREE IS MYSTERY DRUM WHERE NO PRIOR KNOWLEDGE ON THE DRUM'S MATRIX AND ISOTOPIC VECTOR IS CONSIDERED. PN MEANS PNCC. THE SOLID DOTS DENOTE THE TRUE VALUES.

5.3.2.4 Setup 3 (mock-up 206 with mortar and XPS – single source/centre position)

The situation for Setup 3 (mock-up 206 – 1 source/centre position; Figure 59 to Figure 64) is rather similar to that of Setup 2 (mock-up 206 – 21 sources). The only significant difference between the two sets of results is that for Setup 3 and the MYSTERY DRUM assumption, the Q2-derived posterior radionuclide mass distributions become as large as the ISOCS-derived ones.

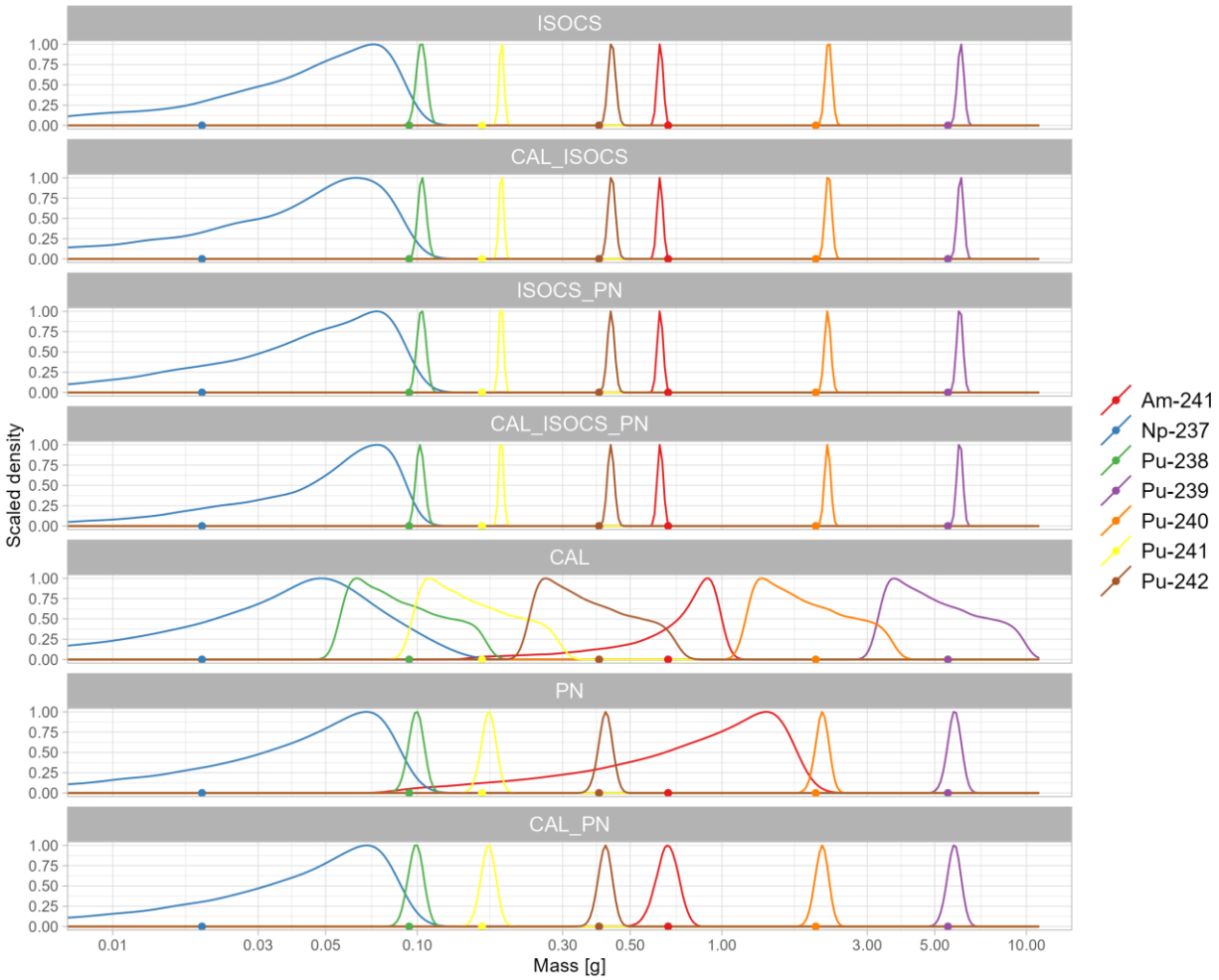

FIGURE 59. POSTERIOR DISTRIBUTIONS OF THE INFERRED RADIONUCLIDES' MASSES OVER THE WHOLE DRUM 206 (1 SOURCE – CENTRE POSITION) FOR DIFFERENT MEASUREMENT TECHNIQUES AND COMBINATIONS THEREOF (ISOCS, CAL-ISOCS, ISOCS-PN, CAL-ISOCS-PN, CAL, PN AND CAL-PN). THE CONSIDERED INFORMATION DEGREE IS FULLY KNOWN WHERE THE ONLY UNKNOWNS ARE BASICALLY THE RADIONUCLIDES' ACTIVITIES WHILE THE DRUM'S MATRIX, ISOTOPIC VECTOR AND PU SPATIAL DISTRIBUTION ARE ASSUMED TO BE KNOWN. PN MEANS PNCC. THE SOLID DOTS DENOTE THE TRUE VALUES.

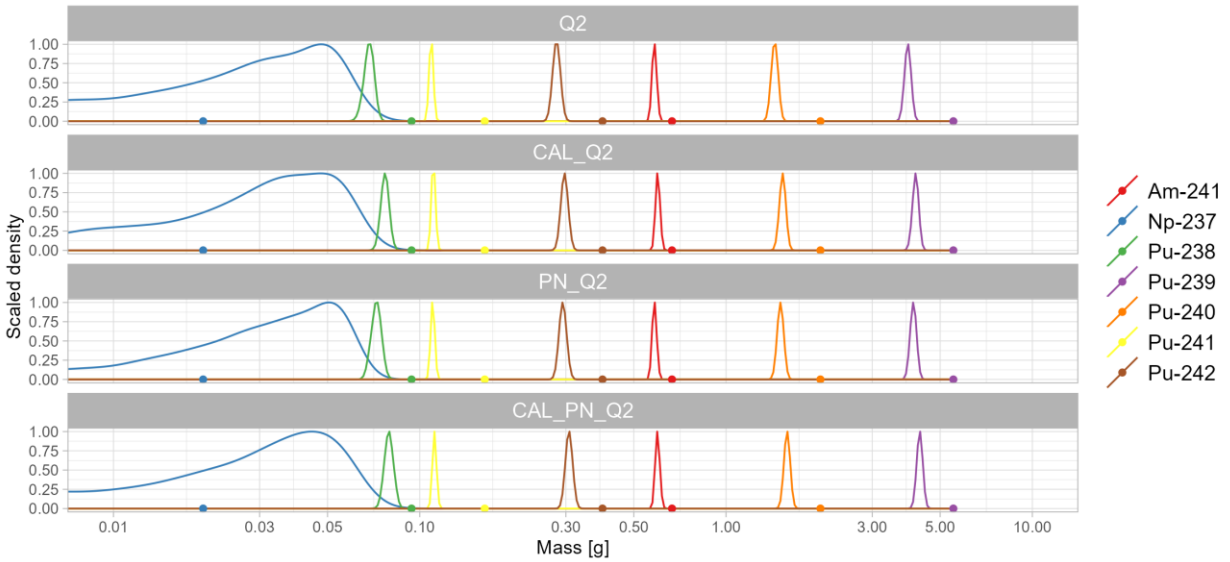

FIGURE 60. POSTERIOR DISTRIBUTIONS OF THE INFERRED RADIONUCLIDES' MASSES OVER THE WHOLE DRUM 206 (1 SOURCE – CENTRE POSITION) FOR DIFFERENT MEASUREMENT TECHNIQUES AND COMBINATIONS THEREOF (Q2, CAL-Q2, PN-Q2 AND CAL-PN-Q2). THE CONSIDERED INFORMATION DEGREE IS FULLY KNOWN WHERE THE ONLY UNKNOWNS ARE BASICALLY THE RADIONUCLIDES' ACTIVITIES WHILE THE DRUM'S MATRIX, ISOTOPIC VECTOR AND PU SPATIAL DISTRIBUTION ARE ASSUMED TO BE KNOWN. PN MEANS PNCC. THE SOLID DOTS DENOTE THE TRUE VALUES.

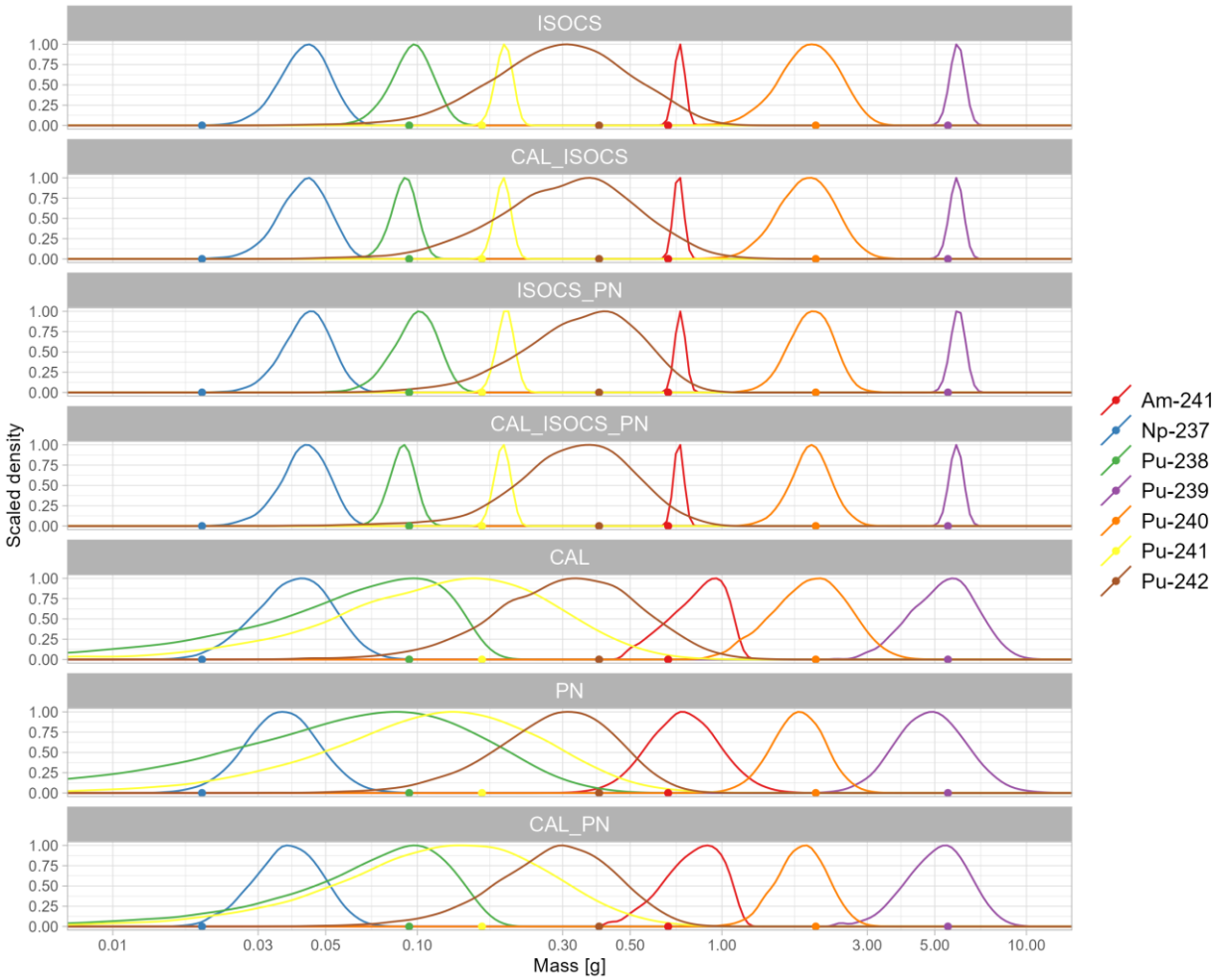

FIGURE 61. POSTERIOR DISTRIBUTIONS OF THE INFERRED RADIONUCLIDES' MASSES OVER THE WHOLE DRUM 206 (1 SOURCE – CENTRE POSITION) FOR DIFFERENT MEASUREMENT TECHNIQUES AND COMBINATIONS THEREOF (ISOCS, CAL-ISOCS, ISOCS-PN, CAL-ISOCS-PN, CAL, PN AND CAL-PN). THE CONSIDERED INFORMATION DEGREE IS REALISTIC WHERE REALISTIC PRIOR KNOWLEDGE ON THE DRUM'S MATRIX AND ISOTOPIC VECTOR IS TAKEN INTO ACCOUNT. PN MEANS PNCC. THE SOLID DOTS DENOTE THE TRUE VALUES.

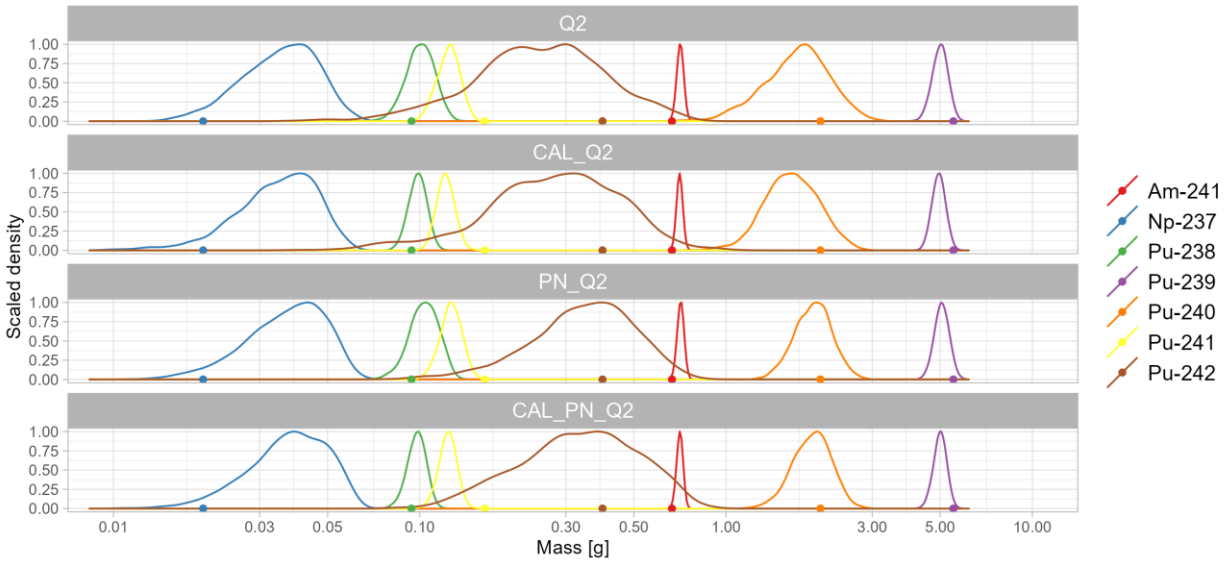

FIGURE 62. POSTERIOR DISTRIBUTIONS OF THE INFERRED RADIONUCLIDES' MASSES OVER THE WHOLE DRUM 206 (1 SOURCE – CENTRE POSITION) FOR DIFFERENT MEASUREMENT TECHNIQUES AND COMBINATIONS THEREOF (Q2, CAL-Q2, PN-Q2 AND CAL-PN-Q2).. THE CONSIDERED INFORMATION DEGREE IS REALISTIC WHERE REALISTIC PRIOR KNOWLEDGE ON THE DRUM'S MATRIX AND ISOTOPIC VECTOR IS TAKEN INTO ACCOUNT. PN MEANS PNCC. THE SOLID DOTS DENOTE THE TRUE VALUES.

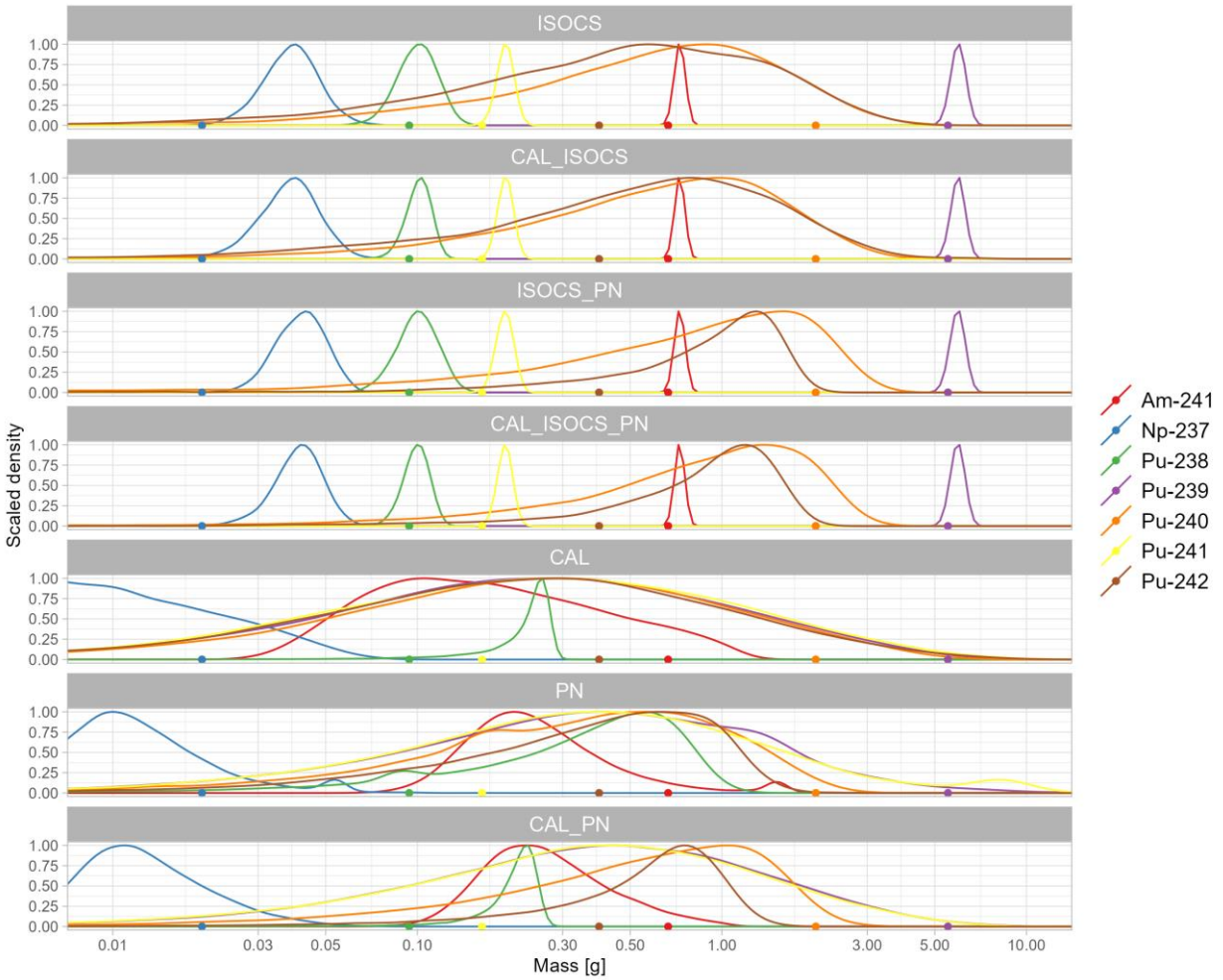

FIGURE 63. POSTERIOR DISTRIBUTIONS OF THE INFERRED RADIONUCLIDES' MASSES OVER THE WHOLE DRUM 206 (1 SOURCE – CENTRE POSITION) FOR DIFFERENT MEASUREMENT TECHNIQUES AND COMBINATIONS THEREOF (ISOCS, CAL-ISOCS, ISOCS-PN, CAL-ISOCS-PN, CAL, PN AND CAL-PN). THE CONSIDERED INFORMATION DEGREE IS MYSTERY DRUM WHERE NO PRIOR KNOWLEDGE ON THE DRUM'S MATRIX AND ISOTOPIC VECTOR IS CONSIDERED. PN MEANS PNCC. THE SOLID DOTS DENOTE THE TRUE VALUES.

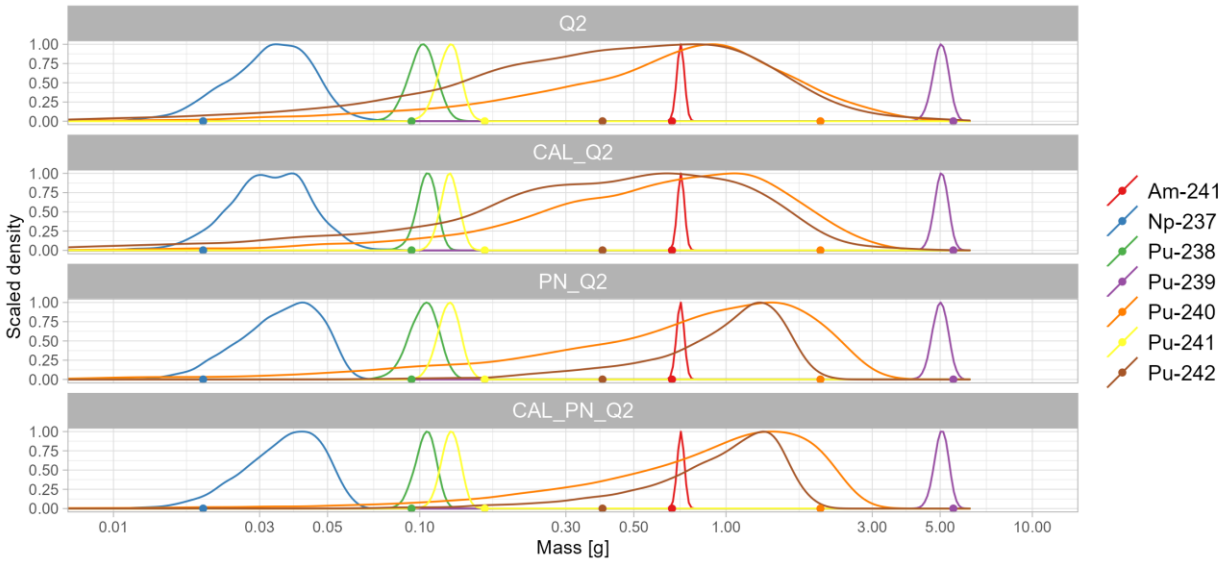

FIGURE 64. POSTERIOR DISTRIBUTIONS OF THE INFERRED RADIONUCLIDES' MASSES OVER THE WHOLE DRUM 206 (1 SOURCE – CENTRE POSITION) FOR DIFFERENT MEASUREMENT TECHNIQUES AND COMBINATIONS THEREOF (Q2, CAL-Q2, PN-Q2 AND CAL-PN-Q2). THE CONSIDERED INFORMATION DEGREE IS MYSTERY DRUM WHERE NO PRIOR KNOWLEDGE ON THE DRUM'S MATRIX AND ISOTOPIC VECTOR IS CONSIDERED. PN MEANS PNCC. THE SOLID DOTS DENOTE THE TRUE VALUES.

5.3.2.5 Setup 4 (mock-up 206 with mortar and XPS – single source/eccentric position)

For this drum setup all our calculated efficiencies seem to be largely biased (Figure 65 and Figure 66) and these biases are only partially mitigated under the REALISTIC assumption for the ISOCS-derived posterior distributions (Figure 67 and Figure 68). The Q2-based results are always quite off and for the first time (that is, for this drum only), the PNCC results under the REALISTIC assumption are wrong. As a consequence, all measurement combinations involving PNCC lead to wrong results as well. For the REALISTIC assumption, only ISOCS, CAL and the ISOCS_CAL combination provide (approximately) reasonable results. Furthermore, under the MYSTERY DRUM assumption posterior uncertainty also grows a lot compared to the REALISTIC case, with ISOCS and CAL_ISOCS the two only methods not showing significant bias (Figure 69 and Figure 70).

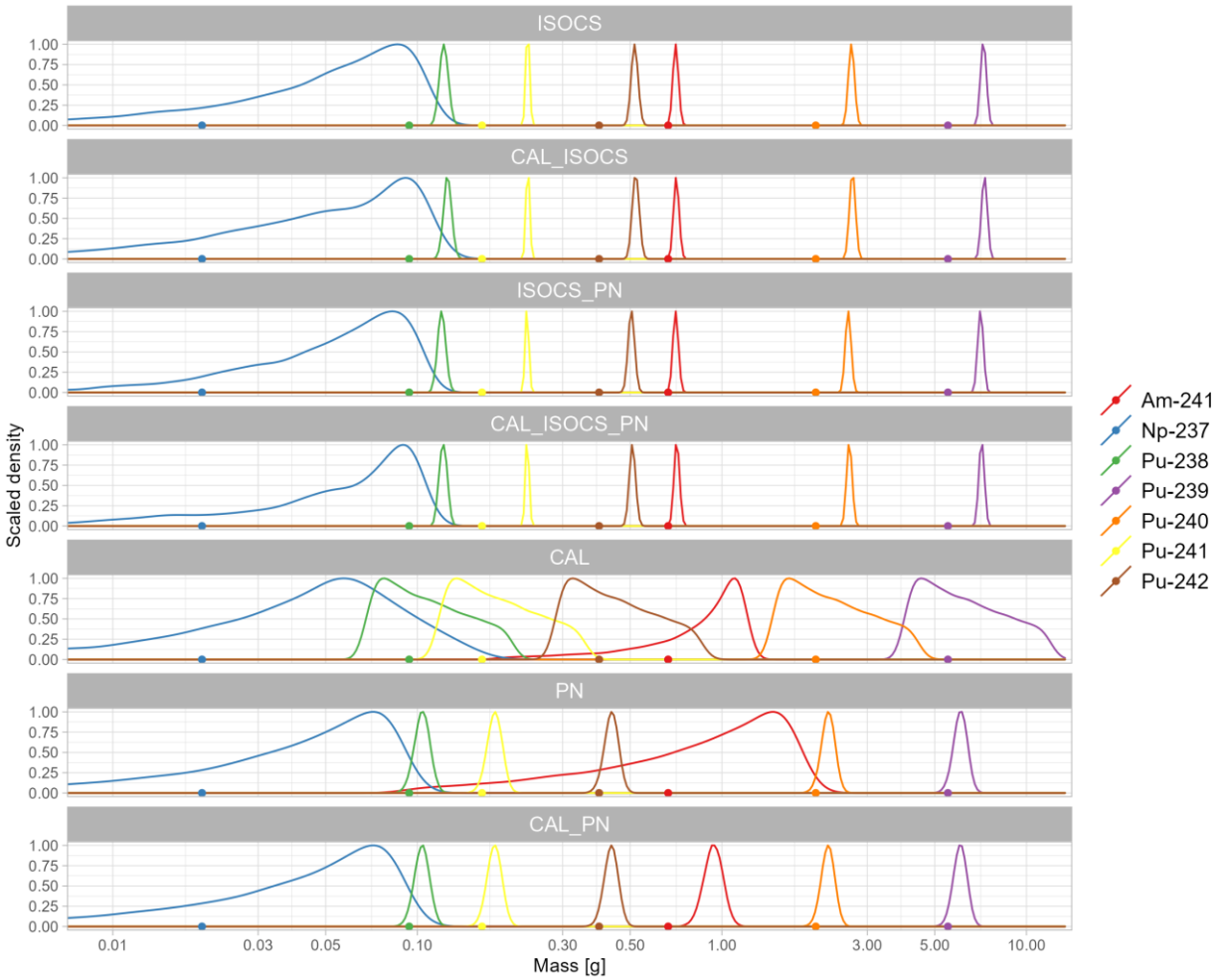

FIGURE 65. POSTERIOR DISTRIBUTIONS OF THE INFERRED RADIONUCLIDES' MASSES OVER THE WHOLE DRUM 206 (1 SOURCE – ECCENTRIC POSITION) FOR DIFFERENT MEASUREMENT TECHNIQUES AND COMBINATIONS THEREOF (ISOCS, CAL-ISOCS, ISOCS-PN, CAL-ISOCS-PN, CAL, PN AND CAL-PN). THE CONSIDERED INFORMATION DEGREE IS FULLY KNOWN WHERE THE ONLY UNKNOWNS ARE BASICALLY THE RADIONUCLIDES' ACTIVITIES WHILE THE DRUM'S MATRIX, ISOTOPIC VECTOR AND PU SPATIAL DISTRIBUTION ARE ASSUMED TO BE KNOWN. PN MEANS PNCC. THE SOLID DOTS DENOTE THE TRUE VALUES.

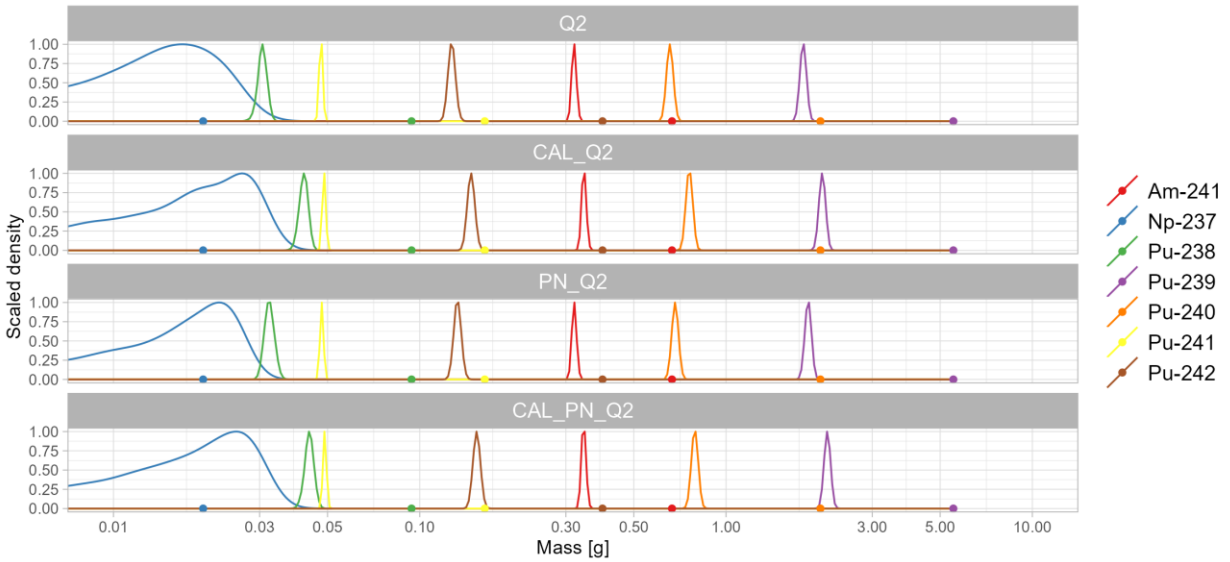

FIGURE 66. POSTERIOR DISTRIBUTIONS OF THE INFERRED RADIONUCLIDES' MASSES OVER THE WHOLE DRUM 206 (1 SOURCE – ECCENTRIC POSITION) FOR DIFFERENT MEASUREMENT TECHNIQUES AND COMBINATIONS THEREOF (Q2, CAL-Q2, PN-Q2 AND CAL-PN-Q2). THE CONSIDERED INFORMATION DEGREE IS FULLY KNOWN WHERE THE ONLY UNKNOWNS ARE BASICALLY THE RADIONUCLIDES' ACTIVITIES WHILE THE DRUM'S MATRIX, ISOTOPIC VECTOR AND PU SPATIAL DISTRIBUTION ARE ASSUMED TO BE KNOWN. PN MEANS PNCC. THE SOLID DOTS DENOTE THE TRUE VALUES.

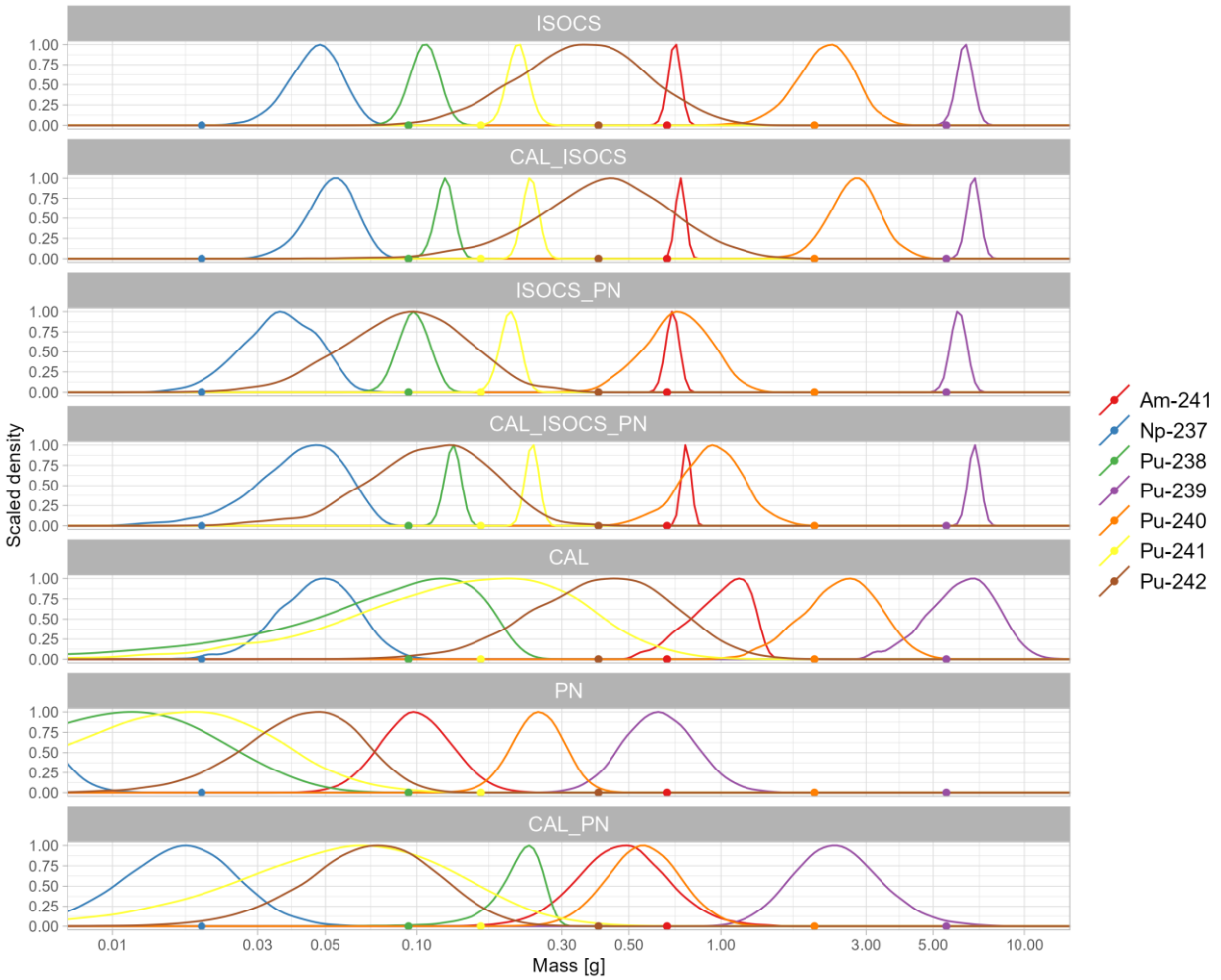

FIGURE 67. POSTERIOR DISTRIBUTIONS OF THE INFERRED RADIONUCLIDES' MASSES OVER THE WHOLE DRUM 206 (1 SOURCE – ECCENTRIC POSITION) FOR DIFFERENT MEASUREMENT TECHNIQUES AND COMBINATIONS THEREOF (ISOCS, CAL-ISOCS, ISOCS-PN, CAL-ISOCS-PN, CAL, PN AND CAL-PN). THE CONSIDERED INFORMATION DEGREE IS REALISTIC WHERE REALISTIC PRIOR KNOWLEDGE ON THE DRUM'S MATRIX AND ISOTOPIC VECTOR IS TAKEN INTO ACCOUNT. PN MEANS PNCC. THE SOLID DOTS DENOTE THE TRUE VALUES.

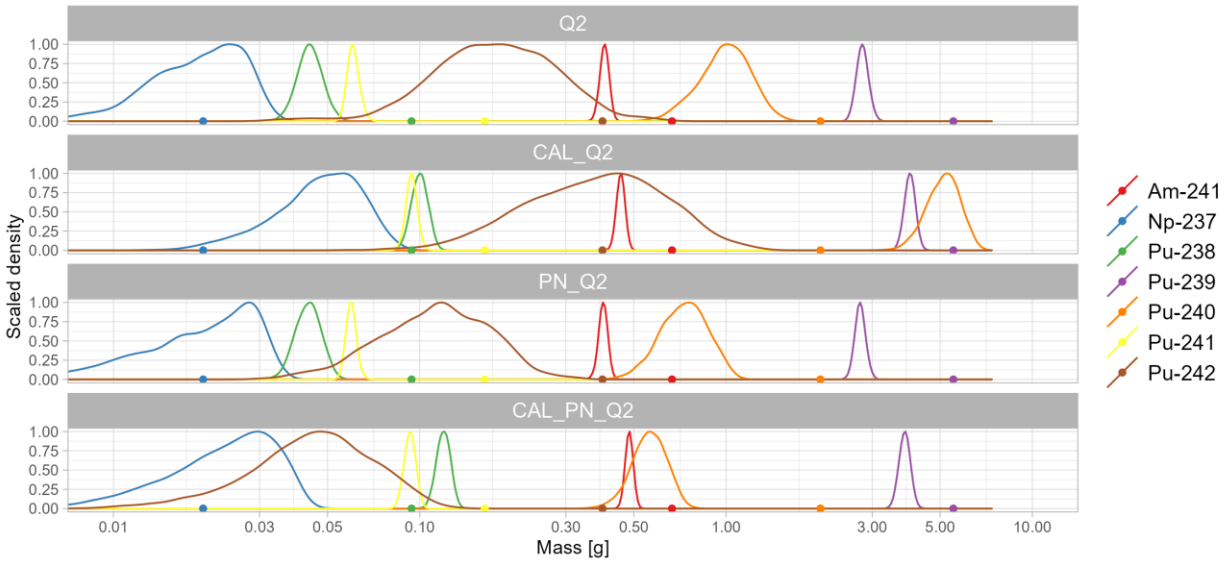

FIGURE 68. POSTERIOR DISTRIBUTIONS OF THE INFERRED RADIONUCLIDES' MASSES OVER THE WHOLE DRUM 206 (1 SOURCE – ECCENTRIC POSITION) FOR DIFFERENT MEASUREMENT TECHNIQUES AND COMBINATIONS THEREOF (Q2, CAL-Q2, PN-Q2 AND CAL-PN-Q2).. THE CONSIDERED INFORMATION DEGREE IS REALISTIC WHERE REALISTIC PRIOR KNOWLEDGE ON THE DRUM'S MATRIX AND ISOTOPIC VECTOR IS TAKEN INTO ACCOUNT. PN MEANS PNCC. THE SOLID DOTS DENOTE THE TRUE VALUES.

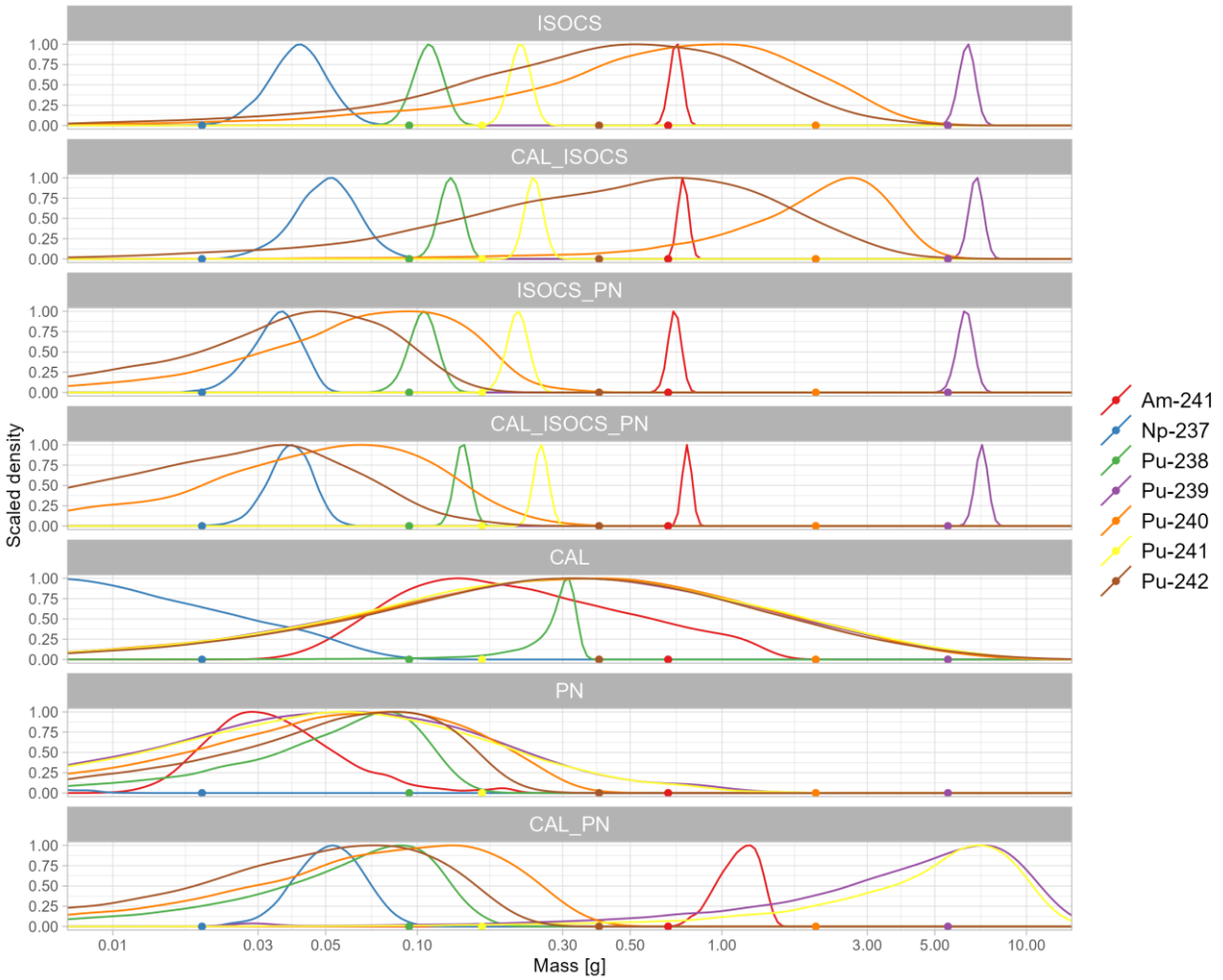

FIGURE 69. POSTERIOR DISTRIBUTIONS OF THE INFERRED RADIONUCLIDES' MASSES OVER THE WHOLE DRUM 206 (1 SOURCE – ECCENTRIC POSITION) FOR DIFFERENT MEASUREMENT TECHNIQUES AND COMBINATIONS THEREOF (ISOCS, CAL-ISOCS, ISOCS-PN, CAL-ISOCS-PN, CAL, PN AND CAL-PN). THE CONSIDERED INFORMATION DEGREE IS MYSTERY DRUM WHERE NO PRIOR KNOWLEDGE ON THE DRUM'S MATRIX AND ISOTOPIC VECTOR IS CONSIDERED. PN MEANS PNCC. THE SOLID DOTS DENOTE THE TRUE VALUES.

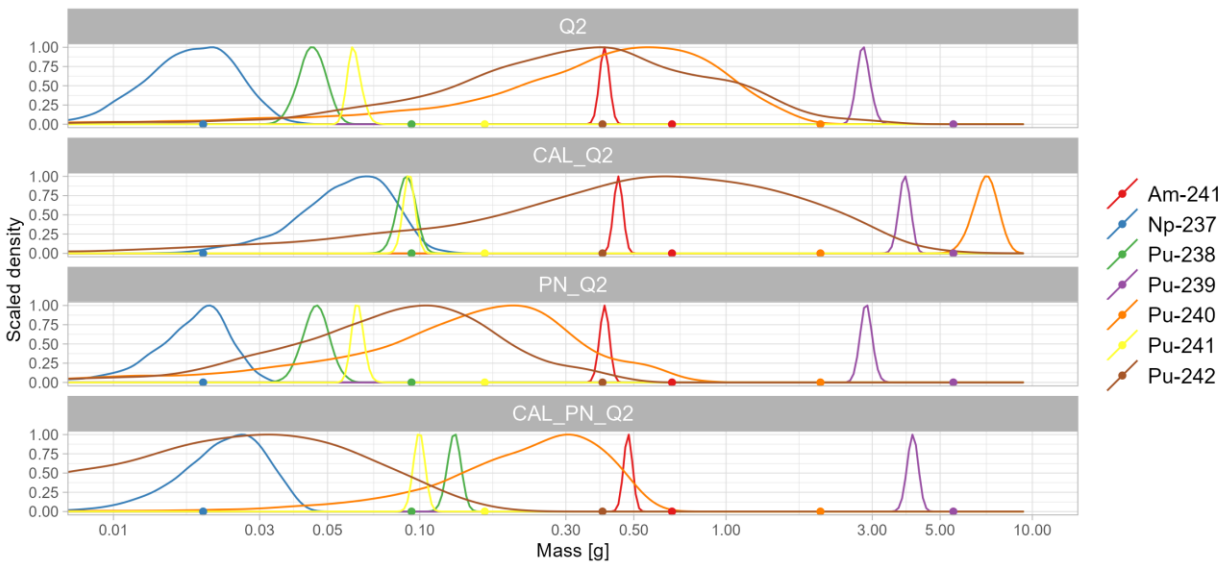

FIGURE 70. POSTERIOR DISTRIBUTIONS OF THE INFERRED RADIONUCLIDES' MASSES OVER THE WHOLE DRUM 206 (1 SOURCE – ECCENTRIC POSITION) FOR DIFFERENT MEASUREMENT TECHNIQUES AND COMBINATIONS THEREOF (Q2, CAL-Q2, PN-Q2 AND CAL-PN-Q2). THE CONSIDERED INFORMATION DEGREE IS MYSTERY DRUM WHERE NO PRIOR KNOWLEDGE ON THE DRUM'S MATRIX AND ISOTOPIC VECTOR IS CONSIDERED. PN MEANS PNCC. THE SOLID DOTS DENOTE THE TRUE VALUES.

5.4 The real unconditioned waste drum exercise

5.4.1 Methodology

The methodology used for the real drum is globally similar to that used for the mock-ups and is described in detail in [41], except for the addition of the calorimeter measurement. The main difference is that for the real drum (1) the drum is stylized as containing 20 horizontal segments (as opposed to 21-point source locations for the mock-ups) and (2) the matrix is assumed to be known while the main source of uncertainty in the efficiencies is considered to be the uncertainty in the source distribution in each drum segment. For the latter, we are interpolating between two extremes: a homogeneous distribution of activity over the segment versus a point source centered at the top or bottom of the segment.

Concerning the calorimeter data for the real drum, the issue around the selection (or lack of) an appropriate baseline measurement was already raised in [1], together with the observations that the different blocks may react differently depending on the thermal properties of the object, and the location of heat production within. For the analysis of the real drum here, we made use of the central block data only, as that seemed to provide the more robust estimates, and the joule effect drum baseline, as that seemed to resemble most the real drum.

5.4.2 Posterior distributions of radioisotope masses

The inference results for Setup 1, the real unconditioned waste drum, are presented in Figure 71. Overall, it is observed that the gamma spectrometry data (whether ISOCS or 3AX-SGS) mostly always seem to provide a lot of information on the gamma-emitting radionuclides together with those non-gamma emitting ones of which prior estimates can be obtained by gamma-based isotopic composition analysis (Pu-242, Np-237, U-235) using for instance the FRAM software. The main effect of considering the CAL and PNCC techniques is a reduction of

uncertainty for the non-gamma emitting nuclides with large specific activity that isotopic composition analysis cannot handle, such as Cm-244 in this particular case.

This exercise does not allow to evaluate the accuracy of the approach, as the true activities are not known. For this reason, a synthetic experiment was performed as well, and included in [41].

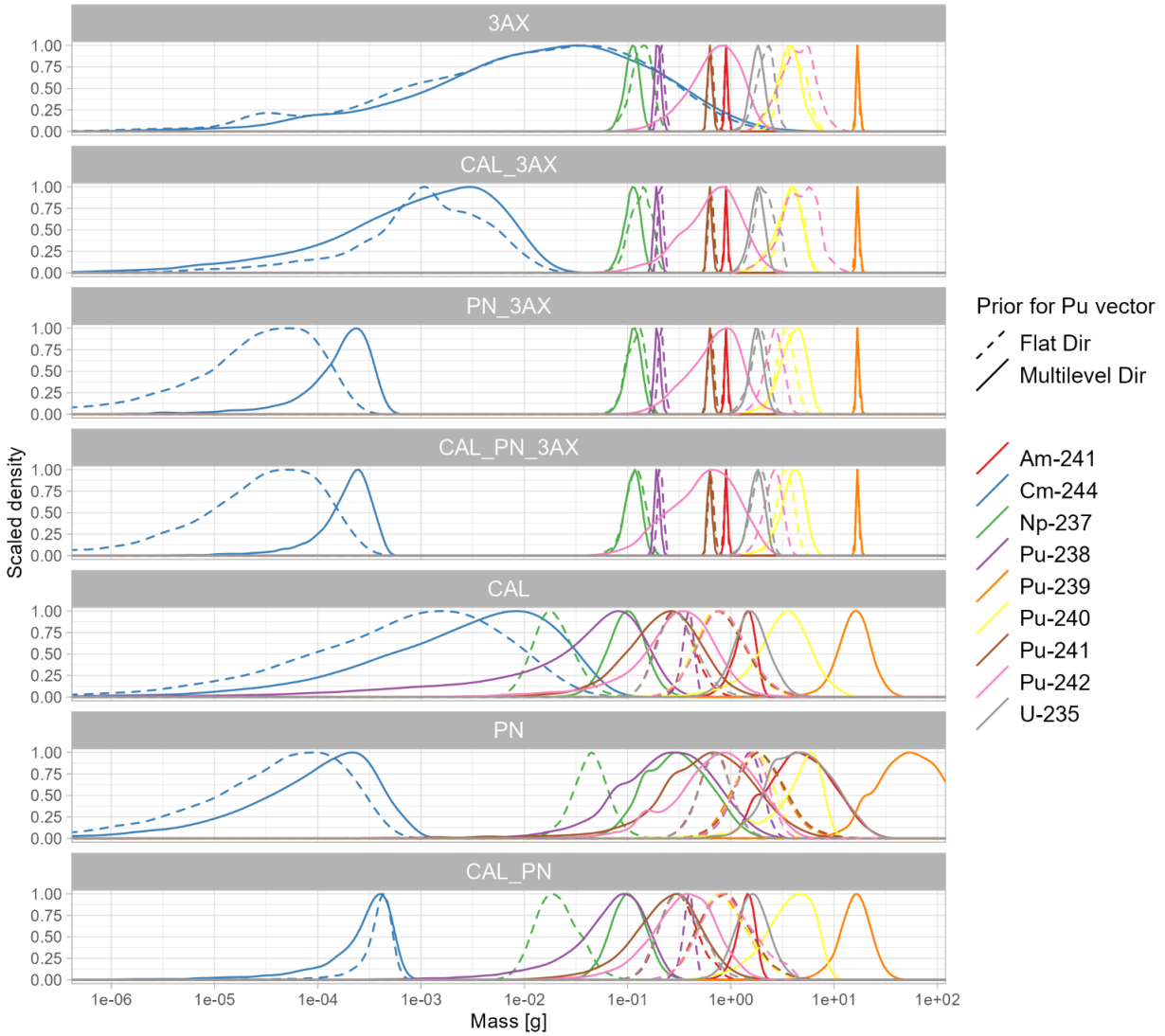

FIGURE 71 POSTERIOR DISTRIBUTIONS OF THE INFERRED RADIONUCLIDES' MASSES OVER THE WHOLE REAL DRUM FOR DIFFERENT MEASUREMENT TECHNIQUES AND COMBINATIONS THEREOF 3AX, CAL-3AX, PN-3AX, CAL-PN-3AX, CAL, PN AND CAL-PN). HERE NO PRIOR KNOWLEDGE ON THE DRUM'S SOURCE DISTRIBUTION TYPE (HOMOGENEOUS VERSUS POINT SOURCE IN EACH DRUM'S SEGMENT) AND PU SPATIAL DISTRIBUTION IS CONSIDERED. PN MEANS PNCC. THE SOLID DOTS DENOTE THE TRUE VALUES. THE PRIOR DISTRIBUTION FOR THE PU VECTOR CAN BE (1) MULTILEVEL DIRICHLET, MEANING THAT DEVIATIONS FROM THE PRIOR ARE ALLOWED IF NEEDED TO BETTER FIT THE MEASUREMENT DATA AND (2) FLAT DIRICHLET, MEANING THAT THE ISOTOPIC VECTOR CAN TAKE ANY VALUES UNDER THE CONSTRAINT OF SUMMING UP TO UNITY.

5.5 Conclusions with respect to the SCK CEN exercises

In general, if the considered waste drum contains only gamma-emitting radionuclides together with non-gamma-emitting radionuclides for which a priori information is available on the relation with gamma-emitting radionuclides then combining gamma spectrometry (ISOCS, Q2 or 3AX-SGS) with CAL and PNCC has little added value compared to ISOCS or 3AX-SGS alone, although combinations involving CAL can lead to less biased and more precise estimates because of the insensitivity to the matrix effect. In contrast, The CAL and PNCC techniques are useful in combination with gamma (ISOCS or 3AX SGS) to jointly quantify gamma emitting radionuclides and non-gamma emitting radionuclides with large specific activity that cannot be estimated from others, such as Cm-244. Furthermore, if the isotopic vector is well constrained a priori, then CAL and PNCC can both recover relatively accurate mean posterior radionuclide masses/activities, relatively unbiased, but less precise than gamma spectrometry for the gamma-emitting radionuclides.

More specifically, for the real drum exercise (Setup 1), we clearly see the added value of CAL and PNCC on the results, especially for Cm-244. PNCC is likely less biased than CAL here, because of the issue around the selection of an appropriate baseline for a real drum. Moreover, combinations involving both PNCC and CAL lead to the most precise Cm-244 estimates.

For the mock-up drums exercise (Setups 2-6), it is noted that the accuracy of the calculated efficiencies is crucial to derive unbiased radionuclide mass estimates. Nevertheless, even in case of seemingly accurate efficiencies complex compensations effects can still arise and bias the results. This is especially the case for our Q2 efficiencies. These complex biases are obviously not welcome and we are currently looking deeply into how to solve this issue, mainly by considering realistic uncertainty in the calculated efficiencies the MCMC is interpolating through. Fortunately, under a realistic level of prior information we find that the ISOCS-based MCMC inversions generally lead to unbiased results, because the flexibility of the REALISTIC assumption permits to compensate the bias in a proper way. Despite the fact that the gamma measurements and information on the isotopic vector already allow decent estimates on all isotopes in case of the mock-up drums, it is still apparent in different cases that calorimetry slightly improves the results in terms of bias and precision, because of the insensitivity to the matrix effect. For the mock-up drums, this is only true because we have very good baseline measurements available, while for a real drum, the information content of the calorimeter measurement will always be less because of larger baseline uncertainty.

Concerning the Bayesian approach, these exercises clearly revealed why it is useful in the context of radioactive waste characterization:

- Given measurement data and a data-generating process, interpreting jointly data of multiple measurement techniques is as straightforward as interpreting each technique individually, and can be done in the exact same way, as illustrated by all figures in Sections 5.3 and 5.4.
- Given measurement data, the data-generating process, and a series of expert-based prior distributions, posterior predictive checks can reveal whether the data is consistent with the model or not, and adjustments or further investigations can be made if necessary. In our case, this helped revealing the issue with the real drum calorimeter baseline selection and revealed some (apparent) inconsistencies in the theoretically estimated efficiencies.

From the latter, we conclude that a proper efficiency model, backed as much as possible by calibration data, and using realistic uncertainties for those efficiencies, is very important to come up with consistent and robust activity posteriors based on multiple techniques.

6 Overall conclusions

Calorimetry makes it possible to significantly reduce the uncertainty when characterizing the mass of plutonium (or, by extension any isotopic vector with sufficient heat production) compared to neutron and gamma measurements. Indeed, these last suffer from large waste matrix and Pu (or more general activity) localisation effects resulting in punitive uncertainties when measuring large, dense and heterogeneous waste packages, like concrete drums containing technological waste. In such cases, the distribution of the Pu mass can be much more accurate when using calorimetry in combination with gamma and neutron measurements, and the various experiments interpreted here reveal improvements both in bias and precision. Note that contrary to heterogeneous waste, dense homogenous packages like those containing bituminized radioactive sludge can be precisely characterized with neutron and gamma measurements, even if matrix effects are also very high. Indeed, thanks to the knowledge of the waste homogeneity, the large gamma and neutron attenuations can be precisely corrected and the measurement uncertainties remain acceptable.

Calorimetry does require the isotopic vector to convert the measured heat flux to plutonium and/or other alpha-emitting product mass or activity. In presence of high alpha-emitting isotopes like ^{241}Am and ^{238}Pu, which bring in general the major part of alpha activity, an isotopic composition measurement or a reliable estimate is a priori needed.

Calorimetry measurement times are long for radioactive waste packages (a few days, plus a few days for the baseline measurement for a 200-L drum) and this technique should be used when gamma spectroscopy and passive neutron coincidence counting are not conclusive, making another reference measurement with smaller uncertainties necessary to guarantee an acceptance criterion, or a criticality threshold, for instance:

- one of the acceptance criteria for surface repository in France is 3.7 GBq/ton of alpha activity (extrapolated in 300 years, which is the release date of the repository). For instance, a 2 ton package, like some of the 870 L drums of CEA, would have an alpha activity threshold near 7 GBq of (Pu+Am). If we consider plutonium coming from a PWR nuclear power reactor, a rough estimate gives a specific Pu+Am activity of the order of 20 to 30 GBq/g (depending on the fuel burnup) and a specific power between 20 and 30 mW/g, mainly due to ^{238}Pu and ^{241}Am (so for military Pu coming from low burnup fuels, these figures can be much lower). Therefore, the 7 GBq acceptance criterion represents only a fraction of gram of Pu (between 0.2 and 0.3 g for non-military plutonium), that is to say a power of a few mW (and even less for military Pu). Similarly, in Belgium, raw compactable waste acceptance criteria, as well as surface disposal limits, give rise to thermal powers less than one mW, using the isotopic composition of the sources inserted in the mock-up drums at SCK CEN, for a 200-L drum. This objective seems difficult to reach with the current system (from [1], the detection limit of the current prototype is at best in the range of 5-15 mW, and can easily increase by an order of magnitude if a decent baseline measurement is not available) but possible improvements of large calorimeters from the return of experience of the CHANCE project could perhaps make it possible in the future;
- another possible application would be to reduce the uncertainty on gamma and neutron measurements for Pu-rich waste packages that pose a safety/criticality problem, for instance in transportation, interim storage or final disposal. To give an order of magnitude, a typical limit not to be exceeded is 200 g of fissile material (i.e. Pu + ^{235}U mass) in some facilities or transportation regulations. If the waste is known not to contain ^{235}U (which has a very low specific power), calorimetry can give a precise estimate of the Pu mass (considering Am as an overestimation factor in a conservative safety/criticality approach).

Finally, the Bayesian approach adopted herein has clearly proven to be very useful for radioactive waste characterization, as it allows accounting for a priori available information in a straightforward and explicit way, makes jointly interpreting different measurements of the same waste package seamless, and allows for model-data

consistency checks. Moreover, the end result is always a complete posterior distribution, that allows for more intuitive and transparent decision making, calculating probabilities of exceeding certain thresholds, risk assessment, etc.

7 References

[1] CHANCE WP3 Deliverable 3.3: Results of the experimental investigation of calorimetry applicability.

[2] Application Guide to Safeguards Calorimetry, D.S. Bracken, R.S. Biddle et. al., LA-13867-M, January 2002.

[3] ENDFB.VII.1 nuclear data library (JANIS), http://www.oecd-nea.org/janisweb/

[4] Waseem Shehzad et al., Estimation of background radiation levels and associated health risks in mineral rich district Chiniot, Pakistan, Journal of Radioanalytical and Nuclear Chemistry 319(3):1-8, January 2019

[5] Calorimetric Non Destructive Assay of Large Volume and Heterogeneous Radioactive Waste Drums, W. R. Kubinski, C. Carasco, D. Kikoła et al., The European Physical Journal Conferences 225:06003, 2020

[6] J. L. Parker, The Use Of Calibration Standards And The Correction For Sample Self-Attenuation In Gamma-Ray Nondestructive Assay, Los Alamos National Laboratory, LA-10045 (1984).

[7] Some techniques applied for plutonium measurements in waste drums, B. Autrusson, J. L. Dufour, P. Funk, T. Lambert, N. Pépin, B. Thaurel, Institut de Protection et de Sûreté Nucléaire, https://www.irsn.fr/.

[8] Calorimetric Non Destructive Assay of Large Volume and Heterogeneous Radioactive Waste Drums, W. R. Kubinski, C. Carasco, D. Kikoła et al., The European Physical Journal Conferences 225:06003, 2020.

[9] C.J. Werner (editor), "MCNP Users Manual - Code Version 6.2", LA-UR-17-29981, 2017

[10] OPERATIONAL QUANTITIES FOR 9 EXTERNAL RADIATION EXPOSURE, Joint report of International Commission on Radiation Units and Measurements and International Commission on Radiological Protection, Journal of the ICRP, 2017

[11] Gamma-radiation-induced corrosion of aluminum alloy: low dose effect, K. Kanjana, P. Ampornrat and J. Channuie, International Nuclear Science and Technology Conference 2016

[12] Effect of gamma-irradiation on the properties of aluminum dihydrogen triphosphate, WEIQIANG SONG, QINGHUAN SONG, LONGCHAO WU and LANTAO YANG, JSCS–5027

[13] EXAMINATION OF THE IBRADIATED 6061 .ALUMINUM HFIB TARGET HOLDER, K. Farrell, R. T. King, and A. Jostsons

[14] Influence of gamma ray irradiation on stoichiometry of hydrothermally synthesized bismuth telluride nanoparticles, Abishek, N. S. ;Naik, K. Gopalakrishna

[15] Effect of High Fluence Neutron Irradiation on Transport Properties of Thermoelectrics , H. WANG AND K.J. LEONARD Materials Science and Technology Division Oak Ridge National Laboratory Oak Ridge, TN 37831 USA

[16] CHANGES IN MECHANICAL PROPERTIES DUE TO GAMMA IRRADIATION OF HIGH-DENSITY POLYETHYLENE (HDPE), S. S. Cota*, V. Vasconcelos, M. Senne Jr., L. L. Carvalho, D. B. Rezende and R. F. Côrrea

[17] NEUTRON RADIATION EFFECT ON CARBON-LOADED POLYETHYLENE, Eduardo P. Ervedosa1,3, Frederico A. Genezini2 and Luiz A. P. Santos

[18] Polyethylene terephthalate degradation under reactor neutron irradiation, K. Chikaoui a, ∗, M. Izerrouken b, M. Djebara a, M. Abdesselam

[19] D. Reilly, N. Ensslin, H. Smith, S. Kreiner, Passive Nondestructive Assay Of Nuclear Materials (1991).

[20] R. Antoni, C. Passard, B. Perot, F. Guillaumin, C. Mazy, M. Batifol, G. Grassic, Reduction of the uncertainty due to fissile clusters in radioactive waste characterization with the Differential Die-away Technique, Nucl. Instr. And Meth. A, 895, 144-149 (2018).

[21] D. S. Bracken, R. S. Biddle, L. A. Carrillo, Application Guide to Safeguards Calorimetry, LA-13867-M (2002).

[22] J. A. Mason, K. J. Burke and A. C. N. Towner, Characteristics and Performance of a Large Volume Twin Cell Heat-flow Calorimeter for Plutonium and Tritium Measurement, Proceedings of INMM12, Orlando, Florida, 12-A-359-INMM (2012).
[23] D. S. Bracken, Performance Testing of a Large Volume Calorimeter, 45th Annual INMM Meeting Orlando, FL, LA-UR-04-4404 (2004).
[24] D. S. Bracken, C. Bonner, K. Vigil et. al., Large Volume Calorimeter Comparison Measurement Results Collected at the Los Alamos National Laboratory Plutonium Facility, Annual Meeting of the Institute of Nuclear Materials Management; Phoenix, AZ, LA-UR-05-4398 (2005).
[25] W. R. Kubinski, C. Carasco, D. Kikola, C. Mathonat, D. Ricard, D. Tefelski and H. Tietze-Jaensch, Calorimetric Non-Destructive Assay of Large Volume and Heterogeneous Radioactive Waste Drums, EPJ Web of Conferences 225, 06003 (2020).
[26] A. Clement, N. Saurel, G. Perrin, "Stochastic approach for radionuclides quantification," in EPJ Web of Conferences 170, 06002 (2018).
[27] A. Clement, N. Saurel, G. Perrin and N. Gombert, Bayesian approach for multi gamma radionuclide quantification applied on weakly attenuating nuclear waste drums, IEEE Transactions On Nuclear Science, Vol. 68 (2021).
[28] E. Laloy, B. Rogiers,A. Bielen, S. Boden, Bayesian inference of 1D activity profiles from segmented gamma scanning of a heterogeneous radioactive waste drum, Appl. Rad. And Isot. 109803 (2021).
[29] T. Bücherl, S. Rummel, O. Kalthoff, A Bayesian method for the evaluation of segmented gamma scanning measurements – Description of the principle, Nucl. Instr. and Meth. in Phys. Res. A 165887 (2021).
[30] C. Carasco, Coupling gamma ray spectrometry and tomography in a Bayesian frame, Nucl. Instr. and Meth. in Phys. Res. A, volume 990 164985 (2021).
[31] T. Marchais, B. Pérot, C. Carasco, P.-G. Allinei, P. Chaussonnet, J.-L. Ma, H. Toubon, Detailed MCNP Simulations of Gamma-Ray Spectroscopy Measurements With Calibration Blocks for Uranium Mining Applications, IEEE Transactions on Nuclear Science 65 (2018).
[32] Canberra Industries Inc., Genie2000 Basic Spectroscopy Software User's Manual (2004), Genie 2000 Spectroscopy Software: Customization Tools, V3.0.
[33] W. Verkerke, D. Kirkby, The RooFit toolkit for data Modelling, roofit.sourceforge.net.
[34] Golding, N., 2019. greta: simple and scalable statistical modelling in R. J. Open Source Softw., 4, p. 1601.
[35] R Core Team (2022). R: A language and environment for statistical computing. R Foundation for Statistical Computing, Vienna, Austria. URL https://www.R-project.org/.
[36] Dillon, J.V., Ian Langmore, Dustin Tran, Eugene Brevdo, Srinivas Vasudevan, Dave Moore, Brian Patton, Alex Alemi, Matthew D. Hoffman, and Rif A. Saurous, 2017. Tensorflow distributions. CoRR, abs/1711.10604.
[37] Abadi, M., Agarwal, A., Barham, P., et al. TensorFlow: Large-Scale Machine Learning on Heterogeneous Distributed Systems. ArXiv e-prints, March 2016, https://www.tensorflow.org.
[38] Neal R (2011). MCMC Using Hamiltonian Dynamics. In S Brooks, A Gelman, GL Jones,XL Meng (eds.), Handbook of Markov Chain Monte Carlo, pp. 116–162. Chapman & Hall CRC.
[39] Betancourt, M. 2018. A Conceptual Introduction to Hamiltonian Monte Carlo. arXiv preprint arXiv:1701.02434.
[40] Borella, A., Boden, S., Bruggeman, C., Rogiers, B., Smets, S., Valcke, E. 2021. Neutron coincidence measurements and Monte Carlo modelling of waste drums containing reference nuclear material. EPJ Web of Conferences 253, 07001. https://doi.org/10.1051/epjconf/202125307001.
[41] Laloy, E, Rogiers, B., Bielen, A., Borella, A., Boden, S. Improving Bayesian radiological profiling of waste drums using Dirichlet priors, Gaussian process priors, and hierarchical modeling. Under review for Applied Radiation and Isotopes. Preprint available at https://arxiv.org/abs/2205.07786.
[42] Gelman A. G, and D. N Rubin (1992), Inference from iterative simulation using multiple sequences, Statistical Science,7, 457 - 472.